Universitetet i Stavanger

FACULTY OF SCIENCE AND TECHNOLOGY

MASTER'S THESIS

Study program /specialization: Master of Science in Structural Engineering and materials	Spring semester, 2020. Open access
Author: Hadi Pezeshki	_____ (Author's signature)

Faculty Supervisor(s): Prof. Kenneth A. Macdonald

Industry Supervisor(s): Dr. Håkon S. Hasting, Dr. Sylvain Bordet

Title of the master's thesis:

Numerical Simulation of Industrial Ultrasonic Testing of Material

Credits: 30 ECTS

Keywords: Ultrasonic Non-destructive Testing Numerical Simulation Finite element modeling Wave propagation Experimental testing	Number of pages: vii + 71 + 5 (supplemental material/other) Stavanger, 29th June 2020

Numerical Simulation of Industrial Ultrasonic Testing of Material

By

Hadi Pezeshki

Master's Thesis
Presented to the Faculty of Science and Technology
The University of Stavanger

THE UNIVERSITY OF STAVANGER
JUNE 2020

Acknowledgment

I would like to thank Prof. Kenneth A. Macdonald for his supervision and guidance, and Dr. Håkon S. Hasting and Dr. Sylvain Bordet for invaluable guidance throughout the project and for enthusiastically inspiring. I would also like to express my gratitude to DNV GL, Stavanger, for giving me the opportunity to do this thesis and using the NDT Lab and office equipment. My thanks extend to all my colleagues in the DNV GL, inspection department in Stavanger. It was a pleasure to be with them during the journey of this thesis.

Abstract

In this thesis, numerical simulation of ultrasonic testing is developed by modeling three different materials including Perspex, water, and steel in each model. Procedures of calibration of An angle probe including timebase calibration, probe index, and probe angle determinations are simulated by 4 different specimens. In addition, speed of sound in the three modeled media, probe near field length, time base linearity, and A-scan display were calculated and verified.

The geometry of V1, V2 calibration blocks, and a manipulated V1 calibration block were simulated in the three different models. A model with no detectable back wall echo by the probe was also created to study the noise signals generated in the simulation. An MWB60-N4 type angle probe producing an angle beam in 60 degrees in 4 MHz central frequency along with water coupling were simulated in each model. In the Results section, the nodal displacements are illustrated in magnitude and local directions that shows wave propagation through the different assembled materials.

The simulation results show that the mode change has successfully happened in the probe-coupling and coupling-specimen interfaces. An initial P-wave at the probe medium transformed into an S-wave at the specimen medium. The average speed of sound in the probe and specimen media has been verified with the analytical values. The probe near-field length was obtained at approximately 29mm which is almost the same length as proposed by the probe manufacture. The probe index is the point where the probe centerline coincides with the coupling. The angle of the probe was measured at around 58 degrees that is comparable to the nominal value of 60 degrees proposed by manufacture. Besides, A-scan displays of the models were created by using the extracted data from the simulation. The time base linearity was also verified by comparing these A-scan. The A-scan display of the simulated V2 calibration block was also compared to that of the experimental test. The comparison shows that both A-scan displays of simulation and experimental testing have a remarkable resemblance in a qualitative manner. However, the amplitude drop between the two back wall echo signals in the experimental test is significantly lower than that of the simulation.

Table of Contents

List of Figures

List of Tables

Chapter 1 Introduction

1.1 Motivation

Ultrasonic testing (UT) technique is one of the non-destructive testing and evaluation (NDT & E) techniques that play an important role in the integrity evaluation of the structures and pipelines in the oil & gas industry. Indeed, it provides vital information on the condition of the designed component during both fabrication and operations lifetime. The knowledge of the interaction of ultrasonic waves is employed to identify any potential weaknesses. The reflection of ultrasound from flaws with simple geometry and orientation has already been studied. However, for more complex cases, the reliability of the UT results is put under doubt. By increasing the demands of the UT technique in the challenging applications because of its advantages, the need for increasing the reliability of it rises. To verify the procedures and obtain robust results, software simulation is attached to the UT technique to predict the properties of waves in the complex geometry of the flaw and structure. The software uses discrete approaches such as Finite element (FE) methods to study the interactions of the ultrasound with discontinuities. Despite a vast variety of studies that have been performed in this area, there is still interest in the simulation of entire ultrasonic testing. This thesis is an attempt to model the three main components involving in the ultrasonic testing and study the effects of interfaces of them by using the finite element method. The probe and coupling media in the UT technique will be modeled and the performance of them will be studied. Besides, an experimental UT will be performed and the results will be compared with the simulation.

It should be noted that by the time of writing this thesis, the COVID 19 pandemic has been spread worldwide. So the limitation applied to the society has been influenced this thesis by limiting access to the library, licensed software, and laboratory equipment.

1.2 Background

Earlier attempts to study the wave propagation inside the solid medium is based on the elastic wave equations (EWE) driven from the equilibrium of the forces [15]. By developing computer programs, numerically solving the fundamental equations governing the motion of sound in materials absorbs scientists' attention. Soon, “wave displays” were produced by the results of EWE that show the complex ultrasonic behavior such as reflection, refraction, diffraction, and mode conversion inside the material.

In the ultrasonic testing technique, an ultrasound is fed to the specimen, and the echo signals are measured with the sensors. Although conceptually simple, results of the ultrasonic testing sometimes become confusing because of the complicated wave interactions with discontinuities. The echo signals are measured outside of the inspected object; then, the inspector infers the situation inside it. At early developments of the ultrasonic testing, inspectors did not have any vision about the behavior of

ultrasound facing with the complex discontinuities. By producing wave displays from the EWE, questions about what is going on inside the sample have answers [1]. Now, Inspectors can understand the complexities occurring inside the sample during the ultrasonic testing, instead of relying upon the measurements made outside of the sample. Besides, the ultrasonic testing simulation can provide a numerical A-scan display for a sample with different sizes or types [2].

However, the analytical approaches can only be performed for simple geometry problems. For generic shapes with arbitrary-shaped defects and specimen, discrete methods should be used. Boundary integrals [16] and the finite element method (FEM) [3] are potential candidates to simulate the ultrasonic propagation. Ihlenburg and Babuska [4] have been working on the link between the elastic wave equation and the dynamic equation of motion. Others such as Lord et al [3] and Richard et al [5] have developed the FEM application in ultrasonic modeling.

Soon, finite element parameters absorbed scientists' attention. The simulation parameters such as solving technique, mesh density, and time increment are the subject of many studies. Earlier studies are collected into books written in FEM such as the one written by Cook et al [22]. Later, Drozdz [31] performed a complete study on the effect of mesh density on the speed of sound in the solid medium. This study is performed for various element types and numerical schemes. Casadei et al [7] proposed formulations for multi-node elements capable of modeling small geometrical features to avoid excessive mesh refinements. Gao et al [8] introduced the finite discrete element method which is a marge of the finite element method (FEM) and discrete element method (DEM).

The finite element simulation of ultrasonic testing has its own problems. There are some factors governing its accuracy. Solving in the time domain, the element size should be limited to carry the wavelength leading to a large number of degrees of freedom and high analyzing time. Besides, the simulation is performed in a limited size in which the boundary reflection is inevitable. To make smaller models, a silent boundary condition was introduced. Cohen et al [9] introduced a silent boundary condition which later, it was used in Abaqus [30] benchmark problem in traducing the infinite element. Some years later, Drozdz [31] criticized its performance and introduced an absorbing layer in which the damping coefficient of elements gradually increased.

In the finite element program, mathematical equations are solved numerically by discretization in time and space domain, in wave propagation problems, which produces a discrepancy between the simulation values and the actual measurement in physical testing. Therefore, there is a tendency in the verification and validation of the numerical models. In the case of simulation of ultrasonic testing, researchers have been attempting to make their models verified and validated. Lakestani [10] was one of the early pioneers of the verification of ultrasonic simulation. Ame et al [6] have been conducting a research program to validate the simulations done by the UTDefect simulation program. Kim e al [11] proposed an efficient analytical modeling approach in angle beam ultrasonic testing simulation. They simplified an entire ultrasonic measurement process by assuming the transducer as a paraxial ray. They admitted that creating a simulation that can simulate the interface effects is a truly hard task. In the other study, Kim et al [12] conducted an immersion ultrasonic testing to model an ultrasonic pulse-echo method. They used the simplified modeling approach introduced in [11] to predict the echo signal of a flat-bottom hole. The results of both studies, [11] and [12], are verified by experiments. Recently, Dib et al [13] performed a prominent study to investigate the validation of the simulation done by CIVA software. It is a semi-analytical simulation platform developed by the French Commissariat à l'Energie Atomique (CEA) which is designed specifically for application in ultrasonic testing simulation. They modeled a vast variety of conventional ultrasonic transducers and compared the results with empirical data. They concluded that the CIVA models qualitatively provide reasonably

accurate results. However, they reported significant inaccuracy in quantitative reasoning applications such as the probability of detection studies or small flaws detectability.

1.3 Aim and objectives

This thesis aims to develop finite element simulations of ultrasonic testing in steel members. By applying the simulation in the Abaqus package, the characteristics of the ultrasound propagation through several media are also conducted. To achieve this goal, the following objectives need to be addressed:

1. Understanding the principle of the ultrasonic wave, reflection and transmission, and some important concepts of the wave propagation. As a result, the theoretical benchmark is developed to verify the simulation results.
2. Understanding the basic knowledge of the ultrasonic testing technique ranging from the methods, equipment principles, the procedure of inspection, important parameters, calibration concept, and other necessary information needed for simulation.
3. Understanding the basic knowledge about the finite element method and its important accuracy factors. Knowing how to apply a commercial finite element package in the modeling and simulating of ultrasonic waves in the media is essential.
4. Developing different finite element models containing the most important components of the ultrasonic testing technique. A probe, coupling, and specimen media are combined in the models. These models can provide a better understanding of the ultrasound propagation throughout these media. Visual observation of mode change of a wave in the interfaces as well as extracting information of several features of the models can be useful in studying the characteristics of the ultrasonic testing components like probe near-field zone.
5. Creating the A-scan display of the simulated ultrasonic testing, and finally, verify them by the actual ultrasonic testing.
6. Performing experimental ultrasonic testing to verify the simulation results.

1.4 Outline of the thesis

Following the objectives mentioned above, this thesis is divided into 8 chapters to address these issues.

- Chapter 2 covers the relevant theory of the thesis. The wave propagation in solid medium and related equations is introduced including the wave equation and wave reflection and transmission. Some important knowledge of ultrasonic testing is briefly described. These are important in the simulation of the ultrasonic testing technique and evaluation of its performances. Having information in the finite element method provides an understanding of the procedure of modeling and accuracy of the results.

- Chapter 3 introduces the objectives of the models and their geometries. Modeling procedures including the material properties, ultrasound pulse, and vital finite element modeling parameters are also described in this chapter. The results of the simulation are also presented in this chapter. Every aspect of the simulation is investigated and the results are provided in both visualization and recoded data. The propagation of the wave from generation in the probe to reflected echo is studied in detail. Besides, the probe characteristics such as near-field length, beam angle are extracted and shown in graphs and figures. Finally, the A-scan

display of the models is created based on the extracted data and the time base linearity of it is studied.

- In Chapter 4, the procedure of the experimental test is introduced. The results are prepared and the measured data is presented.

- The discussion of the results and verification are performed in Chapter 5. The obtained results are verified with theoretical values or references. The result of the simulation and the experimental test are compared and discussed. Finally, the source of difference between the simulation and experimental test or referenced values are explained.

- Chapter 6 contains the conclusions of the thesis and the possible improvements to this work. The most important findings in this work are summarised and highlighted.

Chapter 2 Theory

2.1 Fundamentals of wave propagation

2.1.1 The nature of an ultrasonic wave

Ultrasonic waves are a kind of mechanical vibrations system consisting of a mass and returning forces. These waves have frequencies above the audible range. In general, ultrasonic waves of frequency range 0.5 MHz to 20 MHz are used for the testing of materials. Since the presence of a mass is necessary to propagate an ultrasonic wave, they can propagate in solid, liquid, and gas but not in a vacuum [19]. However, Sound can travel in the form of a beam similar to that of light and follows many of the physical rules of light. An ultrasonic beam can be reflected, refracted, scattered, or diffracted.

To understand how ultrasonic waves propagate through a medium, we should look deeper into the mechanism which transfers the energy between two points in a medium. This could be done by considering the atomic model of an elastic material. All materials are made of atoms (or molecules) which are connected by interatomic forces. These atomic forces are elastic, i.e. the atoms can be considered to be connected as if through springs. A simplified model of such a material is shown in Figure 2-1 [14].

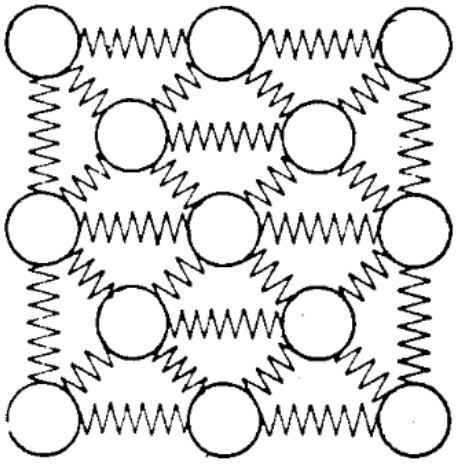

Figure 2-1 An atomic model of an elastic material [14]

Now like a mass-spring vibration system, by applying initial energy in the form of initial displacement of a force to an atom of material, it would start to vibrate with respect to its original position. Because of atomic interconnection, the adjacent atom will be caused to vibrate. This movement will continue the neighboring atoms up to the end of the medium.

2.1.2 Wave propagation in solid medium

The formulation of wave propagation through an un-damped infinite elastic solid medium is well-covered throughout literature and valuable texts [15], [16].

Although the study of the wave propagations in many applications involves complicated mathematical analysis that arises from geometrical complexities and material anisotropy, we strive to start with simplicity. The taut string is a basic physical system whose governing equation is simply understandable, and nearly all of the basic concepts of the wave propagation can and will be introduced by the taut string [15].

Consider a long or semi-long string which a free body diagram of an infinitesimally small element of it depicted in figure 2.2. All of the acting forces applied to it. The following is adapted from [15].

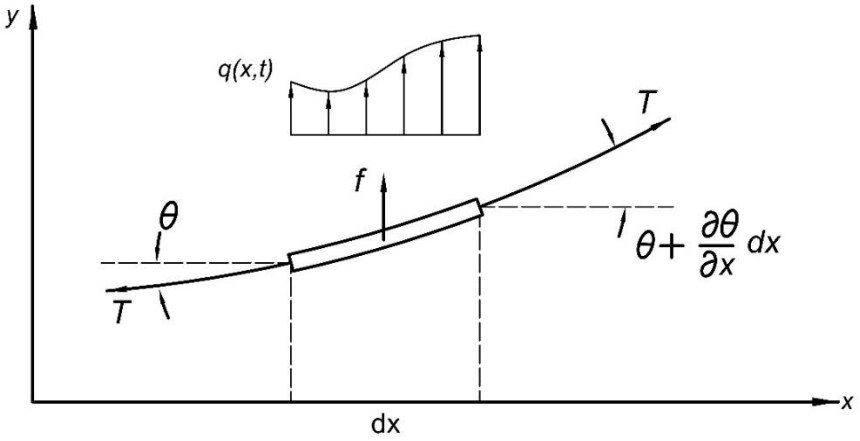

Figure 2-2 An element of a taut string

The wave equation of the string can simply derive by Newton's second law in the y-direction, thus we have

$$Ty_{,xx} + f - \rho\ddot{y} = -q(x,y) \qquad 2\text{-}1$$

Equation 2-1 can be rewritten by omitting body force as

$$y_{,xx} - \frac{1}{c_0^2}\ddot{y} = -\frac{q(x,y)}{T} \qquad 2\text{-}2$$

The above equation is called the wave equation in a string. This differential equation will be homogeneous when q=0, meaning that there is no external force acting on the system. Thus equation 2-2 reduces to

$$y_{,xx} - \frac{1}{c_0^2}\ddot{y} = 0 \qquad 2\text{-}3$$

This resulting equation governs the free motion of the string. It contains several elastic wave's fundamental properties that will be introduced here and their concepts are used in the rest of this thesis.

There are some solutions proposed to equation 2-3. The simplest one is by assuming the harmonic motion of the string in a way that the time and space domain domains are separated as two independent functions. Thus, let

$$y(x,t) = Y(x)T(t) \tag{2-4}$$

So by substituting it into equation 2-3, it gives

$$\frac{Y_{,xx}}{Y} = k^2 = \frac{\ddot{T}}{c_0^2 T} \tag{2-5}$$

or

$$Y_{,xx} + k^2 Y = 0 \tag{2-6}$$

and

$$\ddot{T} + \frac{k^2}{c_0^2} T = 0 \tag{2-7}$$

The resulting solution will be in the form of

$$y = A\cos\, k(x - c_0 t) = A\cos(kx - \omega t) = A\cos\, \varphi \tag{2-8}$$

The argument of equation 2-8 is designated as the phase φ , and A is the amplitude of the wave. By considering two situations of the wave where their phases are equal, giving

$$\varphi_1 = \varphi_2 \;\Rightarrow \Delta x - c_0 \Delta t = 0 \Rightarrow\; c_0 = \frac{\Delta x}{\Delta t} \tag{2-9}$$

This resulting equation is a well-known definition of velocity. Thus, c_0 is defined as a phase velocity of the wave. Phase velocity is a constant of the system describing the velocity of the particle.

Another representation of a harmonic wave could be the exponential form. Thus, let

$$y = Y(x)e^{i\omega t} \tag{2-10}$$

The solution comes by substituting into equation 2-3, giving

$$y = Ae^{i(kx-\omega t)} + Be^{-i(kx+\omega t)} \tag{2-11}$$

where the first and second terms are recognized as propagating waves in the positive and negative direction of x coordinate.

The successive distance between two points with the same phase is defined as wavelength, λ. At equation 2-8, k is defined as a wave number, and their relationship is

$$\lambda = 2\pi/k \tag{2-12}$$

Cyclic frequency, f and Period, T are some other quantities of a wave, where

$$\omega = 2\pi f = 2\pi/T \tag{2-13}$$

In this thesis, we will use frequency as a cyclic frequency. Finally, ω in equation 2-8 is defined as radial frequency, where

$$\omega = c_0 k \tag{2-14}$$

The general wave equation which can describe the true deformation of the material particles in a homogenous isotropic elastic solid is proposed by

$$\sigma_{ij,j} + \rho f_i = \rho \ddot{u}_i \quad \text{2-15}$$

where the relationship between the stress σ and strain ε in anisotropic material is given by the well-known Hooke's law

$$\sigma_{ij} = \lambda \delta_{ij} \varepsilon_{kk} + 2\mu \varepsilon_{ij} \quad \text{2-16}$$

$$\varepsilon_{ij} = \frac{1}{2}\left(u_{i,j} + u_{j,i}\right) \quad \text{2-17}$$

where the λ and μ are Lame' constants.

This equation emanates from Newton's second law by considering all of the forces acting on a differential element of the material. The displacement of a particle depends on its location and time. Thus, this differential equation should be solved in both of them. It is required that the wave equation expresses in terms of displacement, then equations 2-16 and 2-17 substitutes into equation 2-15 to reach the Naiver equation noting that body forces are omitted here

$$(\lambda + \mu) u_{i,ji} + \mu u_{i,ji} = \rho \ddot{u}_i \quad \text{2-18}$$

and in a vector form

$$(\lambda + \mu) \nabla \nabla . u + \mu \nabla^2 u = \rho \ddot{u} \quad \text{2-19}$$

and with rectangular scaler notation, it yields to three equations

$$\left.\begin{aligned}
(\lambda + \mu)\left(\frac{\partial^2 u}{\partial x^2} + \frac{\partial^2 v}{\partial x \partial y} + \frac{\partial^2 w}{\partial x \partial z}\right) + \mu \nabla^2 u = \rho \ddot{u} \\
(\lambda + \mu)\left(\frac{\partial^2 u}{\partial y \partial x} + \frac{\partial^2 v}{\partial y^2} + \frac{\partial^2 w}{\partial y \partial z}\right) + \mu \nabla^2 v = \rho \ddot{v} \\
(\lambda + \mu)\left(\frac{\partial^2 u}{\partial z \partial x} + \frac{\partial^2 v}{\partial z \partial y} + \frac{\partial^2 w}{\partial z^2}\right) + \mu \nabla^2 w = \rho \ddot{w}
\end{aligned}\right\} \quad \text{2-20}$$

Dealing with these equations in some problem because of its inherent complexity is difficult. To simplify them, a set of scaler and vector potentials ϕ and H are introduced due to Helmholtz theorem as

$$u = \nabla \phi + \nabla \times \mathrm{H} \quad \text{2-21}$$

$$\nabla . H = 0 \quad \text{2-22}$$

Equation 2-22 provides the condition in which the three components of u determined uniquely from Helmholtz decomposition potentials. Substituting equation 2-21 into equation 2-19 yields

$$\nabla\{(\lambda + 2\mu)\nabla^2 \phi - \rho \ddot{\phi}\} + \nabla \times (\mu \nabla^2 H - \rho \dot{H}) = 0 \quad \text{2-23}$$

Equation 2-23 will be satisfied in a case that both terms inside the bracket become zero, thus giving

$$(\lambda + 2\mu)\nabla^2 \phi - \rho \ddot{\phi} = 0 \Rightarrow \ddot{\phi} = \frac{\lambda + 2\mu}{\rho} \nabla^2 \phi = c_l^2 \nabla^2 \phi \quad \text{2-24}$$

$$\mu \nabla^2 H - \rho \dot{H} = 0 \Rightarrow \dot{H} = \frac{\mu}{\rho} \nabla^2 H = c_s^2 \nabla^2 H \quad \text{2-25}$$

From equation 2-24, we can conclude that a change in volume or dilatational disturbance travels with the speed of c_l. Similarly a rotational disturbance or non-volume waves propagate with velocity of c_s

resulting from eq. 10. We have seen that waves can propagate at an isotropic elastic material at two different types and speeds. Dilatational and rotational waves are also called longitudinal or primary waves (P-waves) and shear or secondary waves (S-waves). c_l and c_s are the material characteristics which depend only on Lame' constants λ and μ. By substituting there two constant into equation 2-24 and equation 2-25, giving

$$c_l = \sqrt{\frac{E(1-\nu)}{\rho(1+\nu)(1-2\nu)}} \quad and \quad c_s = \sqrt{\frac{E}{2\rho(1+\nu)}} \qquad 2\text{-}26$$

Furthermore, equation 2-24 and equation 2-25 reveals that these two longitudinal and shear waves can propagate independently throughout the medium. Thus the wavenumber and wavelength of them are different. By using equation 2-14, 2-13 and 2-12, we have

$$\mathrm{k}_l = \frac{\omega}{c_l} \ \& \ \mathrm{k}_s = \frac{\omega}{c_s} \qquad 2\text{-}27$$

$$\lambda_l = \frac{c_l}{f} \ \& \ \lambda_s = \frac{c_s}{f} \qquad 2\text{-}28$$

2.1.3 Acoustic features of ultrasonic wave

Similar to the solid medium, waves can also propagate through a fluid medium. These waves are originally small pressure disturbances in the fluids like air and water. However, unlike solid waves, acoustic waves or *sounds* can only propagate in longitudinal waves, thus no shear waves are imagined in a fluid due to lack of significant shear resistance. The sound waves have been the subject of many studies and their theory has been widely developed [17], [18]. Although the differential equations for sound waves are derived by fluid dynamic equations, the resulting solution is as the same language as the waves in solid medium. The purpose of this section is to introduce some important definitions, *plane wave*, *acoustic impedance*, and *acoustic intensity*, which are used in NDT.

- ***Plane-wave***

Plane-wave is defined as a wave whose particle motion is in the same direction as the normal of the "plane" [15]. It means that the wave even though it is 2D or 3D, looks like a one-dimensional wave whose acoustic fields depend on one specific coordinate [17]. Thus, the pressure field is constant along the pane of the wave.

- ***Acoustic impedance***

Acoustic impedance is a material resistance against motion pressure [14]. The essence of this measure comes from the inherent definition of "*impedance*" which is the ratio of frictional force to velocity [17][1]. For plane waves, the acoustic impedance is the same as specific acoustic impedance due to the constant pressure field [18]. It is a material property which is defined as

$$Z = \rho \, c_l \qquad 2\text{-}29$$

[1] In physics, impedance is defined as a ratio between "push" quantities such as voltage or pressure and its resulting "flow" quantities such as current or partial velocity [18].

where ρ is material density and c_l is longitudinal velocity defined in equation 2-26. The acoustic impedance can also be defined for shear velocity [16].

- ***Acoustic pressure***

This is a term mostly used in the acoustical study. However, its concept could be applicable for the wave propagation in solids. The definition of acoustic pressure refers back to the impedance definition where [18]

$$Z = \frac{p}{\dot{u}} \Rightarrow p(x,y,t) = Z\dot{u}(x,y,t) = Z\omega u(x,y,t) \quad 2\text{-}30$$

where $\dot{u}$ and u is the particle velocity and displacement, respectively. Thus, The pressure amplitude is

$$P = Z\omega A \quad 2\text{-}31$$

- ***Acoustic Intensity***

By imparting energy through the medium, it will be carried by the corresponding wave in the direction where it is traveling. Acoustic intensity is defined as a time average of energy flux in a specific direction [18]. It is defined as

$$I = \frac{P_{rms}^2}{Z} \quad 2\text{-}32$$

where P_{rms} is defined as the root-mean-square pressure as

$$P_{rms} = \left(\frac{1}{t_{av}}\int_0^{t_{av}} P^2 dt\right)^{1/2} \quad 2\text{-}33$$

where P is the pressure and t_{av} depends on the type of wave for instance for a periodic wave is period. In a case that the pressure field is a sinusoidal signal with amplitude A, equation 2-33 reduces to

$$P_{rms} = \frac{A}{\sqrt{2}} \quad 2\text{-}34$$

Thus the intensity is

$$I = \frac{A^2}{2Z} \quad 2\text{-}35$$

The definition of acoustic intensity in equation 2-35 is valid for the case of displacement field with the amplitude of A as well [16].

The acoustic intensity level is defined as a ratio of acoustic intensity over the intensity reference. It is often described in the logarithmic scale. It is

$$AIL = 10\log_{10}\frac{I}{I_{ref}} \quad 2\text{-}36$$

The unit is decibel or dB. We can rewrite it in terms of pressure and amplitude as

$$AIL = 20\log_{10}\frac{A}{A_{ref}} = 20\log_{10}\frac{P}{P_{ref}} \quad 2\text{-}37$$

when both P and P_{ref} have the same frequency.

2.1.4 Reflection and transmission

The behavior of waves accounting at the boundary of two different media is a phenomenon in which some portion of the incident wave's energy reflected and the rest transmitted to the adjacent medium. Depending on the angle of the incident, it was studied into normal and oblique. However, we will start with semi-infinite

2.1.4.1 Incident wave at the semi-infinite medium

Assume that P and S waves are propagating to the medium and their corresponding reflected waves are leaving the boundary as shown in Figure 2-3.

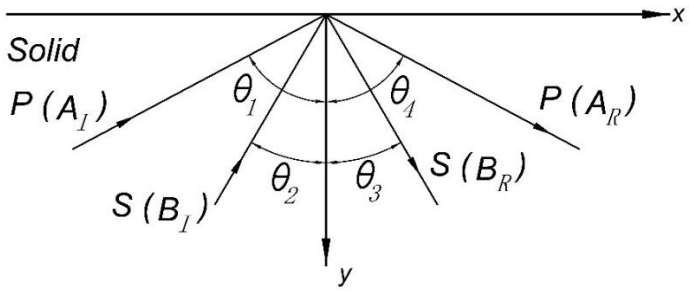

Figure 2-3 Wave reflection at the semi-infinite media
Incident P and S waves encountering at the medium edge and their corresponding reflections leaving

To derive the governing equations for this case, we begin with the study of the solution for the equation 2-24 and 2-25. It could be considered as an exponential harmonic wave for the plane strain case, where $u_z = \partial/\partial z = 0$, and let [15]

$$\phi = f(y)e^{i(k_{lx}x-\omega t)} \; and \; H = h(y)e^{i(k_{sx}x-\omega t)} \qquad 2\text{-}38$$

Substitution in the equations 2-24 and 2-25 gives

$$\phi = A_1 e^{i(k_{lx}x+k_{ly}y-\omega t)} + A_2 e^{i(k_{lx}x-k_{ly}y-\omega t)} \qquad 2\text{-}39$$

$$H = B_1 e^{i(k_{sx}x+k_{sy}y-\omega t)} + B_2 e^{i(k_{sx}x-k_{sy}y-\omega t)} \qquad 2\text{-}40$$

Where k_{lx}, k_{ly}, k_{sx}, and k_{sy} are defined as

$$k_{lx} = k_l \sin\theta_l \quad and \quad k_{ly} = k_l \cos\theta_l \qquad 2\text{-}41$$

$$k_{sx} = k_s \sin\theta_s \quad and \quad k_{sy} = k_s \cos\theta_s \qquad 2\text{-}42$$

where θ_l and θ_s are the angles of an arbitrary P and S waves in the Cartesian coordinate. The first and second terms of equations 2-39 and 2-40 are propagating wave in the positive and negative direction of x coordinate. Thus, for each of the waves in Figure 2-3, the potential functions are defined as

$$\phi_I = A_I e^{i(k_{lx}^I x-k_{ly}^I y-\omega t)} \quad and \quad H_I = B_I e^{i(k_{sx}^I x-k_{sy}^I y-\omega t)} \qquad 2\text{-}43$$

$$\phi_R = A_R e^{i(k_{lx}^R x+k_{ly}^R y-\omega t)} \quad and \quad H_R = B_R e^{i(k_{sx}^R x+k_{sy}^R y-\omega t)} \qquad 2\text{-}44$$

The displacements and stresses are obtained from potential equations by using equations 2-16, 2-17, 2-21 and 2-22, giving

$$u_x = \frac{\partial \phi}{\partial x} + \frac{\partial H}{\partial y} \quad and \quad u_y = \frac{\partial \phi}{\partial y} - \frac{\partial H}{\partial x} \tag{2-45}$$

$$\sigma_{xx} = (\lambda + 2\mu)\left(\frac{\partial u_x}{\partial x} + \frac{\partial u_y}{\partial y}\right) - 2\mu \frac{\partial u_y}{\partial y} \tag{2-46}$$

$$\sigma_{yy} = (\lambda + 2\mu)\left(\frac{\partial u_x}{\partial x} + \frac{\partial u_y}{\partial y}\right) - 2\mu \frac{\partial u_x}{\partial x} \tag{2-47}$$

$$\sigma_{xy} = \mu\left(\frac{\partial u_x}{\partial y} + \frac{\partial u_y}{\partial x}\right) \tag{2-48}$$

The results are derived by substituting equations 2-43 and 2-44 into 2-45, 2-46, 2-47, and 2-48 at y=0 and omitting the common term $e^{i(-\omega t)}$

$$u_x = ik_{lx}^I A_I e^{i(k_{lx}^I x)} - ik_{sy}^I B_I e^{i(k_{sx}^I x)} + ik_{lx}^R A_R e^{i(k_{lx}^R x)} + ik_{sy}^R B_R e^{i(k_{sx}^R x)} \tag{2-49}$$

$$u_y = -ik_{ly}^I A_I e^{i(k_{lx}^I x)} - ik_{sx}^I B_I e^{i(k_{sx}^I x)} + ik_{ly}^R A_R e^{i(k_{lx}^R x)} - ik_{sx}^R B_R e^{i(k_{sx}^R x)} \tag{2-50}$$

$$\begin{aligned}\sigma_{yy} = &-((\lambda + 2\mu)k_{ly}^{I\,2} + \lambda k_{lx}^{I\,2})A_I e^{i(k_{lx}^I x)} + 2\mu k_{sy}^I k_{sx}^I B_I e^{i(k_{sx}^I x)} \\ &- ((\lambda + 2\mu)k_{ly}^{R\,2} + \lambda k_{lx}^{R\,2})A_R e^{i(k_{lx}^R x)} - 2\mu k_{sy}^R k_{sx}^R B_R e^{i(k_{sx}^R x)}\end{aligned} \tag{2-51}$$

$$\begin{aligned}\sigma_{xy} = &\,2\mu k_{lx}^I k_{ly}^I A_I e^{i(k_{lx}^I x)} - 2\mu\left(k_{sy}^{I\,2} - k_{sx}^{I\,2}\right)B_I e^{i(k_{sx}^I x)} - 2\mu k_{lx}^R k_{ly}^R A_R e^{i(k_{lx}^R x)} \\ &- 2\mu\left(k_{sy}^{R\,2} - k_{sx}^{R\,2}\right)B_R e^{i(k_{sx}^R x)}\end{aligned} \tag{2-52}$$

Let us introduce the boundary conditions for the free edge medium

$$\sigma_{yy} = \sigma_{xy} = 0 \quad at \;\; y = 0 \tag{2-53}$$

Boundary condition in equation 2-53 should always be satisfied at every arbitrary *x*, then we must be able to factor out $e^{i(k_{lx}^I x)}$, $e^{i(k_{lx}^R x)}$, $e^{i(k_{sx}^I x)}$ and $e^{i(k_{sx}^R x)}$. This will only happen when

$$k_{lx}^I = k_{lx}^R = k_{sx}^I = k_{sx}^R = k_x \tag{2-54}$$

using equations 2-27, 2-28, 2-41 and 2-42, equation 2-54 is rewritten as

$$\frac{sin\,\theta_1}{c_l} = \frac{sin\,\theta_2}{c_s} = \frac{sin\,\theta_3}{c_s} = \frac{sin\,\theta_4}{c_l} \tag{2-55}$$

The resulting equation is well-known as *Snell's Law* for angle beam analysis. We derived it by using Helmholtz's potential functions and satisfying the conditions of particle displacement and stress at the boundary. It is also be derived by using trigonometry principals [3]. However, the result of both approaches is the same.

Equation 2-55 reveals that $\theta_1 = \theta_4$ and $\theta_2 = \theta_3$, so $k_{ly}^I = k_{ly}^R = k_{ly}$ and $k_{sy}^I = k_{sy}^R = k_{sy}$. The resulting displacement and stress equations could be introduced in the form of matrixes

$$\begin{bmatrix} u_x \\ u_y \\ \sigma_{yy} \\ \sigma_{xy} \end{bmatrix} = M \begin{bmatrix} A_I \\ B_I \\ A_R \\ B_R \end{bmatrix} \quad 2\text{-}56$$

where

$$M = [m_{i,j}] = \begin{bmatrix} ik_x & -ik_{sy} & ik_x & ik_{sy} \\ -ik_{ly} & -ik_x & ik_{ly} & -ik_x \\ -(\lambda+2\mu){k_{ly}}^2 - \lambda {k_x}^2 & 2\mu k_{sy} k_x & -(\lambda+2\mu){k_{ly}}^2 - \lambda {k_x}^2 & -2\mu k_{sy}\, k_x \\ 2\mu k_x k_{ly} & -2\mu\left({k_{sy}}^2 - {k_x}^2\right) & -2\mu k_x k_{ly} & -2\mu\left({k_{sy}}^2 - {k_x}^2\right) \end{bmatrix} \quad 2\text{-}57$$

The same solution will be obtained by assuming a fixed edge boundary condition where $u_x = u_y = 0$.

Let us consider a special case when only a P wave incidence exists, as shown in Figure 2-4 (a). This results if $B_I = 0$ in the wave component matrix 2-56.

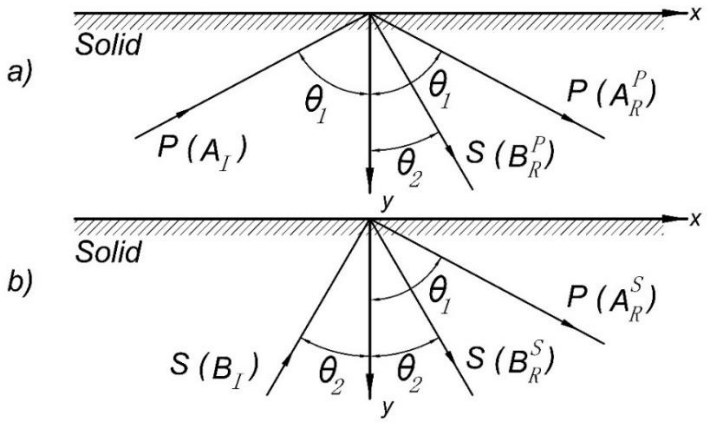

Figure 2-4 Wave reflection at the semi-infinite media
a) An incident P wave of amplitude A_I reflects in the mode of P wave of amplitude A_R^{SP} and S wave of amplitude B_R^P. b) An incident S wave of amplitude B_I reflects in the mode of P wave of amplitude A_R^S and S wave of amplitude B_R^S.

For the free edge boundary, the amplitude reflection coefficients are obtained by considering the zero stress field at the boundary, giving

$$R_P^P = \frac{A_R^P}{A_I} = \frac{\sin 2\theta_1 \sin 2\theta_2 - \alpha^2 \cos^2 2\theta_2}{\sin 2\theta_1 \sin 2\theta_2 + \alpha^2 \cos^2 2\theta_2} \quad 2\text{-}58$$

$$R_S^P = \frac{B_R^P}{A_I} = \frac{2 \sin 2\theta_1 \cos 2\theta_2}{\sin 2\theta_1 \sin 2\theta_2 + \alpha^2 \cos^2 2\theta_2} \quad 2\text{-}59$$

where R_P^P and R_S^P are P and S wave amplitude coefficient in P wave incidence, $\alpha = c_l/c_s$. We note that the angle of the reflected P wave is always equal to that of the incident P wave. Moreover, we know that $c_l > c_s$ is always true, then we conclude that $\theta_1 > \theta_2$ always.

The other case is that if $A_I = 0$, it means only S wave encounters the medium free boundary. It reflects in S wave at the same angle and P wave at $\theta_1$which is determined by equation 2-55 as illustrated in Figure 2-4 (b). The amplitude reflection coefficients are

$$R_P^S = \frac{A_R^S}{B_I} = \frac{-2\alpha^2 \sin 2\theta_2 \cos 2\theta_2}{\sin 2\theta_1 \sin 2\theta_2 + \alpha^2 \cos^2 2\theta_2} \quad 2\text{-}60$$

$$R_S^S = \frac{B_R^S}{B_I} = \frac{\sin 2\theta_1 \sin 2\theta_2 - \alpha^2 \cos^2 2\theta_2}{\sin 2\theta_1 \sin 2\theta_2 + \alpha^2 \cos^2 2\theta_2} \qquad 2\text{-}61$$

where R_P^S and R_S^S are P and S wave amplitude coefficient in S wave incidence. Similar to P wave incidence, we have $\theta_1 > \theta_2$ always. We note that the amplitude coefficients depend on Poisson's ratio and the angle of incidence.

2.1.4.2 Wave reflection and transmission at two semi-infinite interface

We now study the case where two semi-infinite media are in contact. In this case, not only the reflection and transmission but also mode conversion occurs. We specifically devote to the solid-fluid interface which is the case that we are dealing with in this thesis. The solid-fluid interface is of particular interest because the coupling between the probe and specimen in ultrasonic testing is a fluid. Thus, the generated waves at probe transfer to the specimen through a fluid coupling. For fluid, It was considered $\mu = 0$ to calculate wave speed. So there is only a longitudinal wave can propagate through fluids. It was mentioned indirectly through literature [14], [15], [20]. But it is specifically studied in [21]. This section will be investigated in two parts, incident P wave and S wave separately.

Consider solid and liquid media in contact where the properties of the solid medium are given by λ, μ, ρ and those of the liquid medium by λ_L, ρ_L. We start with a P wave incidence in solid traveling towards the boundary at the angle of θ_1 reflects in P and S waves at θ_1 and θ_2, respectively and transmits in only P wave in the fluid at β, as illustrated in Figure 2-5.

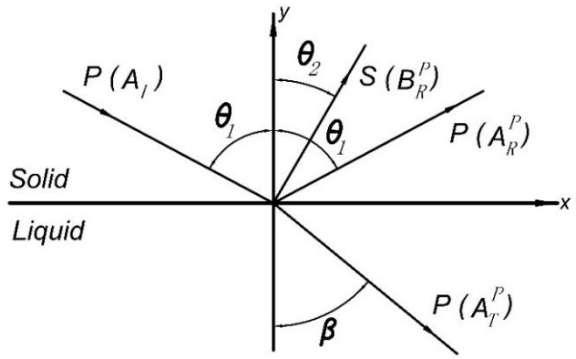

Figure 2-5 Reflection and transmission of a P wave at a solid-liquid interface
Reflection of an incident P wave of amplitude A_I from a solid medium to P wave of amplitude A_R^P and S wave of amplitude B_R^P and transmission to a P wave of amplitude A_T^P in fluid.

The equation of the reflected and transmitted wave can be derived by taking into account two boundary conditions, bonded media and slip faces, at the interface. The latter is of particular interest in the ultrasonic study where transducer and solid medium are coupled by a film of liquid [15]. There is another boundary condition where the displacement and particle velocity matches [16]. Here, we are about to use the slip boundary conditions which is given by

$$\sigma_{yy}^S = \sigma_{yy}^L = -P\,, \sigma_{xy}^S = 0,\ u_y^S = u_y^L \qquad 2\text{-}62$$

The governing equations for interface situation are derived by taking into account that equation 2-56 is valid for both semi-infinite media. Thus the reflection and transmission amplitudes are obtained by substituting equation 2-56 into 2-62. By rearranging it with knowns, P wave incidence amplitude A_I, $B_I = 0$ and unknowns, we have

$$\begin{bmatrix} m_{23}^S & m_{24}^S & -m_{23}^L \\ m_{33}^S & m_{34}^S & -m_{33}^L \\ m_{43}^S & m_{44}^S & 0 \end{bmatrix} \begin{bmatrix} A_R^P \\ B_R^P \\ A_T^P \end{bmatrix} = -A_I \begin{bmatrix} m_{21}^S \\ m_{31}^S \\ m_{41}^S \end{bmatrix} \quad \text{2-63}$$

where m_{ij}^S and m_{ij}^L are M matrix arrays by taking solid and liquid properties, respectively. The amplitude reflection and transmission coefficients are calculated by solving equation 2-64.

The relationship between the angles for the case of two semi-infinite media is also be derived from boundary conditions if one substitutes the general equations of displacements and stresses. The result is the Snell's Law for reflection and transmission which is

$$\frac{\sin\theta_1}{c_l} = \frac{\sin\theta_2}{c_s} = \frac{\sin\beta}{c_L} \quad \text{2-64}$$

where c_L is denoted as the speed of sound in the fluid. Here also, we can conclude that $\theta_1 > \theta_2$ always. This is because in solid, $c_l > c_s$.

Similarly, for S wave incidence as illustrated in Figure 2-6, the amplitude of reflected and transmitted waves could be derived by using the boundary conditions the same as equation 2-60.

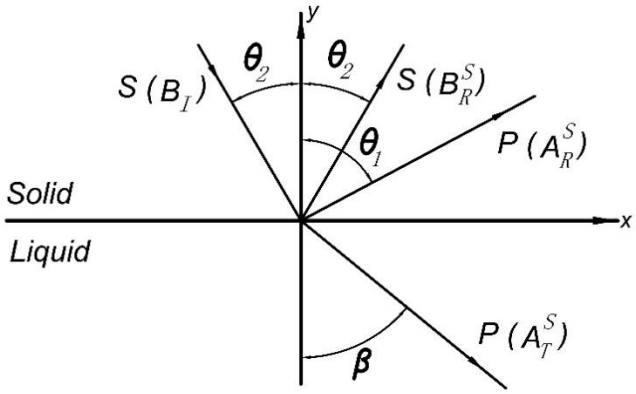

Figure 2-6 Reflection and transmission of an S wave at a solid-liquid interface
Reflection of an incident S wave of amplitude B_I from a solid medium to P wave of amplitude A_R^S and S wave of amplitude B_R^S and transmission to a P wave of amplitude A_T^S in liquid.

Again, by substituting equation 2-56 into 2-62 and taking $A_I = 0$, the equations in the matrix form are

$$\begin{bmatrix} m_{23}^S & m_{24}^S & -m_{23}^L \\ m_{33}^S & m_{34}^S & -m_{33}^L \\ m_{43}^S & m_{44}^S & 0 \end{bmatrix} \begin{bmatrix} A_R^S \\ B_R^S \\ A_T^S \end{bmatrix} = -B_I \begin{bmatrix} m_{22}^S \\ m_{32}^S \\ m_{42}^S \end{bmatrix} \quad \text{2-65}$$

Here, the coefficient matrix is the same as that of 2-63. The amplitude reflection and transmission coefficient are obtained by solving it.

Let us consider the case where the incident wave generated in liquid as shown in Figure 2-7 Reflection and transmission of a P wave at a liquid-solid interface.

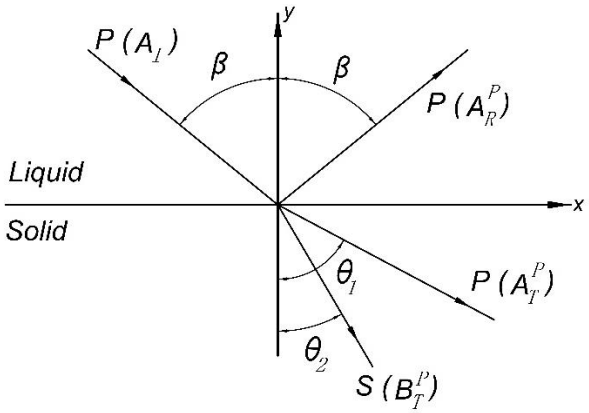

Figure 2-7 Reflection and transmission of a P wave at a liquid-solid interface
Reflection of an incident P wave of amplitude A_I from a liquid medium to P wave of amplitude A_R^p and transmission to a P wave of amplitude A_T^P and S wave of amplitude B_T^P in solid.

A similar approach can be taken to calculate the amplitudes. Thus we have

$$\begin{bmatrix} -m_{23}^L & m_{23}^S & m_{24}^S \\ -m_{33}^L & m_{33}^S & m_{34}^S \\ 0 & m_{43}^S & m_{44}^S \end{bmatrix} \begin{bmatrix} A_R^P \\ A_T^P \\ B_T^P \end{bmatrix} = A_I \begin{bmatrix} m_{21}^L \\ m_{31}^L \\ 0 \end{bmatrix} \quad 2\text{-}66$$

The special case of reflection and transmission is when an incident wave encountering an interface of two media with a direction normal to the interface, $\theta_1 = 0$. Then, the wave equation will simply reduce to a one-dimensional study. Therefore, the reflection and transmission coefficients will be

$$R^d = \frac{A_R}{A_I} = \frac{Z_1 - Z_2}{Z_2 + Z_1} \quad 2\text{-}67$$

$$T^d = \frac{A_T}{A_I} = \frac{2Z_2}{Z_2 + Z_1} \quad 2\text{-}68$$

R^d and T^d are the reflection and transmission coefficients in the displacement field. Similarly, the stress reflection and transmission coefficients, R^σ and T^σ respectively, are

$$R^\sigma = -\frac{\sigma_R}{\sigma_I} = \frac{Z_1 - Z_2}{Z_2 + Z_1} \quad 2\text{-}69$$

$$T^\sigma = \frac{\sigma_T}{\sigma_I} = \frac{2Z_2}{Z_2 + Z_1} \quad 2\text{-}70$$

We note that the coefficients for amplitude and stress are the same. In this context, normal stress interpreted as pressure. From equation 2-31, we know that pressure is linearly proportional to displacement amplitude. Therefore, the displacement amplitude coefficients are equal to that of pressure and stress. The minus behind the stress coefficient implies the direction of it with respect to the positive coordinate direction.

The reflection and transmission coefficient could be expressed in the term of intensity. By using equation 2-35 the coefficients are as follows

$$R^I = \frac{I_R}{I_I} = \frac{(Z_1 - Z_2)^2}{(Z_2 + Z_1)^2} \quad 2\text{-}71$$

$$T^I = \frac{I_T}{I_I} = \frac{4Z_2Z_1}{(Z_2 + Z_1)^2} \qquad 2\text{-}72$$

We can see that these coefficients depend only on acoustic impedance meaning that they are material characteristics. Consider two material with almost the same impedances, then the reflection and transmission coefficients approach to zero and one respectively. In this case, the majority of the wave energy passes to the other medium. These materials are said to be well-matched or coupled. On the other hand, two materials with significant differences in impedances are called miss-matched or uncoupled.

It is worthwhile to mention that equations 2-67 to 2-72 is also applicable for shear wave incident [16]. Here, one should use the shear wave speed in the impedance equation, 2-29. Besides, it covers the situation where one or both of the materials are fluid as well. In the case of shear incident wave strike normally to the solid-fluid interface, there is no wave transmitted to the fluid and the whole shear wave reflected to the solid.

The condition of the normal incident wave implies ultrasonic testing with a normal probe. It was showed that only 1.3 percent of the original sound energy comes back to the transducer after passing through water coupling and steel specimens [14]. Figure 2-8 represents the details of it.

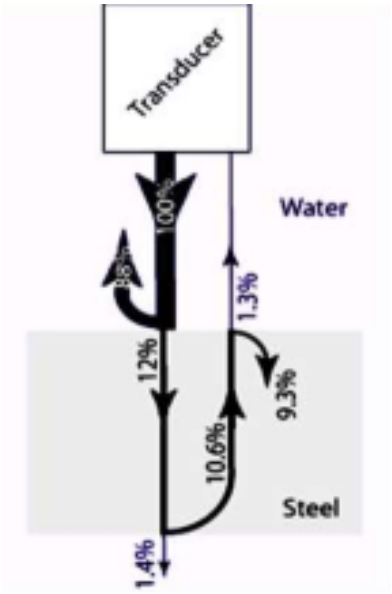

Figure 2-8 Reflection and transmission at normal incident [14]
The percentage of the original sound energy in reflection and transmission in two different materials, water and steel.

2.1.4.3 Critical incident angles

We have seen in 2.1.4.2 that $\theta_2 < \theta_1$ always. Now, there is a case in which $\theta_1 = 90^\circ$. Then, θ_{cr}^1 is defined as first critical angle which is calculated from Snell's Law in equation 2-64, giving

$$\theta_{cr}^1 = \beta = \sin^{-1}\frac{c_L}{c_l} \qquad 2\text{-}73$$

We chose a liquid-solid interface to represent this section because in our case the only situation where P wave vanishes in the specimen is when the wave passes from liquid coupling and transmitted into the specimen.

The second critical angle, on the other hand, is defined when $\theta_2 = 90^\circ$. Recalling equation 2-64, we have

$$\theta_{cr}^{2} = \beta = \sin^{-1}\frac{c_L}{c_s} \qquad 2\text{-}74$$

This can happen if $c_s > c_L$. It means that the shear wave velocity in solid should be larger than a longitudinal wave in a liquid, otherwise the second critical angel does not exist. Moreover, transmitted waves with an angle of 90 degrees are no longer body waves. They are categorized as surface waves [15].

2.2 Ultrasonic nondestructive testing

Ultrasonic testing is a nondestructive testing (NDT) technique in which a high-frequency elastic wave is fed into the metals to inspect its condition. Some discontinuities such as inclusions or cracks may exist or develop in the metals due to its production procedures or the operation lifetime. These discontinuities which are sometimes called flaws create different characteristics in metals. As we have seen in the previous section, the ultrasonic waves encountering discontinuities are disturbed as well. Reflection, transmission, and diffraction can happen for the ultrasonic wave in this situation. Monitoring these phenomena, in particular reflection, builds the basis of ultrasonic testing. The degree of reflection depends mostly on the geometry of the flaw. Thus, the status of the flaw is analyzed by studying its reflection behavior.

The ultrasonic testing has some advantages and disadvantages compared to other methods of NDT testing. This technique utilizes a high-frequency wave that can propagate at the surface or subsurface of the material which can detect almost all kinds of flaws even those with extremely small size. Moreover, its application is relatively simple and hazardless, for example, it can be done by having access only on one side of the specimen. The electronic operation allows us to have an immediate interpretation. Ultrasonic testing allows for the nonhazardous operation to the personnel and nearby equipment. However, skillful and trained personnel is needed to perform ultrasonic testing. Besides, some flaws that have dispersive reflective faces or locates in the anisotropic materials are difficult to detect. Last but not least, ultrasonic test responses from flaws not the shape or size of the flow inherently. In this respect, flaw type is interoperated from the received signal in comparison with some reference flaw signals.

This technique has been developed and used for metal nondestructive testing and other inspection applications such as medical sonography. Its principals and methods are well-covered in the several documents [14], [22], [23], [24]. This section will represent some major aspects of it related to its applications in FE modeling.

2.2.1 Methods and instruments for ultrasonic testing

Ultrasonic testing is applicable to various types of inspection programs. Thus, several methods and their instruments are developed for particular usage on dedicated applications. The transmission method, pulse-echo method, and resonance method are some of the important ones. Among them, pulse-echo is of particular interest in the ultrasonic inspection. The FE modeling presented in the following chapters is on the pulse-echo method.

2.2.1.1 Pulse-echo method

Pulse-echo method is widely used in ultrasonic testing. It involves the use of one probe as the transmitter and receiver of ultrasonic signals. A short burst of ultrasonic energy is fed in the specimen at a regular interval of time. If the pulses encounter a reflector, some or all of the energy is reflected towards the receiver and measured. The reflected energy depends on the shape and orientation of

the flaw. The reflection energy as well as the time delay between transmitting and receiving are measured.

2.2.1.2 Electronic instruments of the ultrasonic testing

Ultrasonic testing is inherently done by using electronic devices which transfer an electronic pulse to mechanical waves. Devoting specifically on the details of the instruments is out of the scope of this work, but understanding its principle is essential since almost the same procedure will be applied for modeling the ultrasonic test by using the finite element method. The instruments represented here are limited to those of the pulse-echo method. Generally, in the pulse-echo method, there is two major equipment require, flaw detector system and probe, which is connected by a cable.

- Flaw detector system

A flaw detector system is a device responsible for generating and receiving electronic pulses. The electric voltage pulse is fed to the probe through a test cable to be transferred to the mechanical wave. The mechanical wave echo receives to the probe and after transferring to the electronic pulses, they are displayed after amplifying and noise filtering.

The components of a flaw detector system are shown in Figure 2-9. A clock triggers a sweep generator and a pulser unit. As the electronic pulse supplied to the probe, it is also fed to the receiver unit to display at the screen as indication ‘a’ in Figure 2-9. This indication is known as a transmission pulse. The input pulse often varies between 300-1000 V applied to the probe at regular intervals. These intervals which are sometimes called repetition frequency or pulse repetition frequency varies between 60 and 2000 hertz. The importance of repetition frequency is for achieving the maximum response of the probe, resonance repetition frequency of the probe, and maximum signal-to-noise ratio in the electronic equipment, lowest noise of electronic devices. Moreover, repetition frequency should be set in a way that the previously generated pulse comes back to the receiver and is displayed. The time between the intervals should be larger than the time the generated pulse travels inside the specimen. In most of the commercially available equipment, this is controlled automatically.

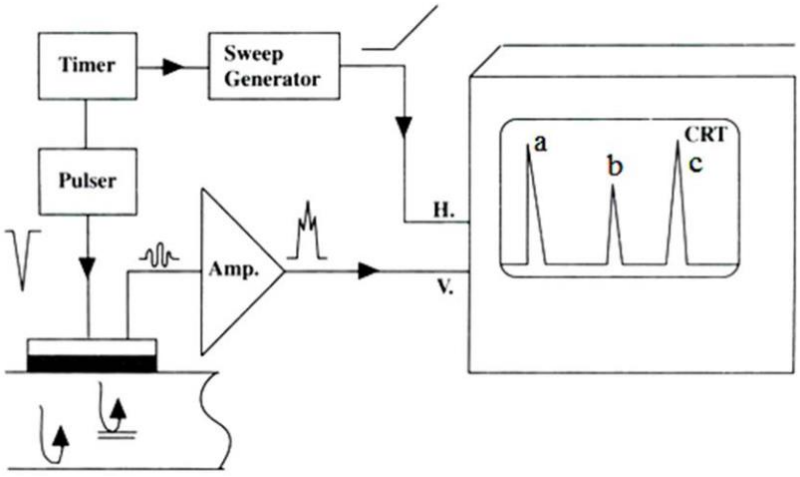

Figure 2-9 Basic component of an ultrasonic flaw detector system [14]

The ultrasonic wave, when facing a defect or back wall, reflects to the probe and transfers to an electronic pulse creating ‘b’ and ‘c’ indicates on the screen as shown in Figure 2-9, respectively. The time of receiving each echo is recorded by the clock triggered the pulser.

The initial pulse will pass through several media and reflects along the same path to the receiver. As we have seen in Figure 2-8, only 1.3 percent of the initial energy is received by the probe. This assumes

ideal reflection and transmission, which means no refraction, absorption, ideal isotropic material property, and smooth reflector. Thus, the received signal is comparatively weak, approximately 1/1000 to 1 V. This weak signal should be amplified before displayed into the screen.

Generally, there are two types of amplifiers in the term of signal amplification. Firstly, the basic amplification method is a linear amplification. It consists of representing the height of the echo linearly proportional to the input voltage level. Secondly, the common amplification is the logarithmic proportion for which the echo height is represented as the logarithm of the probe voltage.

Besides, amplifier units can be tuned to strengthen the amplitude of the specific frequency range of the probe voltage. Since noises are inevitable in the response voltage, it is necessary to amplify frequencies that carry the valuable flaw echo. It could be set in a narrowband or wideband frequency range. It is quite sensible that the flaw echo may have the frequency range the same as the initial pulse. Thus, it is appropriate to set the amplifier in a narrowband frequency range as the initial pulse.

It is common in electronics to compare the voltage or power by the ratio of its initial pulse. Since the echo signal is significantly weak, it is more concise to express it on a logarithmic scale. It is a dimensionless unit for relative power or intensity which is called *Bel* or sometimes 10 times of it, decibel. This quantity is well-known as gain, sensitivity, or attenuator which is defined as

$$Gain = 10 \log_{10} \frac{E_2}{E_1} \qquad 2\text{-}75$$

Where E is the electric energy of the input or output signal. This equation is the same as we defined in equation 2-36 in the *Acoustic Intensity Level*. Since both of them are in terms of energy, Gain can be defined as Acoustic Intensity Level in ultrasonic testing. Thus, from equation 2-37, we can define

$$Gain = 20 \log_{10} \frac{A}{A_{ref}} = 20 \log_{10} \frac{P}{P_{ref}} \qquad 2\text{-}76$$

where A and P are the displacement and acoustic pressure amplitude, respectively.

Signals supplied to and received from the probe are some cycles of alternating positive and negative voltage. These signals can be displayed on the screen directly from the amplifier, but the measurement of their amplitudes is a bit cumbersome as it needs to be measured both in negative and positive directions. So, it is more convenient to display them in an only positive direction. To do this, the envelope of the signal is smoothed out after its half-negative cycles are inverted. This process is called signal rectifying.

- Probe

An ultrasonic sensor is a device that transfers an electronic pulse into a mechanical pulse and vice versa. It is normally called an ultrasonic probe. The ultrasonic wave is generated in the probe and radiated to the test piece. Depending on its angle, probes are classified into two major categories, normal and angle probe. As the name of them implying, the normal probe radiates the ultrasonic waves at the right angle to the test piece, whereas in case of angle probe, the waves entering into it obliquely.

We are about to model the angle probes in our work to generate ultrasonic waves. Hens, it is necessary to understand its components. The components angle probe is illustrated in Figure 2-10.

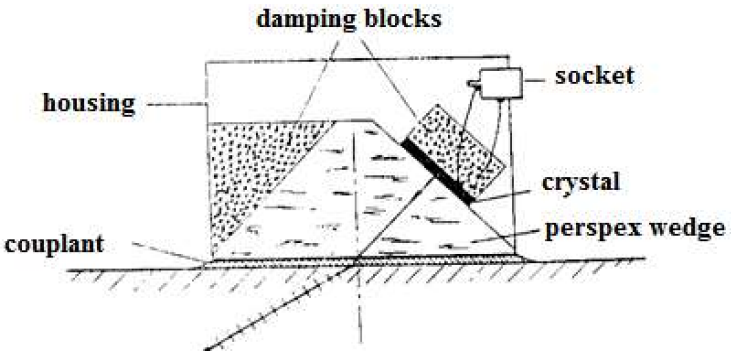

Figure 2-10 Angle probe components [14]

The angle probe consists of three main components, piezoelectric transducer, perspex wedge, and damping blocks. The electronic pulse triggers the piezoelectric material to vibrate and generates a mechanical wave that is reflected and transmitted to the test piece after passing through the perspex wedge.

The piezoelectric effect is a phenomenon in which electrical energy converts into a mechanical one and vice versa. It is exhibited by piezoelectric materials in which the center of negative and positive charges are unbalanced. Consequently, a spontaneous dipole moment exists inherently in these materials. When an external pressure applied in the polar direction, an electric potential difference between the two faces perpendicular to the polar direction creates to neutralize change in dipole moment because of the applied force. Strain in the polar moment direction is linearly varying by electric charge. The ratio of the strain and electric charge is constant, which is known as a piezoelectric constant. Thus, we can conclude that the voltage on the piezoelectric material can be obtained by a constant coefficient of particle displacement. This implies that instead of working with piezoelectric voltage, we can focus on the particle displacement. Consequently, there is no need to simulate the piezoelectric part in our model, and this has not been a part of this work.

The piezoelectric transducer can be made of several materials showing this effect. Generally, these materials are referred to as *crystals* in ultrasonic probes. Construction of the crystal shape depends on the application of the probe. The crystal disc is mostly used in normal probes, whereas the angle probes may be constructed form rectangular piezoelectric crystals. They are also adopted in a carved plate or concave disc for sound focusing applications.

An important question here will be how sound frequency generates in crystals. When a short voltage pulse applied to the crystal, it starts to deform in response. This response is a vibration response to the initial condition along the thickness of the crystal. In fact, the crystal starts ringing at its natural vibration resonance frequency. Thus, the frequency of the ultrasonic wave is determined by the natural frequency of the crystal at the thickness direction. The thinner crystal, the higher frequency ultrasound generated. For example, for 1 MHz frequency probe, the crystal thickness will be 2.98 mm; and for 10 MHz, 0.298 mm. Handling ultrahigh-frequency crystals have their difficulties since they are extremely fragile.

To introduce an angle beam into the test piece, the incident wave should strike the boundary with an inclination. Since it is convenient to use crystals generating P wave for contact probes, the radiated wave will encounter the surface of the test piece obliquely using a perspex wedge. It is needed to have a shear wave transmitted to the test piece and get rid of the P-wave to reach the best conditions for signal interpretation. Therefore, radiated waves should have an angle between the first and second critical angle.

In addition to wave mode conversion, we also have reflected waves in the wedge. These waves will be in the modes P and S wave as described in section 2.1.4. Their existence inside the limited area of the probe will cause some reflection echoes which potentially can disturb and mask inspection signals from the material. Thus, damping blocks are added on to the wedge at the beam path of the reflected waves and to absorb their energy. Their material is selected to have the best acoustic match to the wedge material, and at the same time high acoustic absorption ability.

The vibration of the crystal is not ideally uniform along the crystal length. Each point on the crystal face vibrates in the same direction, but they can be slightly out of phase with its neighbors. This can be explained through the Huygens principle. Each element on the crystal acts as a single point source and radiates a spherical wave from the plane of the crystal face. The interactions between these spherical waves produce a plane wave in front of the crystal traveling outwards. By entering the test piece, the order of these spherical waves is disturbed and consequently, their interactions near the face of the probe create amplitude fluctuations. It takes some distance by propagating away to rearrange together and make a strong wavefront. This distance in ultrasonic is called near field zone, and beyond that will be the far-field zone of the probe.

Wave radiation of an angle probe is illustrated in Figure 2-11. The definition of the near field id the area where interference phenomenon occurs resulting in several maxima in the radiation field of the probe. Sound distribution is unpredictable in this area. The length is defined as a distance from the probe to the position of the last maximum amplitude that occurred due to the interference.

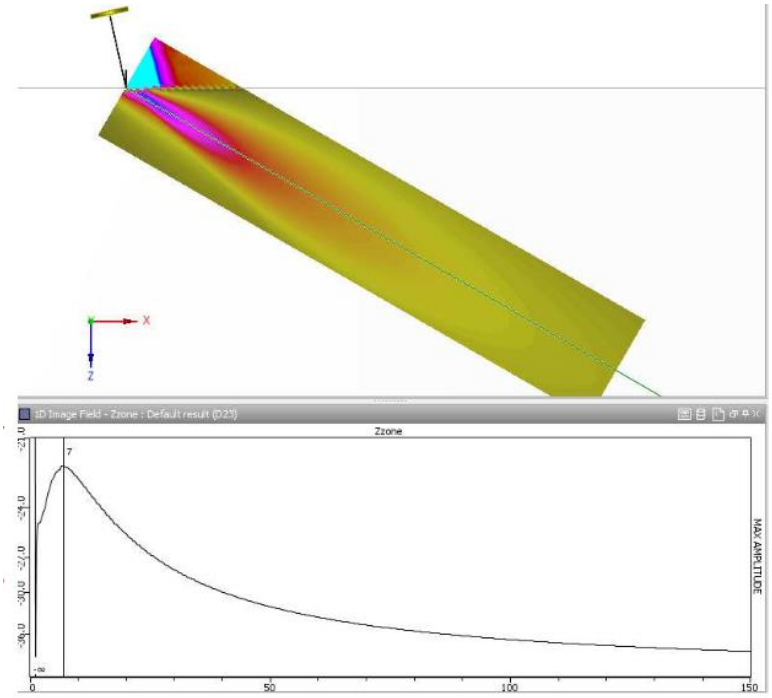

Figure 2-11 A 60º angle probe radiation field [25]
Radiation field and pressure distribution of a 60º angle probe modeled in CIVA, top view, and the pressure distribution along the probe center line, bottom view.

The near field length depends on several parameters. Crystal shape and dimensions, wave frequency, and speed of sound are the most important ones for the determination of the probe near field zone.

2.2.2 Ultrasonic Pulse

As mentioned along with the wave generation in the piezoelectric crystal in the previous section, the generated wave is a dynamic response for the applied excitation charge. This response is in the type

of forced vibration which produces a wave with multiple frequencies. These frequencies are referred to as frequency band or *bandwidth* of the probe. The bandwidth of the probe has a central frequency that carries the most energy of the pulse and defined by the upper limit frequency and the lower limit frequency. Upper and lower limits are usually defined as the frequencies at which the amplitude reduces 50% or -6dB. The frequency spectrum of the MWB60-N4 is shown in Figure 2-12.

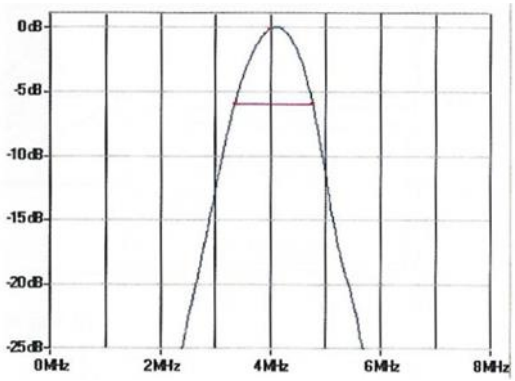

Figure 2-12 Frequency spectrum for MWB60-N4 [26]

The probe has a wide frequency range is called broad bandwidth, whereas the less frequency content spectrum is called narrow bandwidth. To express the bandwidth, a quantity is defined as probe quality factor which is

$$Q = \frac{f_0}{f_2 - f_1} \qquad 2\text{-}77$$

where f_0 is the central frequency, f_2 is the upper -6db frequency, and f_1 is the lower -6dB frequency. The quality factor for the MWB60-N4 probe is calculated at about 2.77. For ultrasonic application, the Q factor varies usually between 1 and 10.

The corresponding pulse shape for the spectrum in Figure 2-12 is known as a Hanning window pulse. The shape of the pulse is illustrated in Figure 2-13. This is a 6 cycles of Hanning window pulse which can simulate mathematically as

$$F(t) = 0.5 \times \sin(\omega t)(1 - \cos(\frac{1}{6}\omega t)) \qquad 2\text{-}78$$

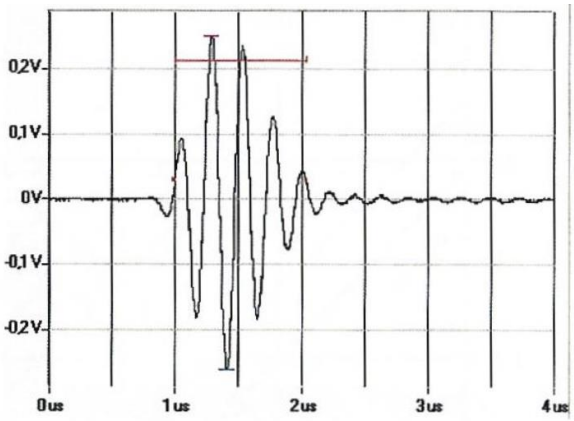

Figure 2-13 Pulse shape for MWB60-N4 [26]

2.2.3 Coupling

In the ultrasonic testing by using the contact probe, the gap between the test piece and probe is filled by air. The acoustic impedance of the air and solid materials largely different. Due to this, almost no wave energy transfers into the material, as almost all energy is reflected according to equations 2-71 and 2-72. Therefore, it is necessary to replace the air gap with a material with higher acoustic impedance. It is better to use liquids such as glycerin, water, oil, grease, etc. The selection of an appropriate coupling liquid depends on the surface roughness, operation temperature, the chemical reaction between the test piece and coupling, and cleaning matters.

Figure 2-14 shows the sensitivity of the signal amplitude by variation of coupling thickness. Ginzel [27] conducted an experimental test in an immersion set up to illustrate the effect of the coupling gap. The test is done on a steel block with a 45° bevel at one end, and a 12.5mm diameter probe providing a 45° refracted angle with a 5MHz was installed on the steel block facing the bevel. The probe was placed on the steel block by a holder to provide the desired gap thickness. The test components were placed in a tank filled with water as shown in Figure 2-14, right picture. The amplitude of the pulse-echo signal from the bevel was then monitored with respect to the vertical position. In Figure 2-14, the plot on the left indicates the amplitude (in volts) versus the distance from the steel plate surface with the probe underwater during the movement. The thickness of the water gap varies between 0 and 0.5mm. For the zero position, the amplitude was recorded at about 0.7V. By increasing the gap to the 0.1 mm the value starts to drop; and by the time the water gap is 0.25mm the voltage has dropped to 0.2V. The voltage rises to 0.4V when the gap increases to 0.3mm and then constantly drops as the gap thickness reaches just over 0.5mm.

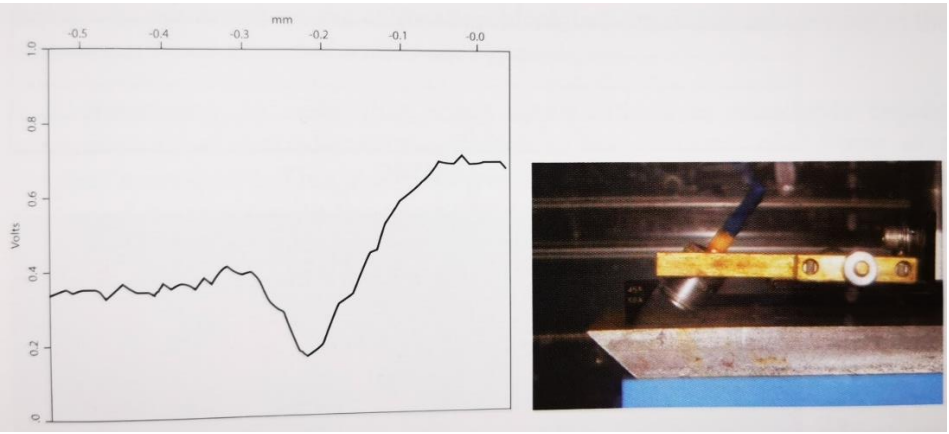

Figure 2-14 The effect of coupling gap in signal amplitude [27]

Ginzel concluded that by approaching a gap thickness of half a wavelength equivalent in water, the reduction of the voltage increases. The interface effect is reduced by increasing the gap thickness more than half wavelength, but the impedance mismatch prevents the signal to rise to its zero position value and causes to gradually reduction after increasing signal amplitude.

The effect of the coupling medium bolds when the surface roughness of the test piece is considered. Figure 2-15 shows the variation of echo amplitude in different surface roughness values for some types of couplings. It is obvious that the increase in surface roughness, the decrease in echo amplitude. However, a relatively smooth surface does not have a significant effect on the echo.

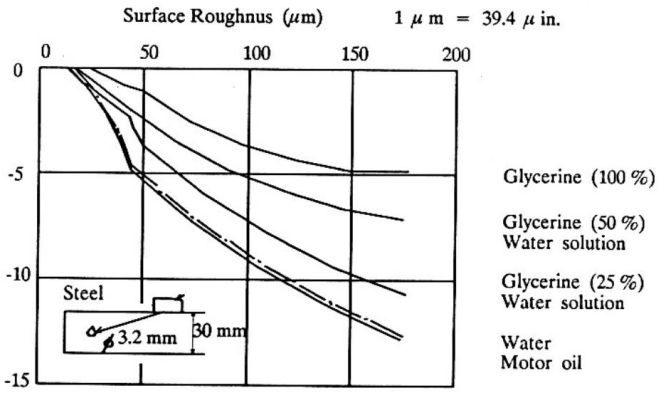

Figure 2-15 The effect of surface roughness of a test piece on signal amplitude [14]

2.2.4 Attenuation of ultrasonic waves

As mentioned earlier, the received echo from any reflector is significantly weak. That is because of attenuation or loss of sound energy traveling inside and through the medium. The attenuation of sound can be classified into three following categories:

- Transmission losses

Transmission losses involve the dispersion of sound energy due to absorption, scattering, and effect of impedance difference. Absorption can be imagined as a braking action on the motion of particles. This implies the damping effect in which the mechanical energy transfers to the heat even in the homogenous materials. The amount of the absorption effect depends on the material type and motion amplitude. In addition to absorption, scattering of ultrasonic wave mostly occurs in materials which are not completely homogenous. Small material discontinuities such as grain boundaries, twin boundaries, and minute nonmetallic inclusions, reflects a small amount of sound energy away from wavefront. Scattering effects highly depends on the ratio of material crystal size to wavelength. When this ratio is less than 0.01, scattering can be neglected. Lastly, Attenuation due to acoustic mismatch occurs in the boundary of two different materials, and consequently, some portion of wave energy transmitted as represents in Figure 2-8.

- Interference losses

Attenuation due to wave interference includes diffraction and phenomenon in which wave fringes, phase shift, or frequency shift happens. When a wave passes the edge of the reflector, it bends behind the edge in a spherical or cylindrical pattern. In other words, plane wave pattern breaks behind the reflector surface. In a case that reflector size is relatively small compared to the wavelength, implying a pore or inclusion, the wave bends behind it causes an interference pattern. This is because of the superposition of the in-phase and out of phase waves creating maximum and minimum intensity, respectively.

- Beam Spreading

In a point source wave, the propagation pattern is several or cylindrical. The constant wave energy spreads on the surface on these patterns and decreases by propagating away from the source. If a reflector exists in a distance from the source, an only small portion of the energy will be detectable at the source point.

These attenuation types not only influenced the quality of the echo signal but also create some small and random noise in the receiving signal. These unwanted noise signals cannot be avoided since there

is no way to remove their sources. Some ultrasonic flaw detectors are designed to recognize and remove noise signals by applying noise filtering systems.

2.2.5 Noise in ultrasonic testing

In addition to transmission losses, the flaw detector's electronic circuits can be a potential source of the noise. Pre-amplifier, transducer, transmitter/receiver switch, low noise amplifier, variable-gain amplifier, etc are the main sources of noise produced by electronic devices.

Generally speaking, noise is a small, randomly, fluctuating signal which is unwanted but present at the physical system. It masks the valuable signal from the defect. therefore, it is necessary to extract the defect echo through the noised signals.

The received signal can be defined in the form of

$$x(\boldsymbol{t}) = \boldsymbol{s}(\boldsymbol{t}) + \boldsymbol{n}(\boldsymbol{t}) \qquad 2\text{-}79$$

where s(t) is the defect echo and n(t) is noise [28]. In practical testing, noise can be filtered out by signal processing procedures. The common signal processing methods used in ultrasonic testing consist of the wavelet transform, spectrum transform, Hilbert-Huang transform, and split spectrum transform [29]. Studying about them is beyond the scope of this thesis, but it can briefly say that their principals based on the response frequencies of the defect echo which allows them to distinguish from the noise signals.

2.2.6 Flaw detection

The main aim of the ultrasonic testing in materials is to inspect the condition. During previous sections, it is apparent that neither the time base nor voltage recordings have any absolute meaning by themselves. So, these recordings should be processed to release their information.

The screen of the conventional ultrasonic flaw detector devices displays information in the horizontal and vertical axis. The horizontal axis is adjusted to represent the depth of the reflector based on the beam traveling time and material sound speed. The vertical axis, on the other hand, gives an indication of the amplitude of the detected signal represented by the *gain* being used. These horizontal and vertical axis provides a signal representation so-called *A-scan* display. The A-scan is the basic ultrasonic display that provides information about where the reflector is located. Nevertheless, it does not necessarily indicate the size and shape of the defect.

2.2.6.1 Calibration of the testing system

Since the A-scan representation is constructed based on the recorded data by transferring the time-base data to distance-based data, it needs to be calibrated before doing the test to standardize the inspection for a given material and specific performance. In fact, the calibration is the assurance that the results are accurate, reliable, and reproducible. The calibration in ultrasonic testing is classified into three following categories:

- Equipment characteristics verification
- Range calibration
- Reference level or sensitivity setting

Standards specify some prequalified blocks to achieve the above three objectives. The most versatile calibration blocks are the V1 and V2 blocks illustrated in Figure 2-16 and Figure 2-17, respectively, as described by the International Institute of welding, I.I.W.

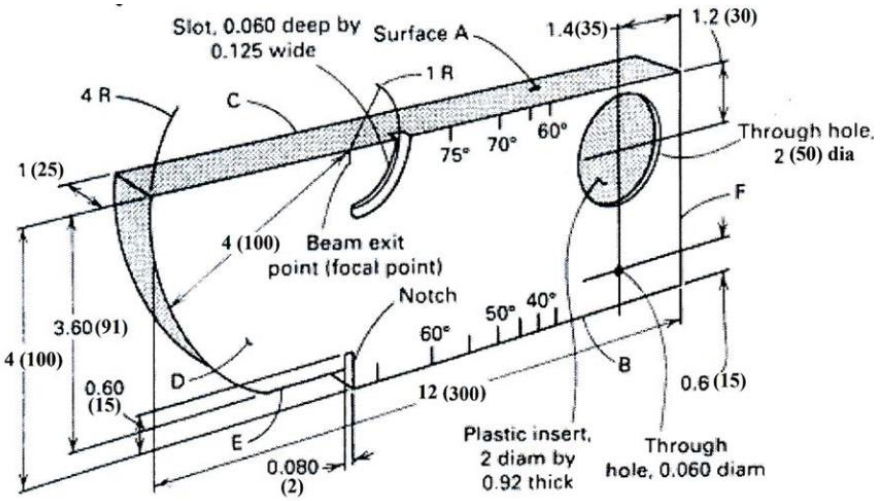

Figure 2-16 The V1 calibration block in the International Institute of welding [14]

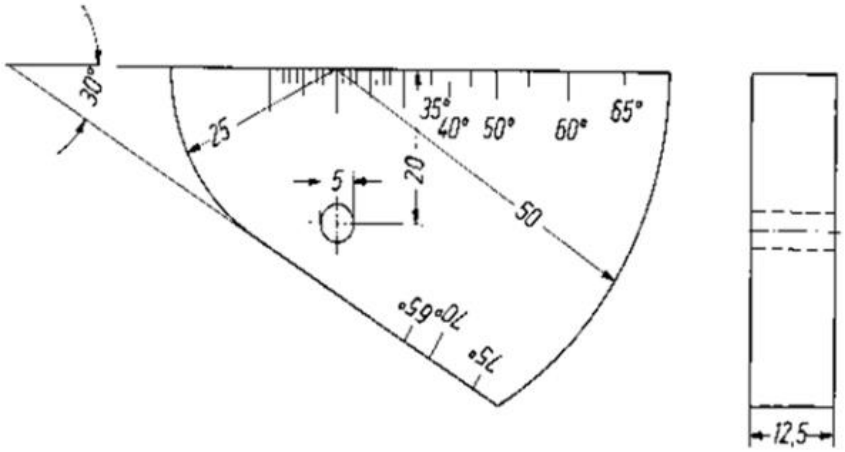

Figure 2-17 The V2 calibration block in the International Institute of welding [14]

2.2.6.2 Calibration of the angle probe

As the angle probe in our work will be evaluated within this work. It is necessary to introduce the calibration procedures for these types of probes. Generally, three types of calibrations are performed for the angle probes, consisting of the calibration of the time base, determination of the probe index, and determination of the probe angle. The two latter are the main controlling concept.

- Calibration of time base

The calibration of the time base is necessary to make sure that the distance between two signals, i.e. the transmitted signal and the echo are fitted to the scale of the screen horizontal scale. In order to understand the concept of the time base calibration procedure by using the I.I.W. V1 block, the beam path can be investigated. The ultrasonic beam leaves the probe face and heads towards the 100 mm radius. The ultrasound reflects and activates the probe's crystal producing the first echo indication on the screen of the ultrasonic flaw detector. Some portion of the beam reflects at the surface of below the probe towards the 25mm radius and comes back to the probe interface. However, the probe cannot detect this echo since it is orientated at 90 degrees of the sound direction. The beam reflects from the surface below the probe towards the 100mm radius for the second time and this reflection is detectable by the probe's crystal producing the second echo indication. Thus, the first and second echo travels 200 and 450 mm, respectively. The beam path is illustrated in Figure 2-18. Thus, the time

base should be calibrated in a way that those two signals will be indicated on the screen of the ultrasonic flaw detector at their actual distances which are 100 and 225 mm, respectively.

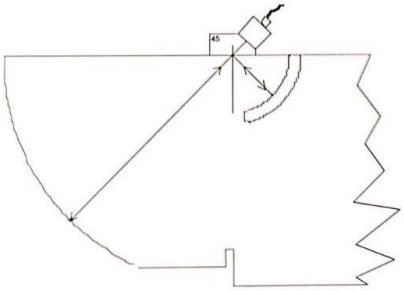

Figure 2-18 The time base calibration of the V1 block, the beam path [24]

- Determination of the probe index

The probe index is the spot whose center of the ultrasonic beam leaves the probe. Its location can be checked by the V1 block. By aligning the probe index on the edge of the cut mark of the block as illustrated in Figure 2-19, the amplitude of the back wall echo should be the maximum.

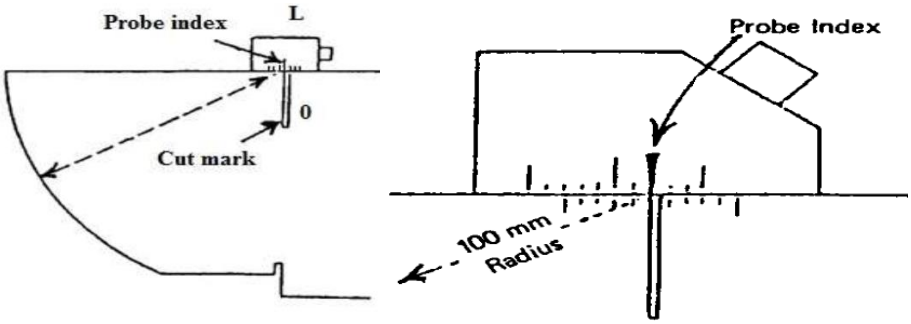

Figure 2-19 The probe positioning for checking its index [14]

- Determination of the probe angle

Angle probes are constructed to produce the ultrasonic beams within an angle range between 30 and 80 degrees. Probe angle can vary upon inspection due to mechanical wear. To determine the exact angle of the probe, the probe is moved at the vicinity of its nominal angle at positions a, b, or c for probes with the angles from 35 to 60, 60 to 75, and 75 to 80 degrees, respectively, to reach the maximum echo from perspex insert or 1.5 mm diameter hole as shown in Figure 2-20. The probe angle is then determined where the probe index meets the angle scale on the block.

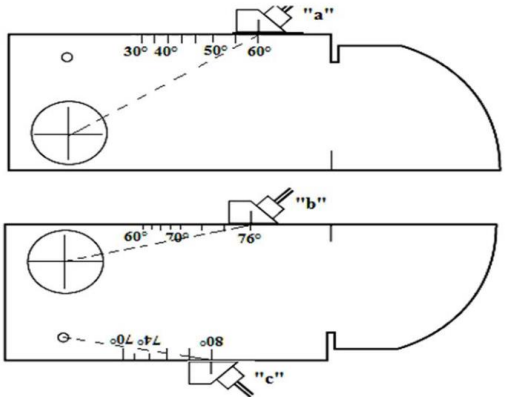

Figure 2-20 The angle of probe determination by using V1 block [14]

2.2.6.3 Defect sizing and evaluation techniques

The ultrasonic testing provides some signal indications on the A-scan display of the ultrasonic flaw detector. It can reveal directly the presence and locations of discontinuities, but there is no evidence on the size and nature of them. Some defects have volume such as gas pores, and others may have planar shapes like cracks. Understanding of the sizes and nature of the defects is of particular interest in integrity evaluation of the structure. This is a controversial subject in ultrasonic testing because no unique technique has been introduced which gives a high degree of accuracy and reliability in defect sizes and characterization in all circumstances. Various techniques have been established in which their concepts are underlying in two basic philosophies. Firstly, these are attempts to deduce the actual size of each defect through the interpretation of defect signal response. These include in the Intensity Drop Technique, Maximum Amplitude Technique, and Time of Flight Diffraction, TOFD. Secondly, these are techniques in which the defect echo is evaluated by comparison of defect the echo from known reflectors responses. These methods do not intend to measure actual defect size. These are the attempts to standardize the defect evaluation methods to achieve a uniformity of the results, and go or no-go criterion. These are Distance-Gain-Size, DGS, and Distance Amplitude Correction, DAC, techniques.

In the DGS method, the defect signal height will be compared with a diagram with the same name as the method to find the equivalent drilled-hole size of the defect. The sensitivity of the defect detector is set by adjusting the actual back wall echo height with the DGS diagram back wall echo at first. Then, the defect echo height is measured by the adjusted gain setting. The intersection of the defect echo and the size curves of the diagram give the equivalent drilled-hole defect size.

However, in the DAC method, the gain will be set by using the reference blocks resulting in the DAC curve for every probe and testing situation. The amplitude of the defect echo will be measured and compared with the level at the constructed DAC curve.

2.3 Finite element method for wave propagation modeling

2.3.1 Dynamic equilibrium equation

Wave propagation can be described by the dynamic equation of motion, because wave propagation is inherently a dynamic problem [16]. The finite element form of a dynamic problem is

$$[M]\{\ddot{d}\} + [C]\{\dot{d}\} + [K]\{d\} = \{F\} \qquad 2\text{-}80$$

where $[M]$, $[C]$ and $[K]$ are the mass, damping, and stiffness matrixes, respectively. $\{\ddot{d}\}$ and $\{\dot{d}\}$ represent nodal accelerations and velocities vector, respectively. Finally, $\{F\}$ is the nodal external

forces vector. Vectors, here, are time-dependent quantities implying that equation 2-80 should be solved numerically in several time steps. There are two different resolution methods, implicit and explicit.

In the implicit method, the next step is obtained by solving the dynamic quantities not only on previously known values but also on unknown values at the next step. Thus, some nonlinear equations are produced due to the inverting of the mass and stiffness matrixes at each time step. It implies that it is unconditionally stable and time increment governs only the accuracy of the analysis. The explicit method, on the other hand, uses only the previously known values to reach the value of the next step. Thus, the time increment plays an important role to have stable solving. However, it does not need to invert the integration operator matrixes, which makes solving at each increment relatively inexpensive [30].

2.3.2 Abaqus explicit solver

For dynamic problems, Abaqus explicit package [30] offers an explicit solver that uses a half-central difference method. In this method, equation 2-80 are integrated by using

$$\dot{d}_{n+\frac{1}{2}} = \dot{d}_{n-\frac{1}{2}} + \frac{\Delta t_{n+1} + \Delta t_n}{2} \ddot{d}_n \qquad 2\text{-}81$$

$$d_{n+1} = d_n + \Delta t_{n+1} \dot{d}_{n+\frac{1}{2}} \qquad 2\text{-}82$$

where d is the displacement and n is the time step varies from zero to the number of time increments. The procedure starts with the calculation of the velocity and acceleration for each degree of freedom from initial values.

The procedure works with a large number of small time increments efficiently. The efficiency key of explicit solving procedure comes from the fact that it uses a diagonal element mass matrices because of lumped mass approximation. Thus, it results in two major benefits. Firstly, the equation for every degree of freedom is solved independently. Secondly, there is no need to calculate the invert of the mass matrix, so the accelerations at the beginning of the increment are obtained simply by

$$\ddot{d}_n = \{M\}^{-1}(\{F\}_n - \{I\}_n) \qquad 2\text{-}83$$

where $\{F\}$ is the external force vector, $\{I\}$ is the internal force vector, and $\{M\}^{-1}$ is the inverted mass matrix which is easily computed from $\{M\}$.

As mentioned before, explicit implementation is conditionally stable. Wave propagation consists of time and space parameters. Both of them are crucial for the stability of analysis. It was shown that the three following conditions should be satisfied by using explicit dynamic solving in wave propagation application.

1. The time increment required for stability in central difference operator is related to the “time” domain in the form of the maximum frequency exists in the system by, [32],

$$\Delta t \leq \Delta t_{cr} = \frac{2}{\omega_{max}} \qquad 2\text{-}84$$

2. The time increment is also related to “space” domain in the form of minimum element size by, [32],

$$\Delta t \leq \Delta t_{cr} = \frac{\Delta L}{c_l} \qquad 2\text{-}85$$

where ΔL is the shortest distance between nodes and sides of the element. It is defined differently among triangular and rectangular elements, see Figure 2-21.

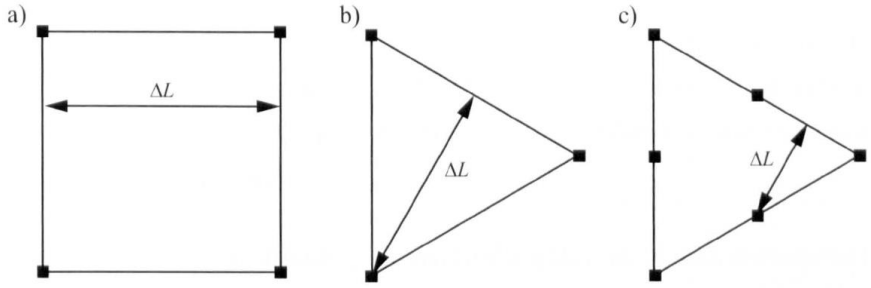

Figure 2-21 Illustration of ΔL in critical time increment [31]
ΔL for critical time increment in explicit solving, a) linear square element, b) linear triangular element, quadratic triangular element.

The time increment of the model can also be expressed as a portion of the critical one. This factor being called *Courant number* is a ratio between the time increment of the model and critical time increment

$$C_n = \frac{\Delta t}{\Delta t_{cr}} \qquad 2\text{-}86$$

The Courant number is a measure showing how close the applied time increment to the critical value is. To ensure a stable analysis, it should be less than one. It is preferable to keep it close to one to achieve appropriate accuracy.

3. The space discretization is also important since the number of elements involving in the wavelength should be enough to reconstruct it appropriately. Thus, ΔL should be

$$\Delta L \leq \frac{\lambda}{N} \qquad 2\text{-}87$$

where N is the number of elements per wavelength. There are different recommendations for N, but it is usually recommended to be a number between 6 and 10 [31], [22]. The higher number element per wavelength provides a higher accuracy at the expense of increased analysis time-consuming.

2.3.3 Non-reflecting boundary

Modeling of wave propagation is done through finite media. Thus, the effect of the edges of the media in terms of reflection is inevitable. Edge reflection is not inherently inappropriate, but its presence and propagation throughout the medium cause interactions with the valuable signals which are the particular objective of the modeling. These generated noise signals, when spurious (i.e. when not physically representative), decreased or even eliminated. For the sake of the noise reduction in modeling, the reflective boundaries can be positioned either further away by increasing the size of the model, or non-reflecting boundaries or absorbing layers can be used. The latter one is of particular interest as it allows the models to run faster. Non-reflecting boundaries can be implemented in commercially available FE packages by defining finite regions with increased damping or using infinite elements.

Absorbing layers are the regions in the model where the energy of the entering waves is dispersed. The method of adding absorbing layers to the model is by assigning a damping coefficient to the elements of the layer. Damping gradually increases from zero at the interface of the area of study to the maximum at the end of the layer. It is preferable to increase damping element by element to avoid a mismatch between the elements and consequently avoid reflection [31].

Abaqus package [30] offers a special type of element known as infinite elements. Below, this is introduced in a one-dimensional problem. A similar approach can be applied to higher-dimensional problems. The damping form is introduced at the boundary of the finite elements by

$$\sigma_{xx} = -\alpha_l \dot{u}_x \tag{2-88}$$

$$\sigma_{xy} = -\alpha_s \dot{u}_y \tag{2-89}$$

This consideration comes from the assumption that there is no wave reflection occurring at the boundaries. Now, consider a wave propagating towards the infinite elements with the following potential function

$$\phi = Ae^{ik_l(x-c_l t)} \quad and \quad H = Be^{ik_s(x-c_s t)} \tag{2-90}$$

By substituting them in equation 2-45, the corresponding displacements are

$$u_x = Aik_l e^{ik_l(x-c_l t)} \tag{2-91}$$

$$u_y = -Bik_s e^{ik_s(x-c_s t)} \tag{2-92}$$

The first derivative of them is the particle velocity

$$\dot{u}_x = -Ak_l{}^2 c_l e^{ik_l(x-c_l t)} \tag{2-93}$$

$$\dot{u}_y = Bk_s{}^2 c_s e^{ik_s(x-c_s t)} \tag{2-94}$$

And, the corresponding stresses are obtained by substituting displacements in equations 2-91 and 2-92 into equations 2-46 and 2-48

$$\sigma_{xx} = (\lambda + 2\mu)Ak_l{}^2 e^{ik_l(x-c_l t)} \tag{2-95}$$

$$\sigma_{xy} = -\mu Bk_s{}^2 e^{ik_s(x-c_s t)} \tag{2-96}$$

Finally, By substituting stress in equations 2-95, 2-96 and particle velocities in equations

2-93, 2-94 into equations 2-88, 2-89, respectively, it gives

$$\alpha_l = \rho c_l \tag{2-97}$$

$$\alpha_s = \rho c_s \tag{2-98}$$

Abaqus calculates and implements these values in the infinite elements. Theoretically, all of the normally impinged plane body waves are absorbed by the infinite elements. However, infinite elements provide a “quiet” boundary rather than complete silence for non-plane body waves. These infinite elements are used in the models of this thesis.

Chapter 3 Finite element modeling of ultrasonic testing

3.1 Model objectives

In total, 4 finite element models are constructed to simulate the checks and acts being done in the ultrasonic calibration procedures. As described in section 2.2.6.1, the calibration processes of an angle probe include time base calibration, probe index determination, and probe angle control. These calibrations and controls will be performed by 4 models described in section 3.2.

The major media of the ultrasonic testing which are an angle probe, a coupling, and a specimen or test piece are simulated in our models. Their geometry, material properties, and interactions are introduced to the software. Therefore, the behavior of them can be investigated.

The main objectives of the models are as follows:

- Model 1

Model 1 is a simulation of a portion of the V1 calibration block shown in Figure 2-16. Two arcs of this block with radii of 100mm and 25mm which is called “specimen or test piece” in this work are selected to simulate the calibration of an angle probe as described in section 2.2.6.2. It is expected to observe the beam path shown in Figure 2-18.

By the results of model 1, the speed of sound in the probe and the specimen will be calculated. The speed of sound is one of the most important parameters showing the performance of the modeling. This will be compared and verified by the analytical values obtained by equation 2-26. Based on the calculated speed of sound, the time-displacement records or “displacement history” will be transferred to the distance-displacement record. The displacement history used for this purpose is extracted from a node located in the middle of the place where the ultrasonic wave generates. This will be explained later in section 3.3.8. By this transformation, the horizontal scale of the A-scan display will be constructed.

The index of the simulated probe will be controlled and investigated. This is done by using the 100mm radius arc of model 1 similar to the procedure described in section 2.2.6.2 and shown in Figure 2-19. It should be noted that the procedure of determination of the probe index in actual calibration is performed by moving the probe around the cut mark of the V1 calibration block to find the highest back wall echo. While the simulation of this procedure is done only in model 1. The reason is that the beam propagation can be observed in the simulation while in the actual testing, this observation is almost impossible. Therefore, the entrance of the ultrasonic beam and its path can be used to control the probe index.

The angle of the simulated probe will be determined by using the results of model 1. Since we can observe the ultrasonic path inside the specimen. The locus of the maximum displacement of each increment creates a line which its angle to the normal of the probe bottom surface is the probe angle. This is unlike the procedure described in section 2.2.6.2 and shown in Figure 2-20. The reason is the ability to observe the ultrasonic beam path in the simulation.

The probe near field zone will be investigated in model 1. The maximum displacement magnitude of each location inside the specimen will be studied to determine the length of the near field.

The pressure distribution along the coupling medium will be investigated. Specifically, the pressure distribution at layers under the probe and above the specimen will be extracted and shown in a figure to study the effect of the coupling layer in the ultrasonic testing.

- Model 2

The concept of creating model 2 is to control the linearity of the horizontal scale of the A-scan display based on the parameters calculated in model 1. The simulated probe and coupling media of model 2 are the same as in model 1. The specimen has two arcs with 75mm and 25mm radii. The only difference between model 1 and model 2 is the radius of the larger arc. All of the modeling parameters in model 2 are the same as model 1. The displacement history of a node in the probe at a similar location of the node used to creat the A-scan display in model 1 will be extracted. The A-scan display of model 2 will be created by using the algorithm used in model 1. It is expected that the back wall echos of model 2 by using the algorithm of model 1, i.e. the speed of sound and other parameters calculated in model 1, will be at the location of 75mm and 100mm.

- Model 3

Model 3 simulates the V2 calibration block shown in Figure 2-17. The main objectives of creating this model are to control the linearity similar to the purpose of model 2 and experimental verification of the amplitude drop between two back wall echoes.

- Model 4

Model 4 simulates a specimen with infinite dimensions. No returning echoes will be expected in this model. The reason for creating this model is to record the displacement history of a silent situation. Consequently, this record will show the noises of the model. The modeling parameters of model 4 is the same as the other three models except for the specimen geometry. Therefore these noises exist in the record of other models. Using the principle of wave superposition, these noises can be subtracted from the records of the other three models.

3.2 Models geometry

The geometry of the models consists of three different media, the probe, the coupling, and the specimen. These media are created and assembled to the models. The properties and geometries of the probe and the coupling are the same in the models to make the results comparable. Different geometry as described in section 3.1 with the same material properties is used in the models.

In this thesis, the simulated probe is an angle probe with a commercial type of MWB60-N4 as shown in Figure 3-1. This is a probe producing a 4 MHz ultrasonic wave at a 60 degrees angle in steel. It generates ultrasonic pulses in the shape of 6 cycles of Hanning window ton burst formulated in equation 2-78 and illustrated in Figure 2-13. The quality of this plus is calculated to 2.77 from equation 2-77 and Figure 2-12. The detailed geometry of the probe is shown in Figure 3-2. The dimensions were

measured from the actual probe. The generated P- waves hits the bottom surface of the probe at 47 degrees from the normal line to the probe bottom surface and reflects in P and S waves at 47 and 22 degrees, respectively, following Snell's law in equation 2-64.

Figure 3-1 MWB60 - N4 ultrasonic probe
The right picture is a top view and the left one is a bottom view of the probe

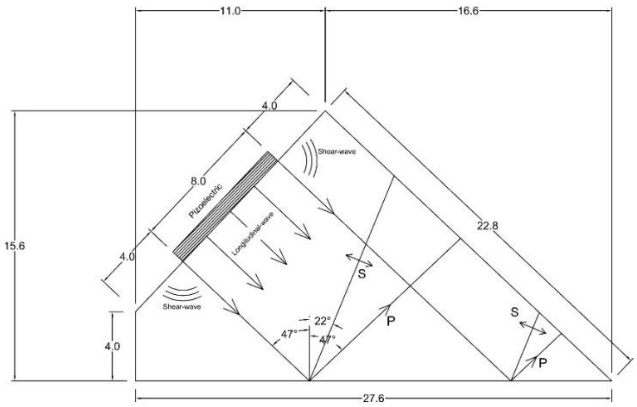

Figure 3-2 Geometry of MWB60 – N4 modeling, units in mm.

The coupling medium is modeled under the probe and covers the whole area under it. The thickness of the coupling is chosen to 0.5 mm. This distance allows us to represent a distinguished pressure distribution at the layers under the probe and the specimen. However, the thickness of the coupling in the actual ultrasonic testing is far less than 0.5mm.

The geometry description of 4 models are as following:

- model 1

The geometry of model 1 is illustrated in Figure 3-3. This model simulates the two quadrants of the V1 calibration block shown in Figure 2-16. In this model, the 100mm quadrant is simulated by a 60 degrees arc with the same radius, and the 25mm quadrant is modeled on the opposite side of the 100mm radius arc with a common center. The distance between two curves creates a straight line used to define the boundary condition for the whole system.

The probe and the coupling are placed on top of the specimen in model 1. As mentioned above, the probe produces an ultrasonic wave in 60 degrees normal the probe bottom line. The line indicated in the specimen in Figure 3-3 shows the beam path at 60 degrees, 30 degrees from the horizontal line, which is called the "beam center axis" for the rest of the thesis.

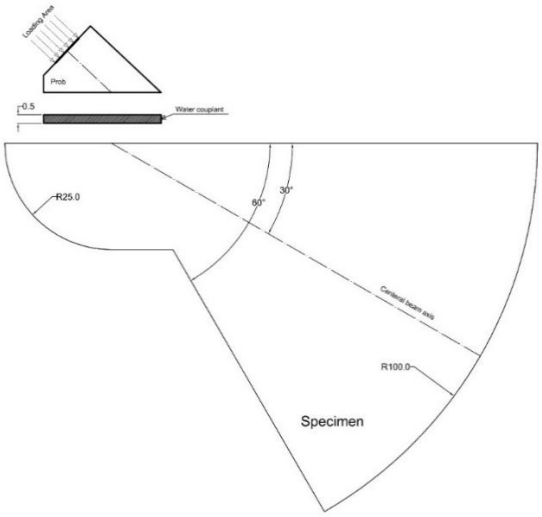

Figure 3-3 Geometry of model 1, units in mm.
The geometry of the 100 mm radius specimen model of the V1 calibration block

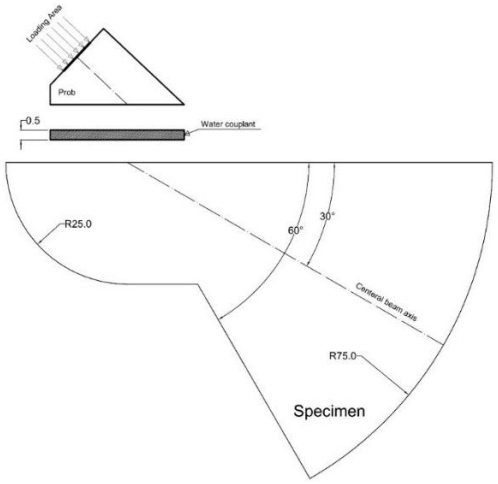

Figure 3-4 Geometry of model 2, units in mm.
The geometry of the 75 mm radius specimen model

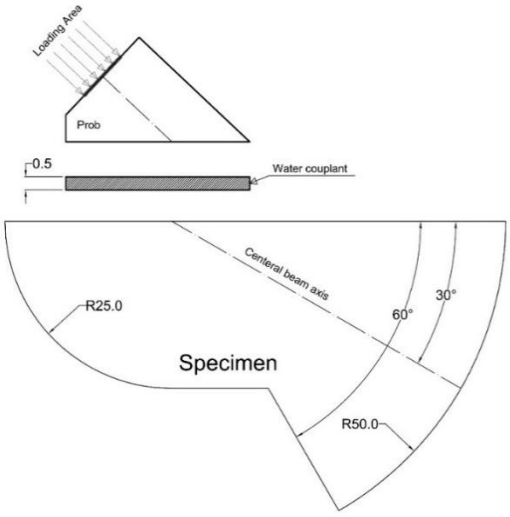

Figure 3-5 Geometry of model 3, units in mm.
The geometry of the 50 mm radius specimen model

- Model 2

Model 2 is the same geometry as model 1 with a difference in the longer radius arc. This radius is set to 75mm as illustrated in Figure 3-4. The other geometry and properties of model 2 are copied from model 1.

- Model 3

Model 3 simulates the V2 calibration block which is shown in Figure 2-17. Figure 3-5 represents the geometry of mode 3. The shape of this calibration block is manipulated by keeping the main features of it. Two arcs of it are modeled in model 3 which have the radii of 25mm and 50mm. The same as the two other models, a straight face is created for introducing the boundary condition. The probe and coupling and other modeling parameters are copied from model 1 to have the ability to compare the results.

- Model 4

Model 4 is a copy of model 1 by changing the geometry of the specimen to a 150 x 200 mm block as illustrated in Figure 3-6. This model has the same configuration as other models. The probe is placed in the middle of the block. It is expected that no reflection from the specimen will come back and detected by the probe.

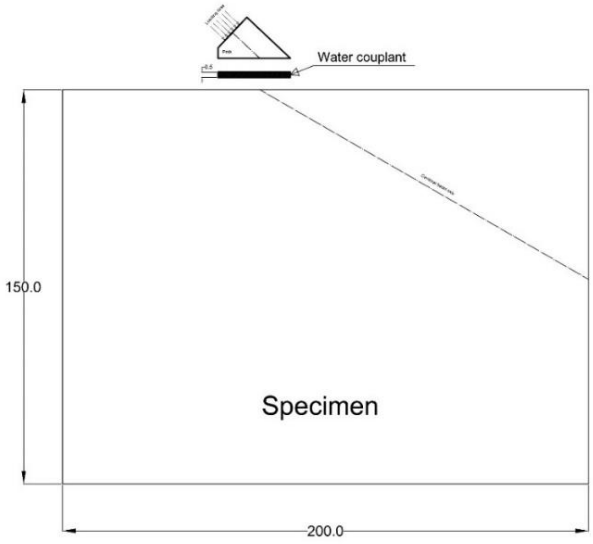

Figure 3-6 Geometry of model 4, units in mm.

3.3 Modeling procedure

The details of the modeling procedure are presented in this section. Abaqus ACE/explicit [30] is employed as a modeling platform.

3.3.1 Material properties

Three different media including perspex glass for probe edge, water coupling, and steel specimen are used in the models. Table 3-1 shows the property of materials used in the models. The speeds of sound are calculated from the given density, modulus of elasticity, and Poisson ratio by using equations 2-26. These theoretical velocities will then be compared with the measured data from our models.

Table 3-1 Material properties of the models and theoretical velocities

Part	Prob	Couplant	Specimen
Material	Perspex	Water	Steel
Density (kg/m^3)	1180	1000	7850
Modulus of elastisity (GPa)	6.33	-	212
Bulk modulus (GPa)		2.1	
Poisson ratio	0.311	-	0.2842
Vp (m/s)	2730	1500	5920
Vs (m/s)	1430	-	3250

3.3.2 Loading

The pressure applied to generate the ultrasonic wave as shown in Figure 3-7 is a 6 cycle of Hanning window tone burst with the central frequency of 4 MHz. The loading pulse is generated by equation 2-78 representing the ultrasonic pulse generated by the MWB60-N4 probe. The quality number is also calculated by using equation 2-77 at a value of 2.77 from the spectrum diagram shown in Figure 2-12.

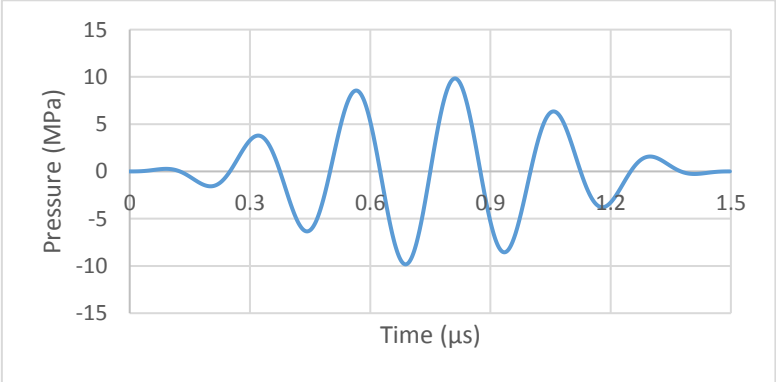

Figure 3-7 Hanning window tone burst pressure with 4 MHz central frequency

3.3.3 Meshing and element type

Meshing and element types are two important parameters governing the accuracy and the stability of a finite element dynamic analysis. As seen in section 2.3.2, referring to equations 2-84 and 2-85, the stable time increment depends on the frequency of the wave and element size. The probe and the coupling were meshed for model 1 and copied this to the other 4 models. However, the specimen meshing differed in every model depending on the geometry. The maximum element size was calculated from equation 2-87 using N=10. These calculations are representing in Table 3-2.

Table 3-2 Maximum element size and stable increment calculations

		Probe	Coupling	Specimen
$f_c\ (MHz)$		4		
$c_l\ (m/s)$		2730	1000	
$c_s\ (m/s)$				3250
$\lambda\ (m)$		682.5	250	812.5
N		10	5	10
$\Delta L_{max}\ (\mu m)$		68.25	50	81.25
$\Delta L_{used}\ (\mu m)$		50	50	80
$\Delta t_{max}\ (\mu s)$	Eq. 2-85	0.018	0.050	0.025
	Eq. 2-84	0.080		

The elements selected for these models are in the type of plane stain since the modeling is of a section of the 3D phenomenon in 2D. The element types are assigned from the Abaqus element library [30] which are CPE3 for triangular 3 nodes elements and CPE4R for rectangular 4 nodes elements where the geometry of the meshing part is appropriate. Moreover, an infinite or one-way element named CINPE4 is also added to the model to create a non-reflecting boundary as described in section 2.3.3. There are no other kinds of damping or energy absorptions defined to the elements, so no energy dispersion is expected.

3.3.4 Probe modeling

The probe is modeled by the dimensions shown in Figure 3-2. As illustrated in Figure 3-8, the infinite elements are added to the two boundaries of the probe representing the damping blocks shown in Figure 2-10 to absorb the reflected waves. The pressure gradient is also applied to the loading area at the width of 8mm. The bottom surface of the probe is the location where waves are transmitted to the specimen.

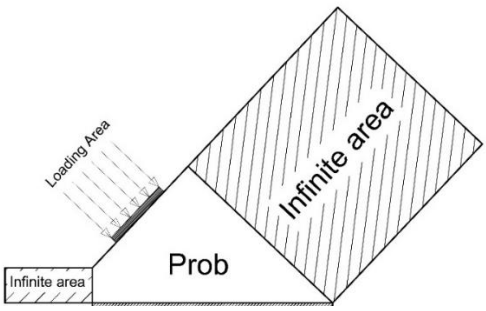

Figure 3-8 The configuration of the probe in the models

3.3.5 Coupling modeling

Water as the coupling medium is modeled in this work. A 0.5mm layer of water coupling has been modeled between the probe and specimen. A 3 node linear 2D acoustic triangular element, AC2D3, are used in the coupling area. The coupling medium is completely covering the area under the probe surface so complete wave transmission is ensured.

3.3.6 Specimen modeling

The models are of steel specimens in which, the shear wave propagate. Different geometries of the models were introduced in section 3.2. Each specimen is divided into several partitions to mesh different parts separately. A combination of CPE4R and CPE3 is used as element type where appropriated.

3.3.7 Model assembly

Three different media are assembled as shown in Figure 3-9. The interaction between them is a type of tie interaction where the displacement of the joined nodes is considered to be equal. It is also a non-reflecting feature assigned to the two free sides of the coupling medium to create a silent boundary at those boundaries.

Three local Cartesian coordinates are defined to models. CSYS-1 is a general horizontal and vertical coordinate, CSYS-2 is defined in a way that the X-axis along the probe center line to extract the displacement. Similarly, CSYS-3 is defined to extract the displacement along the beam central axis.

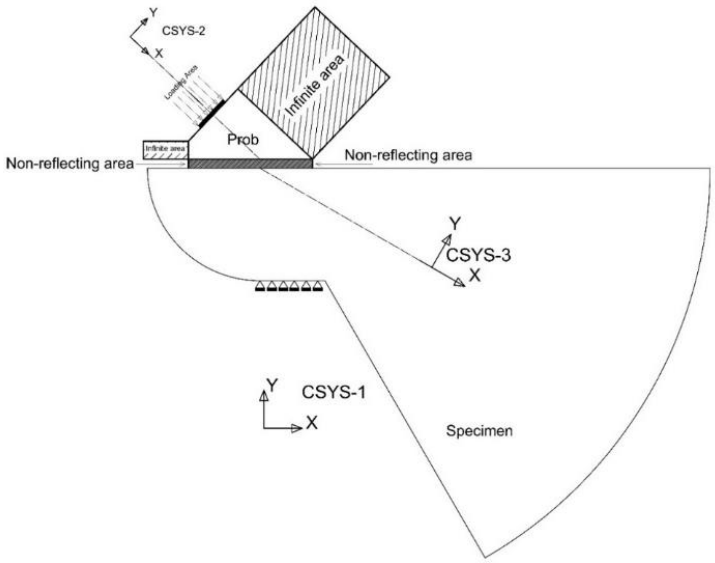

Figure 3-9 The model assembly
Local axis, Boundary conditions, non-reflecting area, and assembly configuration of the models are shown in this picture.

Finally, A fixed boundary condition is assigned to the bottom surface of the specimen at the straight surface between the two arcs as shown in Figure 3-9.

3.3.8 Displacement recording nodes

The nodal displacements are recorded at several points at the probe and specimen. Figure 3-10 shows these nodes and their locations at the probe. The local displacement in X-direction which is defined as U1 will be recorded at node number 1 for all models at the SCYC-3 local coordinate to study the echo of any reflector inside the specimen. The U1 displacement in SCYC-3 local coordinate of nodes number 2 and 3 will be extracted to calculate the speed of sound in the probe in model 1.

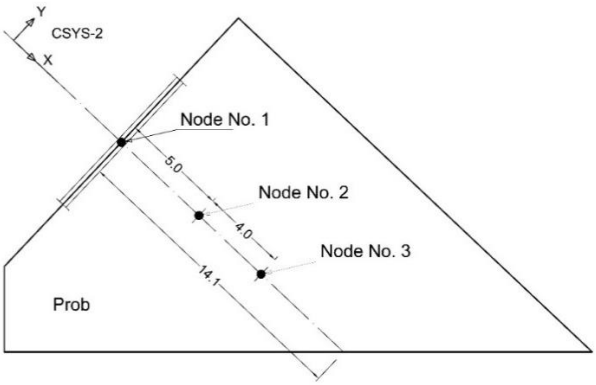

Figure 3-10 Displacement recording nodes in probe

There are three nodes selected to calculate the speed of sound in the specimen of model 1. Figure 3-11 shows their locations and distances on the beam centerline. The U1 displacement in CSYS-3 local displacements will be extracted and studied.

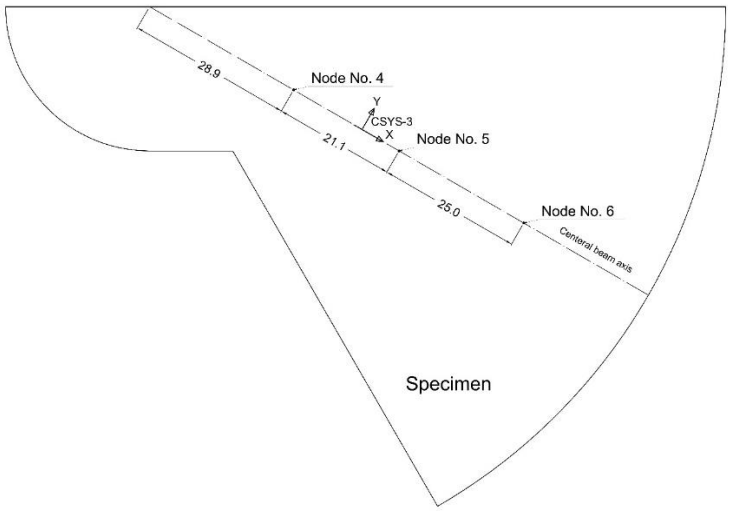

Figure 3-11 Displacement recording nodes in specimen

3.4 Simulation results

The results of the simulation of the models described in chapter 3 are presented as contour plots over the model geometry and graphics. The displacement vector fields and displacement magnitude are extracted in the various local coordinate systems. The displacement magnitude is calculated by the following equation

$$Displacement\ magnitude = \sqrt{(U_1)^2 + (U_2)^2} \qquad 3\text{-}1$$

where U1 and U2 are the amplitude of displacements in X and Y directions, respectively. The displacement magnitude is the length of the resultant displacement vector which is independent of the coordinate. Also, U1 and U2 displacement will be extracted in the local coordinates.

The displacement field has been chosen to study the wave propagation. As presented in Section 2.1.3, displacements directly relate to acoustic pressure and intensity, both of which scale with the voltage measured in the piezoelectric crystal. Both P and S waves are thus characterized in terms of displacement magnitudes along the appropriate local coordinate system. The displacement is

recorded in one specific direction where the displacement in only one direction needed. For instance, the voltage created in the piezoelectric crystal from the echo wave depends on the direction of it which is perpendicular to the crystal plane.

3.5 Probe

The snapshots of the propagating wave in different time sequences are shown in Figure 3-12, Figure 3-13, and Figure 3-14.

Figure 3-12 shows the displacement magnitude plot of the wave inside the probe area at time 3.25 µs after pressure impulse (cf. Figure 3-7 where the pressure pulse starts at time zero). A plane P-wave is generated from the pressure loading area and propagates along the probe centerline. Concomitantly, S-waves and surface waves generated at both edges of the loading area and propagate at a lower speed of the P-wave.

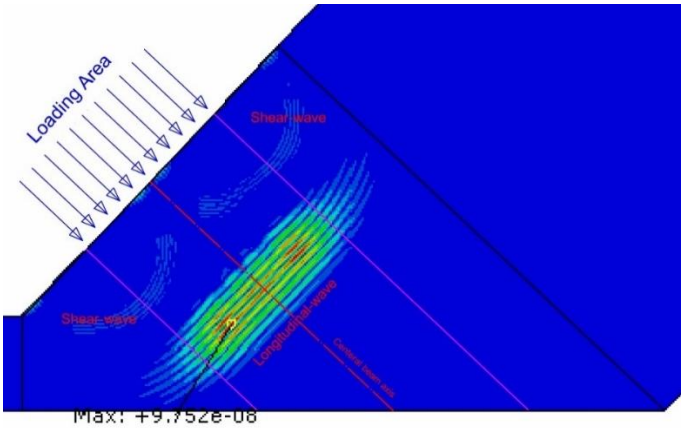

Figure 3-12 Probe visualization at initial wave propagate

In Figure 3-13, the reflections of the initial wave at the boundary of the probe medium are visible. The P-wave is reflected as one P-wave and converted into an additional S-wave as discerned in section 2.1.4.2 and Figure 2-5. As can be expected from Snell's law, the 47 degrees incident wave reflects in P and S waves at angles of 47 and 22 degrees, respectively.

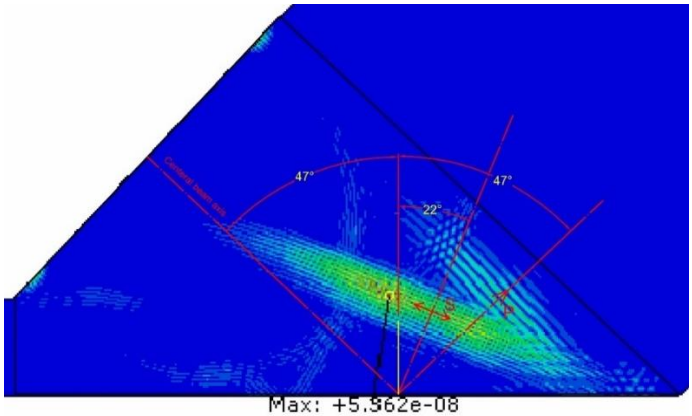

Figure 3-13 Probe visualization at the reflection of the initial wave to it.
Mode change of a P-wave initial wave to P and S waves at the 47 and 22 degrees

The transmitted wave from the specimen comes back into the probe after reflected by the reflector inside the test piece as shown in Figure 3-14. The back-reflected wave is constituted of a P-wave and S-wave wave as shown in Figure 2-7. The P-wave is propagating normal to the loading area.

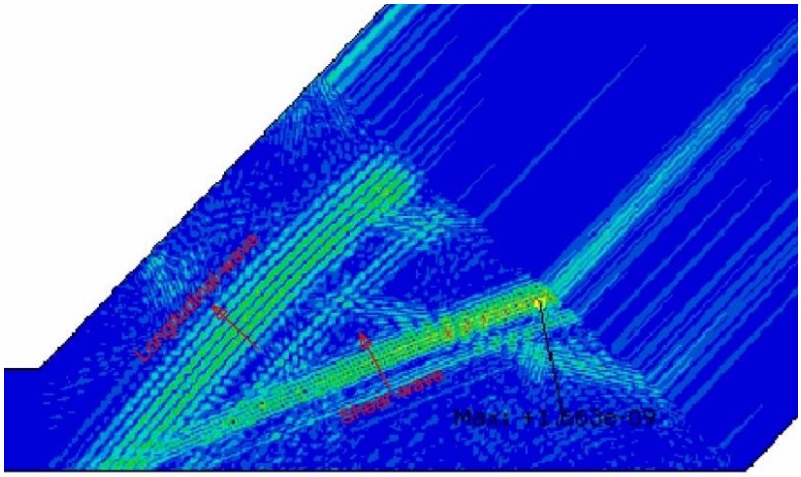

Figure 3-14 Transmitted echo from a reflector into the probe area
The transmitted waves reflected from a reflector into the probe area divides into P and S waves inside the probe area.

The model is designed to generate a P-wave in the probe. In the P-wave, the particle displacement is in the direction of propagation. Thus, no transverse movement will occur in the P-wave. To prove that, the longitudinal and transverse displacements, U1 and U2, measured in the CSYS-2 local coordinate are represented in Figure 3-15 at the same instant in time of propagation.

It can be observed that the S-waves which are produced at both sides of the loading area are also visible in the U2 displacement counter plot. Their speed is less than that of the P-wave, so they are propagating with a delay in time.

Figure 3-15 The displacement field of the generated wave shown in CSYS-2 local coordinate
U1 and U2 displacement field in the right and left view at the same time, respectively.

Similarly, when an echo returns to the probe, both P and S waves are transmitted. To recognize them, CSYS-2 local displacement counter plots are extracted and represented in Figure 3-16 at the same time. The P-wave traveling perpendicularly to the loading area is visible in the U1 displacement contour plot, while only the S-wave is visible in the U2 displacement counter plot.

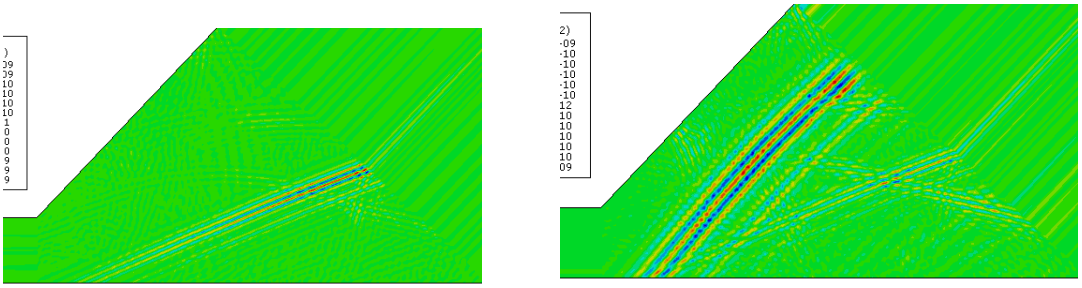

Figure 3-16 The displacement field of the reflected echo from a reflector shown in the CSYS-2 local coordinate.
U1 and U2 displacement field in the right and left view at the same time, respectively.

3.6 Coupling

The acoustic pressure field can directly be extracted in the coupling medium since acoustic finite elements are used to model the coupling medium. This is plotted in Figure 3-17 at different snapshots of wave propagation. The initial transmission of waves from the probe happens from the left side of the coupling medium as illustrated in Figure 3-17a. Waves propagate towards the bottom surface where they are reflected and transmitted to the steel medium as shown in Figure 3-17 b. While the waves are transmitting continuously into the coupling, their interaction with reflected waves from the steel surface intensifies the acoustic pressure. This magnification continues just before the probe index and consequently, a focused wave is transmitted to the steel medium before the point of the probe index, Figure 3-17 c. A rough estimation of this point is 1.4 mm offset from the probe index. The interacted waves propagate towards the right side of the coupling after transmitting most of the energy and are finally absorbed in the non-reflecting boundary condition defined at the right side of the coupling medium, Figure 3-17 d.

The maximum acoustic pressure distribution along the coupling is also extracted at the top and bottom layer and drawn in Figure 3-18. The acoustic pressure at the bottom layer in contact with the steel medium is higher than that at the top layer. The horizontal scale is normalized by the bottom surface length of the probe and the zero point is the location of the probe index. The highest acoustic pressure occurs at the -0.05 normalized distance from the probe index in the bottom layer near the steel medium. This can be obtained from Figure 3-17 c where the maximum acoustic pressure occurs at 1.4mm before the probe index, taking into account that the probe bottom length is 27.6mm shown in Figure 3-2.

A second pressure maximum occurs at 0.08 normalized distance. In the distance between the two maxima, the acoustic pressure drops and rises, and the local minimum occurs at the probe index. It gradually drops with increased distance beyond the second maximum point. The interpretation of this pattern will be explained in chapter 6.

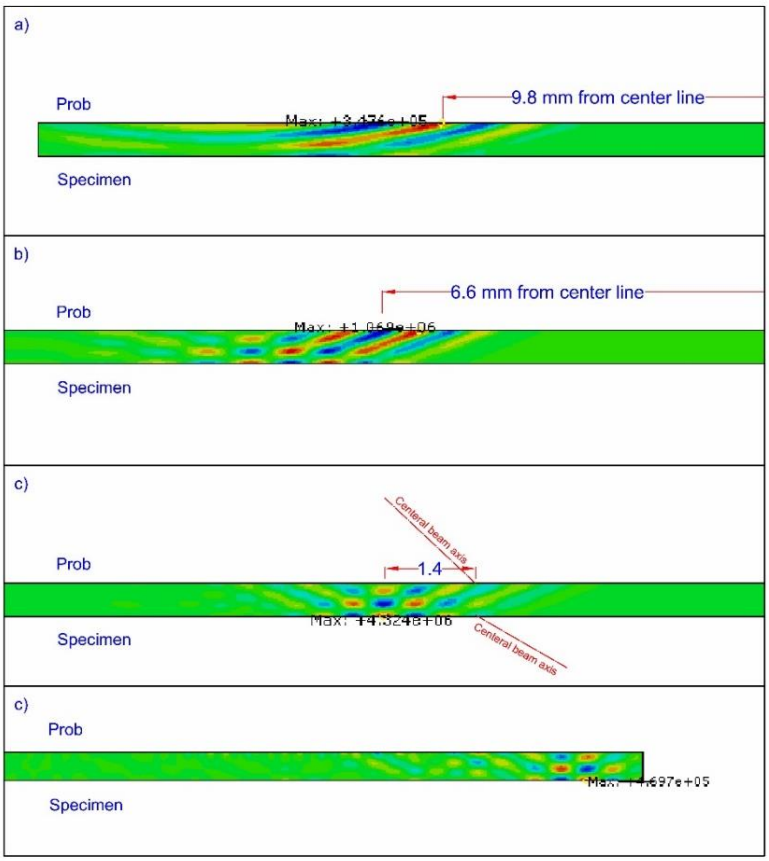

Figure 3-17 Acoustic pressure inside the coupling medium, units in mm.

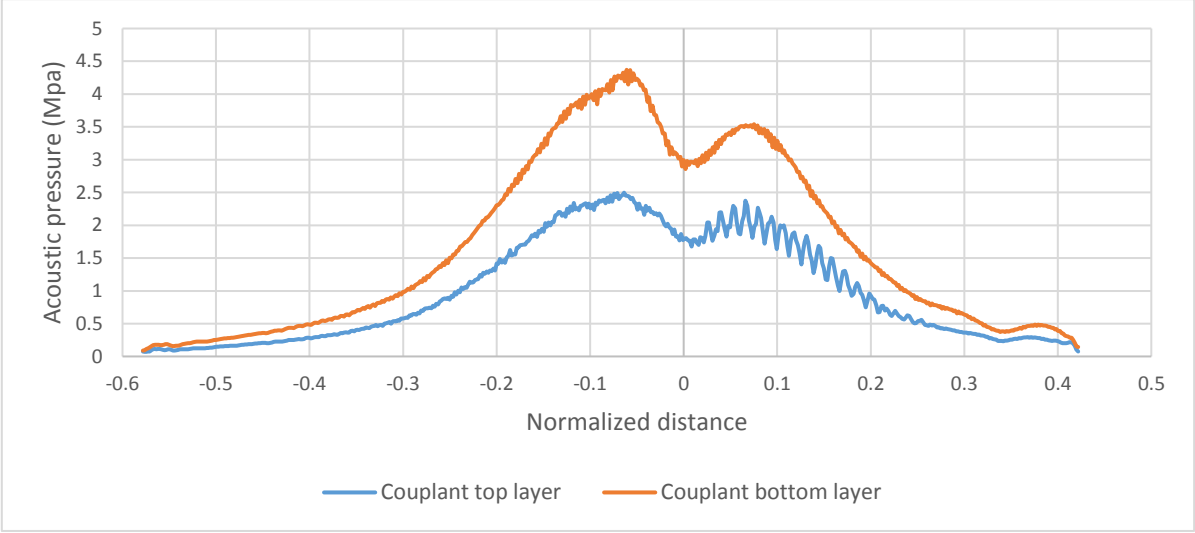

Figure 3-18 Maximum acoustic pressure distribution along the coupling medium at top and bottom layers.

3.7 Specimen

The displacement magnitude contour plots in the Specimen are represented in Figure 3-19 and Figure 3-20 at different times. Transmission of the wave into the steel medium is initiated far from the probe index. The contour plot of Figure 3-19a shows that it begins at almost 8mm offset from the probe index. This is the result of the entrance of the wave into the coupling medium obliquely as shown in Figure 3-12 and Figure 3-17a. The maximum displacement moves towards the probe index near the

surface of the steel medium as the amplitude increases. This is because of a concentration of acoustic pressure just behind the probe index as shown in Figure 3-17 c. The maximum displacement detaches from the surface of the specimen and propagates inside the specimen a few millimeters behind the probe index. This explains the acoustic pressure drop up to the probe index in Figure 3-18 as shown in Figure 3-19 b. It does not meet the probe centerline up to 4.8mm from the probe index, Figure 3-19 c.

A plane wave forms where the maximum displacement meets the centerline and propagates towards the 100mm radius curve. Figure 3-20 a, b, and c shows the snapshots of it. Figure 3-20 c reveals a 2 degrees deviation from the 60 degrees probe angle. The wave reflects from the curve along the center line and propagates towards the probe index point as illustrated in Figure 3-20 d, e, and f. After transmitting a portion of its energy to the probe, the rest reflects at the same angle to the 25mm radius curve, Figure 3-20 g, h, and i. This refection is also transmitted and reflected towards the 100mm radius. The same pattern as the initial wave entering the specimen happens as clearly visible in Figure 3-20 j, k, l. However, the beam angle deviation increases to 5 degrees by which the beam angle reaches approximately 55 degrees. The reason can be because of the initial 2 degrees deviation and the refraction due to the breaking point where the straight line between two arcs breaks to the larger radius arc. Besides, the wave spread is more than that of the initial wave.

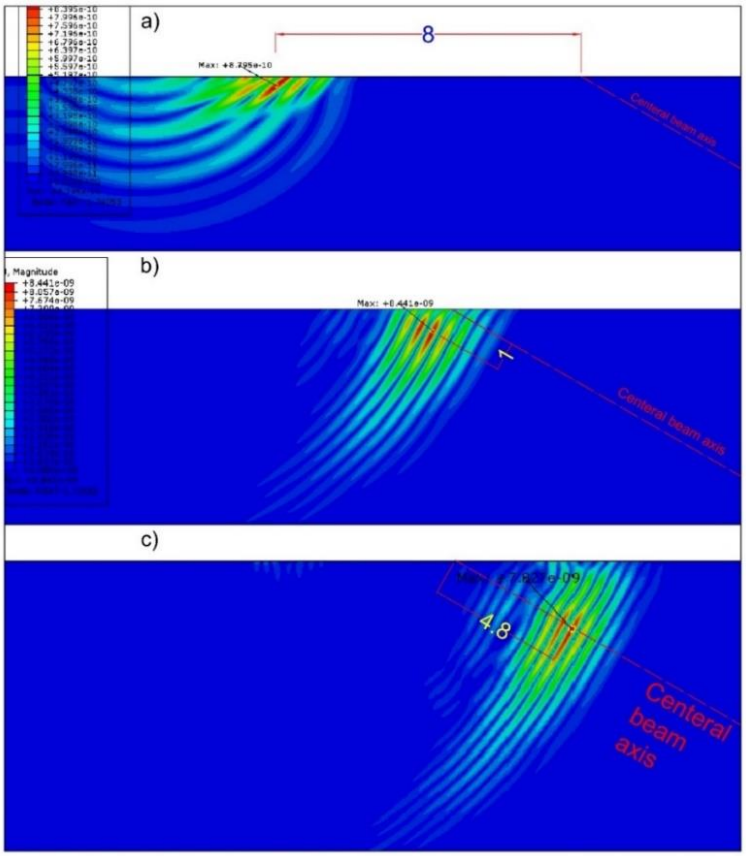

Figure 3-19 Displacement magnitude of the transmitted wave in the specimen, units in mm.
A closer view of the transmitted wave near the probe index.

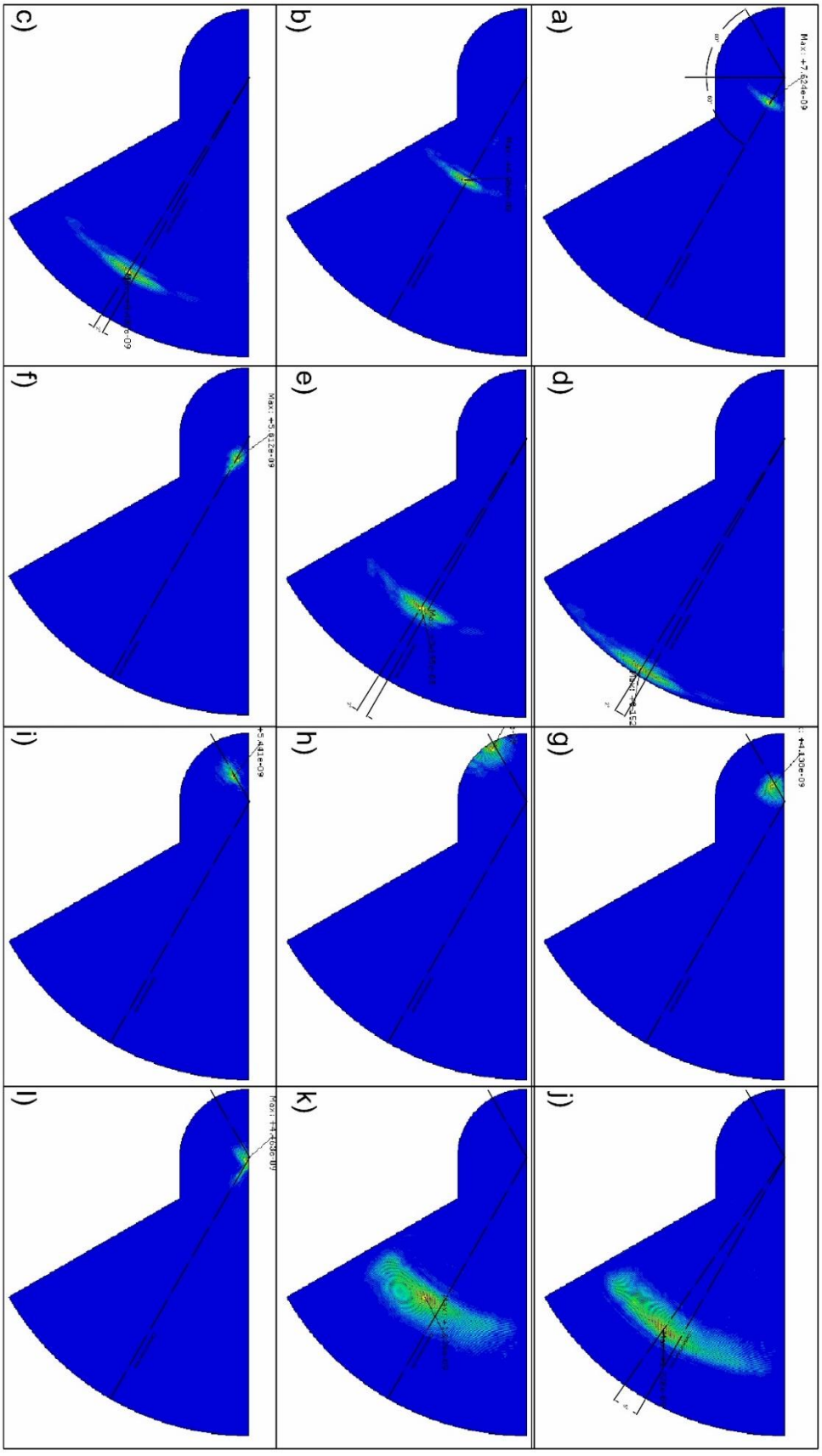

Figure 3-20 Displacement magnitude of the transmitted wave in the specimen.

To evidence the creation of S-wave inside the specimen, U1 and U2 displacement contour plot is extracted along the CSYS-3 local coordinate. The x-direction of this coordinate lays on the beam nominal centerline which is 60 degrees. The U1 displacement contour plot does not show any particular disturbance on the centerline, while a clear transverse wave is recognizable in the U2 displacement contour plot. Thus, a mode change has occurred during the transmission of the P-wave from the probe into S-wave inside the specimen.

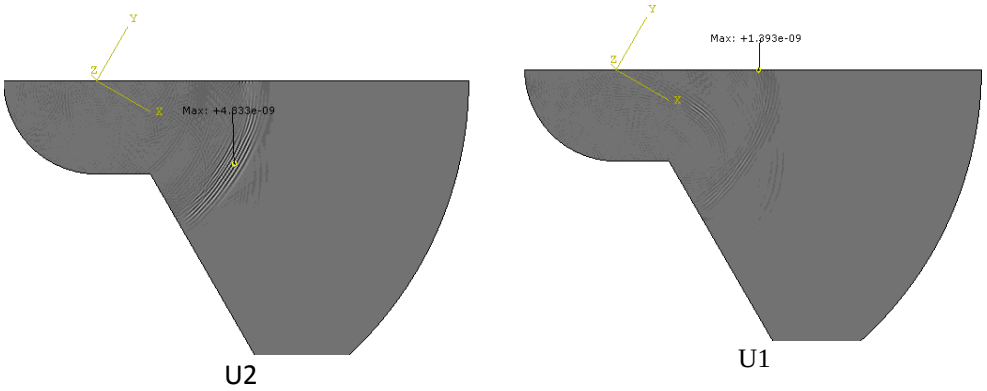

Figure 3-21 The displacement field of the transmitted wave in the specimen shown in the CSYS-3 local coordinate.
U1 and U2 displacement field in the right and left view at the same time, respectively.

3.8 Data Analysis

3.8.1 Near field determination

Figure 3-22 shows plots of the maximum values of the displacement magnitudes along the beam centerline, 60 degrees, and 2 degrees deviation, 58 degrees. This proves the observation of the beam centerline in Figure 3-20 about the probe angle.

Moreover, Figure 3-22 shows that both curves begin at zero which is the probe index point, and the displacements along the 2 degrees deviation from the beam centerline slightly increase more than that of for the beam centerline. This proves the observation in Figure 3-20 showing that the probe index point is at the location we expected.

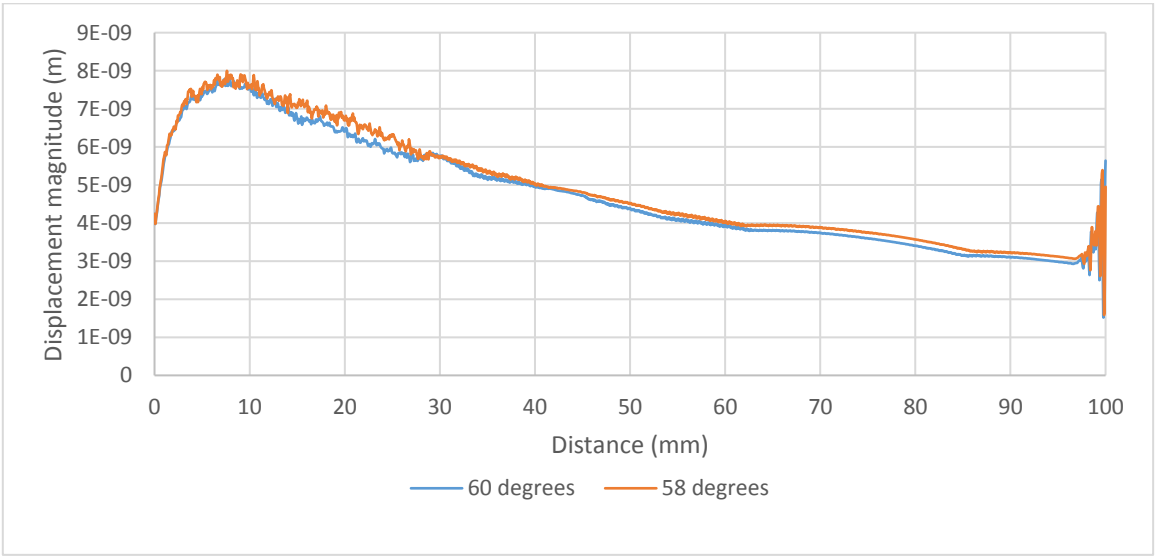

Figure 3-22 The variation of displacement magnitude along the 60 and 58 degrees

Figure 3-22 also shows that the displacement magnitude increases rapidly by the distance from the probe index until reaching an overall maximum displacement value at 7.6mm from the probe index. The displacement magnitude, then, gradually decreases at the end of the medium. Displacement magnitude fluctuations are observed from the maximum value up to 29mm from the probe index while the displacement decreases smoothly at the rest of the curve. If the near field is defined as the distance from the probe index to the point where the maximum pressure or displacement occurs, it will be 7.9mm. However, the concept of near field is a distance where the interaction between the waves entering the medium is causing amplitude fluctuations. Thus, 29mm can be also considered as near field distance. This will be discussed further in Chapter 5.

3.8.2 Displacement radiation field

To study the displacement amplitude variation in the model media, the displacement radiation fields for the probe and specimen are extracted. They show the maximum displacement magnitude calculated at each time increment.

Figure 3-23 shows the displacement radiation field of the probe. The loading area has the highest displacement value. Two displacement concentration spots at both ends of the loading area are visible explaining the creation of the S-waves seen in Figure 3-12. It is clear that the displacement variation along the loading area is not uniform even though we applied a uniform pressure. The waves with large displacements created at the edges of the loading area propagate to the end of the probe medium where the beam enters the coupling medium creating a reversed U shape displacement variation near the coupling. This U shape pattern which is highlighted by a spline in Figure 3-23 shows the variation of the displacement magnitude in the probe medium near the surface of the coupling. This is an explanation of the creation of two maxima in the acoustic pressure distribution shown in Figure 3-18.

A trace of the surface waves which is mentioned in section 3.5 is also visible at two sides of the loading area near the edge of the probe medium in Figure 3-23. These waves have small displacement magnitude which is shown by the dark blue color in this figure.

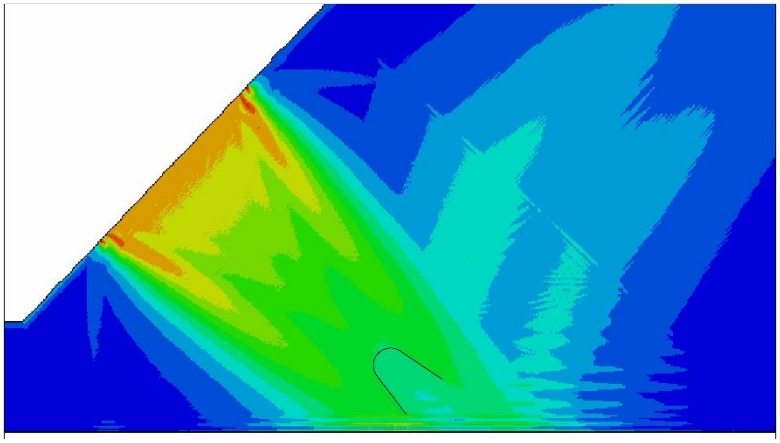

Figure 3-23 Radiation field of the probe
The U shape pattern near the coupling medium is drowned by a spline

The displacement radiation field in the specimen is shown in Figure 3-24. The wave propagation starts at the probe bottom surface. The displacement is the highest at the top surface of the specimen near the probe index. The wave is propagating at almost 60 degrees through the steel medium. The displacement drops gradually with distance. This pattern is similar to the pattern seen in Figure 3-22.

The wave is mostly focused on the area near the beam centerline. The displacement magnitude in this area is dramatically higher than its upper or lower adjacent.

Figure 3-25 provides a closer view of the specimen radiation field. The narrow red line is the beam centerline. Most of the high displacement area is below the centerline as explained in section 3.7.

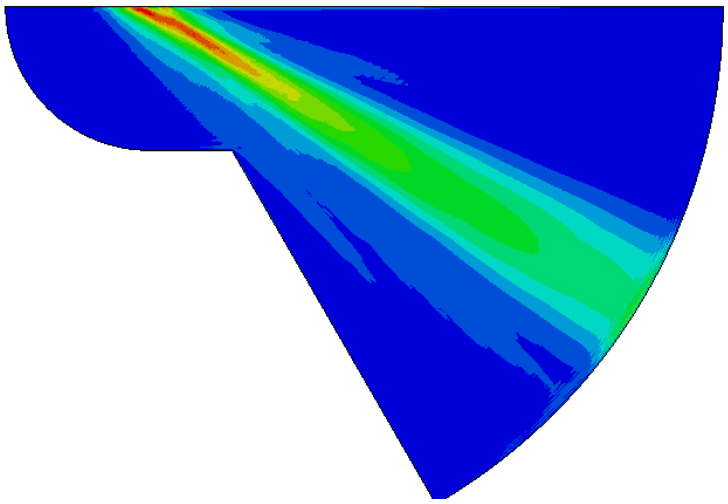

Figure 3-24 Radiation field of the specimen

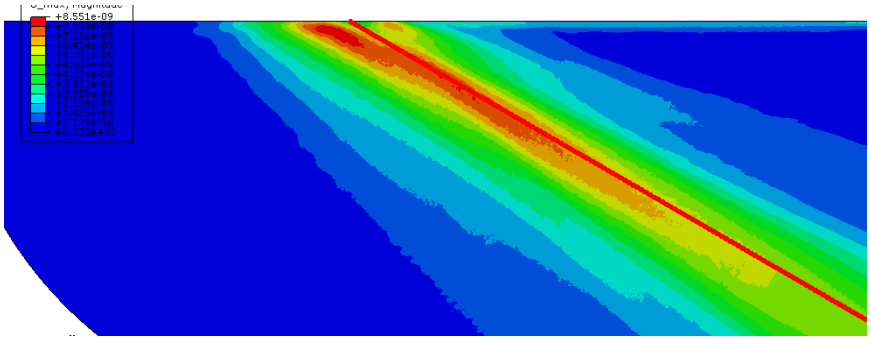

Figure 3-25 A closer view of the radiation field of the specimen at the area under the probe. The redline is 60 degrees beam centerline stretching from the probe index.

3.8.3 Local displacement at node 1 of the probe

The displacements of the node 1 for the models have been recorded to study the echo from the back walls. The local coordinate defined as CSYS-2 shown in Figure 3-10 is used to record the displacement in the x-direction. They are represented in Figure 3-26, Figure 3-27, and Figure 3-28 for models 1, 2, and 3, respectively. For all of the models, some high displacement amplitudes are observed which are continues up to 20 µs of the records. They are damped by the infinite elements mounted at the edges of the probe medium in the models. The large spike in the graphs starting from time zero is the main pulse generated by the pressure field applied to the loading area. The wave will propagate throughout the media and reflects to its initial point at the probe in node 1. The rest of the indications in the graphs up to 20 µs are mainly coming from the surface waves generated at the both of the edges of the loading area, traveling like a surface wave at the edge of the probe medium where the load is applied. This is explained in section 3.5 where the shear waves generated at the edges of the loading propagating like two semicircular shapes inside the probe. The trace of the surface loads is also visible in Figure 3-23 as explained in section 3.5. These are noise signals which are unwanted and not possible to avoid, generated because of modeling situation.

In the displacement histories, two back wall echo indications are visible. As described in section 3.7, the first indication is the back wall echo of the larger radius and the second one is from the 25mm radius. Those indications are recorded at around 76 µs and 155 µs for model 1 which are the reflections of 100mm and 25mm radii, respectively. For model 2, Those are 59 µs and 123 µs for 75mm and 25mm radii, respectively. Finally, the back wall echoes for model 3 are recorded in 44 µs and 91 µs for 50 mm and 25 mm radii, respectively.

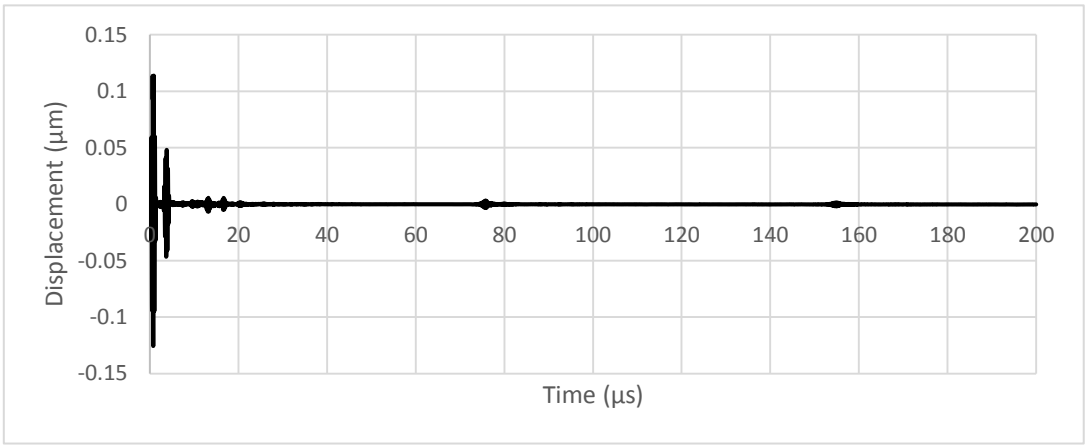

Figure 3-26 The displacement history of node 1 in model 1 recorded in the x-direction of CSYS-2 local coordinate

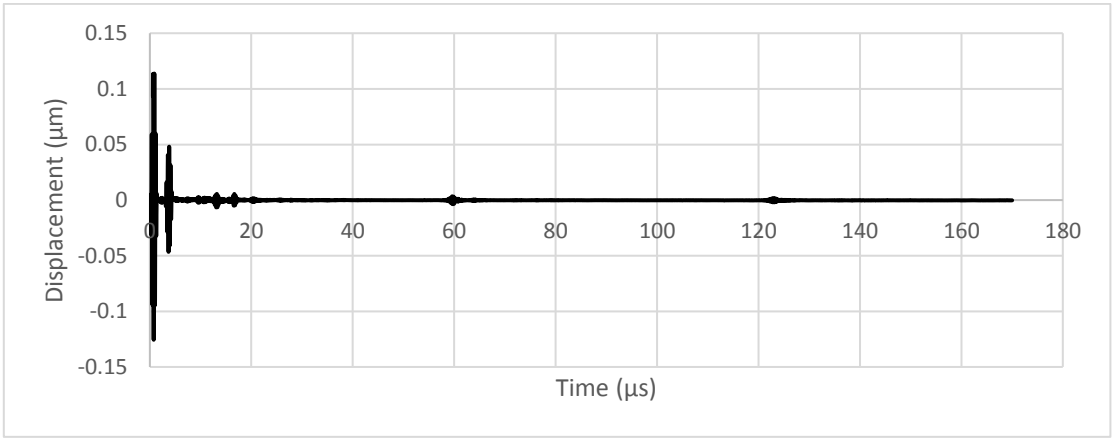

Figure 3-27 The displacement history of node 1 in model 2 recorded in the x-direction of CSYS-2 local coordinate

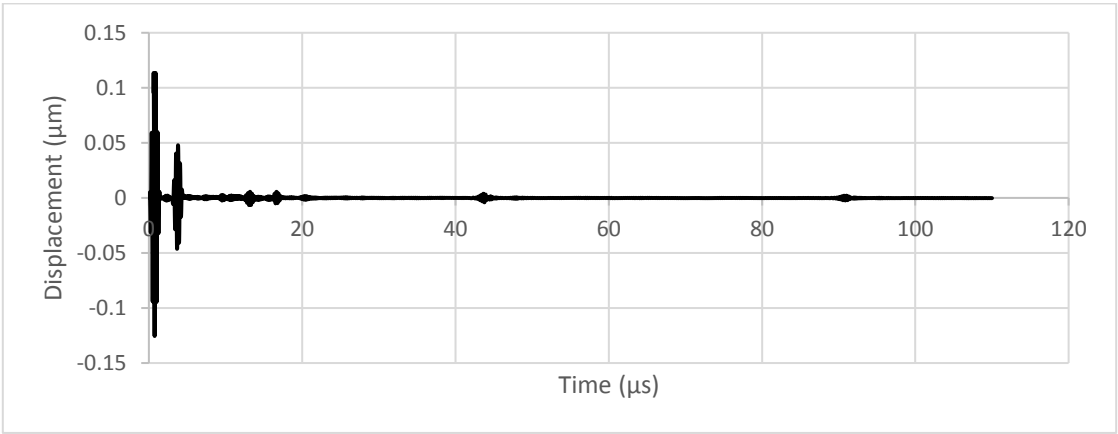

Figure 3-28 The displacement history of node 1 in model 3 recorded in the x-direction of CSYS-2 local coordinate

3.8.4 Noise reduction

As described above, the first 20 µs indications of the displacement histories in Figure 3-26, Figure 3-27, and Figure 3-28 are the noises generated in the model. They are different from the noise signals that exist at the ultrasonic testing described in section 2.2.5. To remove these simulation resultant noise signals, Model 4 is defined, and the displacement at the same node and coordinate as the other modes is extracted.

The displacement history in node 1 for model 4 is shown in Figure 3-29. At a short glance, the first 20µs is the same as the displacement histories of the other models. Thus, simulation resultant noise signals can be removed by subtracting the displacement history of model 4 from the displacement histories of the main models.

Equation 2-79 can be rewritten in the form of

$$s_i(t) = x_i(t) - n(t) \ , i = 1,2, and\ 3 \qquad 3\text{-}2$$

where $s_i(t)$ and $x_i(t)$ are the filtered and unfiltered displacement histories, respectively, for models 1, 2, and 3. $n(t)$ is the displacement history of model 4. By using equation 3-2, the simulation resultant noise signals will be removed. This procedure will be implemented by a Matlab code and results will be represented in section 3.8.6.

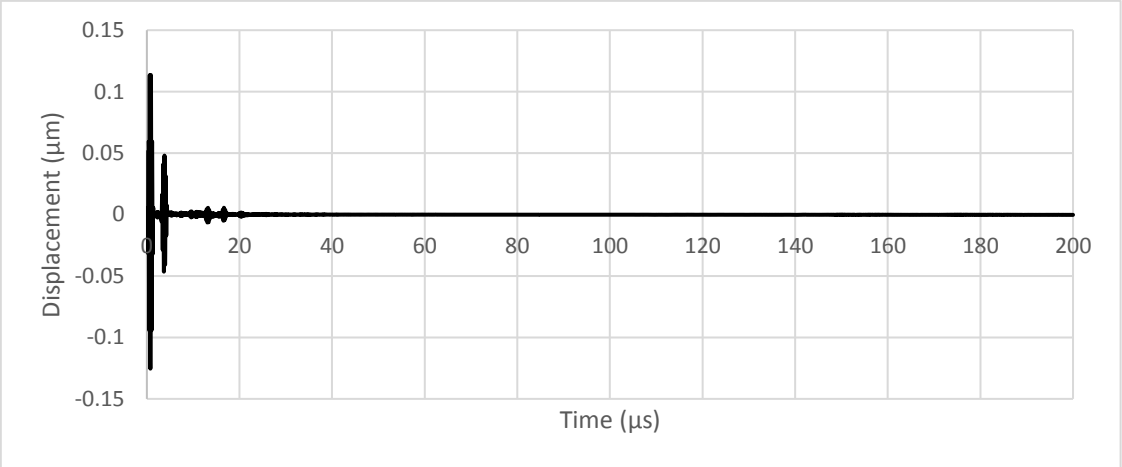

Figure 3-29 The displacement history of node 1 in model 4 recorded in the x-direction of CSYS-2 local coordinate

3.8.5 Speed of sound calculations

The speeds of the sound will be calculated in both probe and specimen media and verified against the theoretical values. The speed of sound is necessary later to transform the displacement history to the A-scan display which is the normal way to represent an ultrasonic signal upon an inspection situation. The speed of P and S waves will be calculated for the probe and the specimen for model 1.

The displacement history of nodes 1, 2, and 3 defined in Figure 3-10 are plotted in Figure 3-30. The main ultrasonic wave which is generated from the probe and propagating inside it is selected to study.

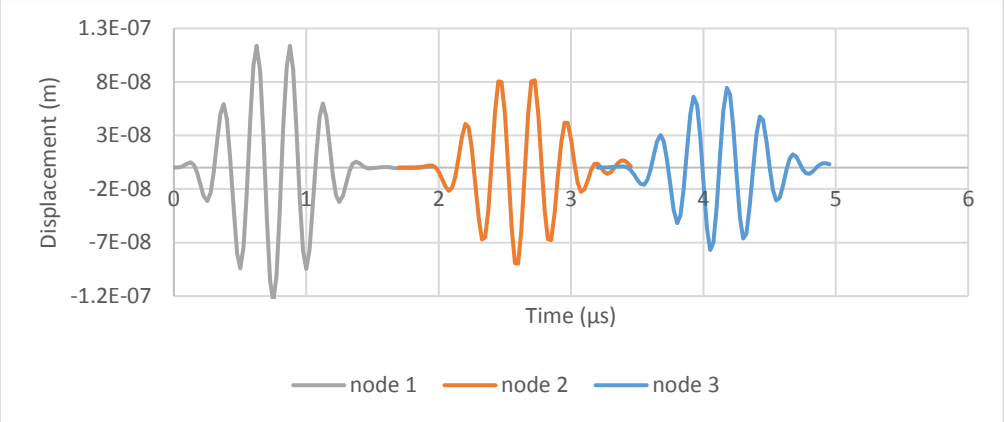

Figure 3-30 The displacement history of node 1, 2 and 3 in the probe recorded in the x-direction of CSYS-2 local coordinate

The speed of sound in the probe is calculated based on the time delay between nodes 1 and 2 in Table 3-3. Both maximum and minimum displacements have been chosen as references point and the related time have been read and used to calculate the speed of sound. The average speed of sound between maxima and minima is 2703 m/s.

Table 3-3 Calculation of the speed of sound in the probe between node 1 and 2

		Time (s)	Δt (s)	Δx (m)	c_l (m/s)
At maximum displacement	node 1	8.76E-07	1.85E-06	0.005	2703.2
	node 2	2.73E-06			
At minimum displacement	node 1	7.51E-07	1.85E-06	0.005	2703.2
	node 2	2.60E-06			
Average					2703.2

Similarly, the time delay between node 2 and 3 are based on the speed of sound calculation. Table 3-4 shows the detail of the calculation. 2757 m/s is calculated as the average speed between maxima and minima.

Table 3-4 Calculation of the speed of sound in the probe between node 2 and 3

		Time (s)	Δt (s)	Δx (m)	c_l (m/s)
At maximum displacement	node 2	2.73E-06	1.45E-06	0.004	2757.1
	node 3	4.18E-06			
At minimum displacement	node 2	2.60E-06	1.45E-06	0.004	2757.1
	node 3	4.05E-06			
Average					2757.1

The average of the speed of sound calculated above, 2703.2 and 2757.1, is equal to 2730.1 which is exactly equal to the theoretical value calculated in Table 3-1. It should be noted that in finite element analysis, the dynamic equation of motion which is introduced in equation 2-80 is solved and the speed of sound is calculated implicitly from its results. While the speed of sound is calculated analytically from the wave equation introduced in equation 2-15

The speed of S-wave is also calculated in the specimen. The local displacement of nodes 4, 5, and 6 in the CSYS-3 coordinate is shown in Figure 3-31.

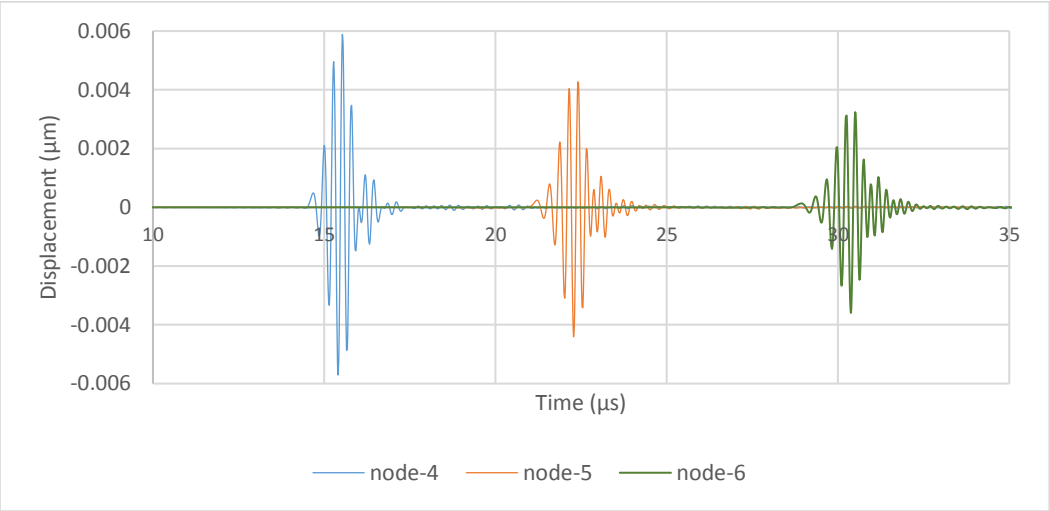

Figure 3-31 The displacement history of node 4, 5 and 6 in the specimen recorded in the x-direction of CSYS-3 local coordinate

Table 3-5 and Table 3-6 represent the calculations for the speed of sound in the specimen. The average of calculated velocities based on two maxima and minima are 3189.7 m/s and 3190.3 m/s. The average of those velocities is equal to 3190 m/s which is slightly lower than the theoretical value of 3250 m/s.

Table 3-5 Calculation of the speed of sound in the specimen between nodes 4 and 5

		Time (s)	Δt (s)	Δx (m)	c_s (m/s)
At maximum displacement	node 4	1.5528E-05	6.63E-06	0.021132	3189.7
	node 5	2.2153E-05			
At minimum displacement	node 4	1.54E-05	6.63E-06	0.021132	3189.7
	node 5	2.2025E-05			
Average					3189.7

Table 3-6 Calculation of the speed of sound in the specimen between nodes 5 and 6

		Time (s)	Δt (s)	Δx (m)	c_s (m/s)
At maximum displacement	node 5	2.2403E-05	7.85E-06	0.025	3184.9
	node 6	3.0252E-05			
At minimum displacement	node 5	2.2278E-05	7.82E-06	0.025	3195.7
	node 6	3.0101E-05			
Average					3190.3

3.8.6 A-scan display

The A-scan displays of the models are created based on the displacement recorded in node 1 of the probe. The process was done by a Matlab code which is attached in appendix 1. As mentioned in section 3.8.4, the first 20 µs of the displacement history comes from noises generated by different waves propagating in the probe. They removed by the procedure described in section 3.8.4. Since the time increment of the models does not match, the time increment between two recordings should be

synchronized. It is done by using spline interpolation in Matlab. The time increment is automatically calculated by Abaqus based on the principles described in section 2.3.2. So, it changes in different models producing a mismatch in their recorded data.

To transfer the displacement history of the models to the A-scan display. The time when the wave propagates inside the probe and coupling media should be calculated and their related displacement values should be removed. By this, the horizontal scale of the A-scan display will be calibrated to zero. So, the location of the back wall echo which is the length that the wave propagates and reaches the back wall can be calculated.

The time when the wave is propagating inside the probe can be calculated by having the distance of propagating and calculated the speed of sound in the probe. The length of the probe center line is p=14.1 mm as shown in Figure 3-2. The speed of sound is also calculated in the previous section which is 2730 m/s. Moreover, we know that the wave is passing through the probe twice until it comes back to the initial location. Thus, two times of the propagation time inside the probe should be removed from the recorded history.

Besides, the wave also passes through the coupling medium, and the propagation time should also be considered. The coupling oblique thickness is equal to 0.6 mm, so the time can be calculated by considering 1500 m/s.

In the specimen, the transmitted wave follows a curve path to reach the centerline as shown in Figure 3-32. If we consider this curve path as a straight line, its length will be 8.1mm as opposed to 5.5mm length from the probe index. This pattern is seen once at the first entrance of the transmitted wave. Thus. the time of propagating wave during the extra length in which the wave propagates more than expected, 2.6mm, should be subtracted.

As a conclusion, the recorded history is calibrated to zero on the horizontal scale. Finally, the time-base history is converted to the distance-based history based on the calculated speed of sound in the specimen to create the A-scan display. A full rectification is also applied to the data.

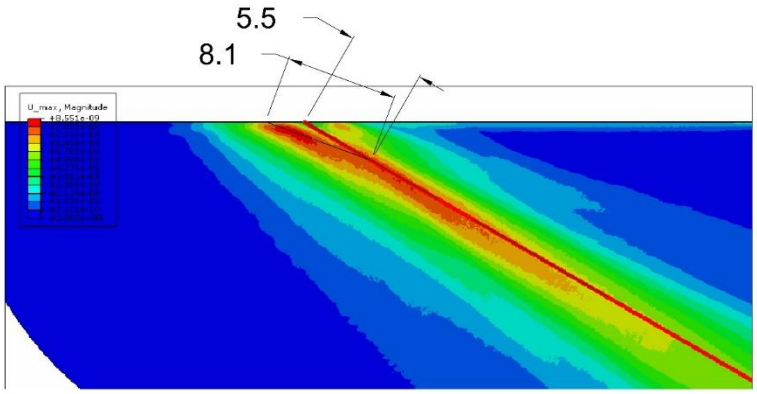

Figure 3-32 A curve path of the transmitted wave at the vicinity of the porbe index. (units in mm)

- The A-scan display of model 1

This procedure is implemented on the displacement history of model 1 to create the A-scan display which is shown in Figure 3-33. The first and second peaks indicate the echos of the 100mm and the 25mm radii, respectively. The echo of the 25mm radius is located at 225mm, which is the length in which the wave propagates to reach that. As described in section 2.2.6.2, the back wall echos in the testing of the V1 calibration block should be in 100mm and 225mm. This verifies the time base

calibration of the A-scan display which is done by simulation. The error of the A-scan display will be presented in the next section.

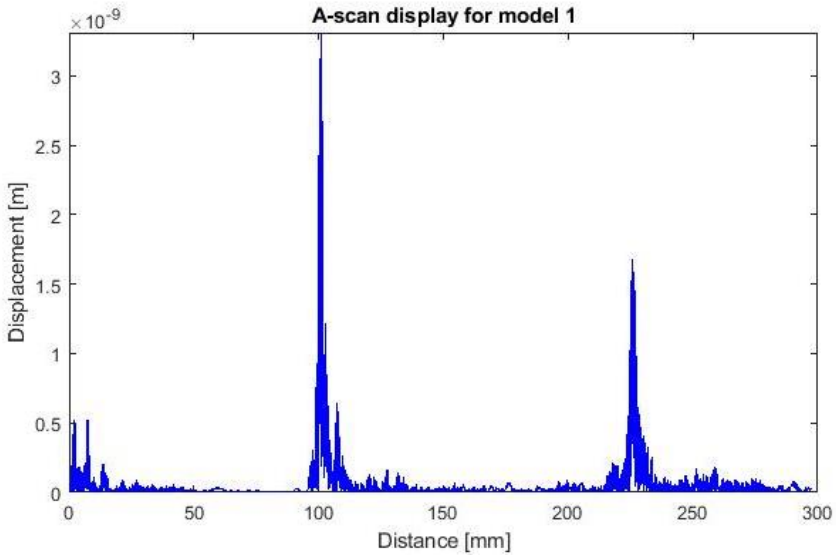

Figure 3-33 The A-scan display of the model 1

A small displacement rise is visible in Figure 3-33 at around 110mm distance. This is an echo of an S-wave generated from transmission of the wave to the probe as shown in Figure 3-14.

- The A-scan display of mode 2 and 3

By the algorithm used to create an A-scan display for model 1, the A-scan display of models 2 and 3 is generated. The parameters calculated in model 1 such as speeds of sound in the probe and specimen and the time delay used to calibrate the time base are applied to create these displays. The A-scan displays of the model 2 and 3 are shown in in Figure 3-34 and Figure 3-35, respectively.

In the A-scan display of model 2, the locations of the first and second echo are around 75mm and 175mm, respectively, and The locations of the first and second echo for model 3 are around 50mm and 125mm.

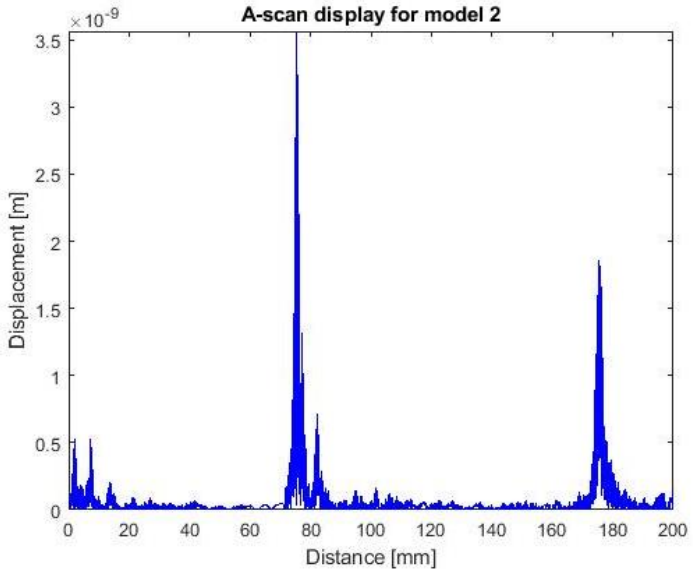

Figure 3-34 The A-scan display of the model 2

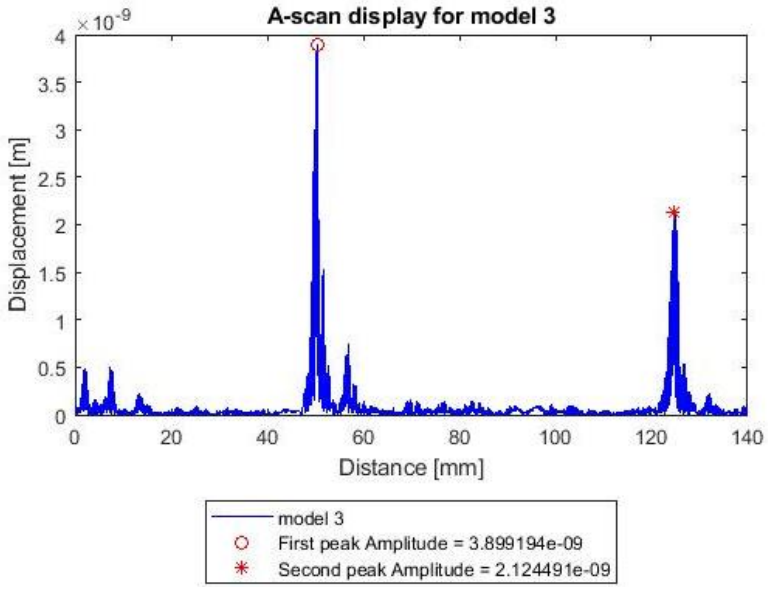

Figure 3-35 The A-scan display of the model 3

3.8.7 Time-base linearity

The location of the first and second back wall echo in the A-scan displays of models 1, 2, and 3 verifies the horizontal scale of the A-scan display is linearly varying with the distance of the back wall. It means that the parameters used to create the A-scan display of model 1 is valid for the other modes.

3.8.8 The error of the A-scan display

To investigate the error of the A-scan creation procedure described in section 3.8.6, the differences between the location of each peak in the display, and the exact value is calculated and presented in Figure 3-36. e1, e2, and e3 are the error of the location of the first peak, second peak, and the distance between them, respectively. The overall error of the three models are less than 1mm in 225mm range and decreases by decreasing the radius from 100mm to 50mm. The errors of the first and second peaks in model 1 are the highest while the error of the distance between them is the lowest. The error values for model 2 are quite reasonable and follow the trend for model 1. However, the location of the second peak in mode 3, e2, is quite high.

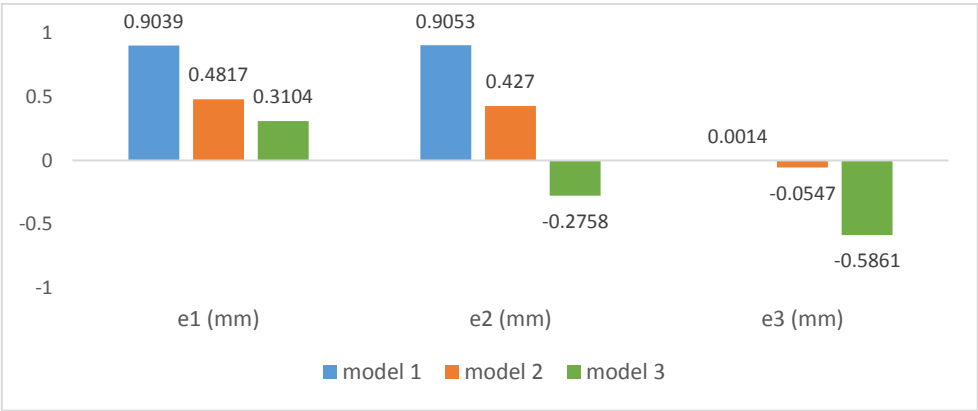

Figure 3-36 The error of the A-scan in three models

The small errors observed in three different models show that the procedure of modeling and data analysis ensures reliable results. Moreover, it reveals that the speeds of the sound calculated in the probe and specimen are almost constant and reliable.

Chapter 4 Experimental measurement

To verify the results of the simulations, an experimental program has been conducted. A V2 calibration block has been used to record the amplitude drop between the first and second back wall echos and then compare the results with the simulation. The V2 block is modeled at model 3 shown in Figure 3-5. The two arcs with the 50mm and 25mm radii of the V2 calibration block are simulated in model 3 as described in section 3.1.

4.1 Test set up

Ultrasonic testing is a relatively convenient inspection method that needs a few pieces of equipment to run. The equipment needed for our testing program is shown in Figure 4-1. The flaw detector used here is EPOCH 600 model made by Olympus [33]. A Krautkramer MWB60-N4 type probe used for the experiments. This is the same probe simulated in the models as described in chapter 3.

Figure 4-1 The test equipment.

The standard V2 calibration block has a faceted shape and needs to be supported upon the test. It was supported by some pieces of steel that they do not interfere the accuracy of the test. Their contractions are established in the locations that the propagating wave inside the V2 calibration block does not possibly transfer to the steel supports. This arrangement is shown in Figure 4-2. A steel block is also placed behind the test piece as a guide for the probe to make sure that the probe beam was exactly parallel to the V2 block. By this, the strongest back wall echo will be detected in the probe. Two pieces of plastic plates are also stacked on the top of the test piece to provide 0.5mm coupling thickness by supporting the two sides of the probe.

Figure 4-2 Test preparation of the V2 calibration block in two different view

The probe is placed on the top of the test piece after adding the coupling liquid. Although the water was modeled as the coupling media, the type of coupling is irrelevant for smooth surfaces.

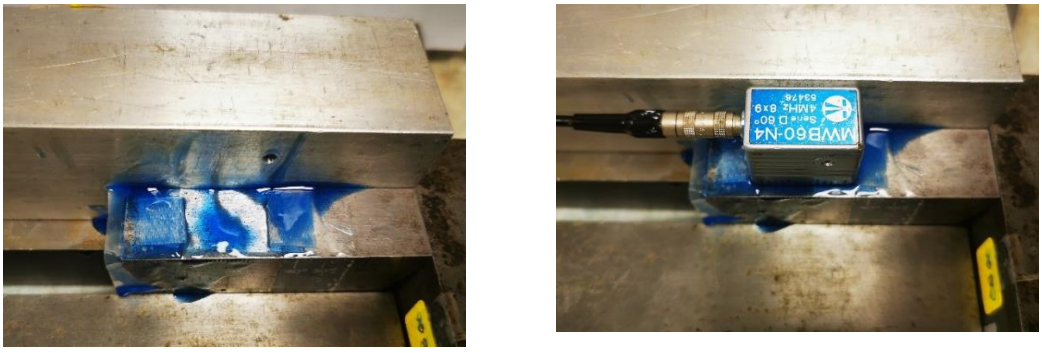

(a)

(b)

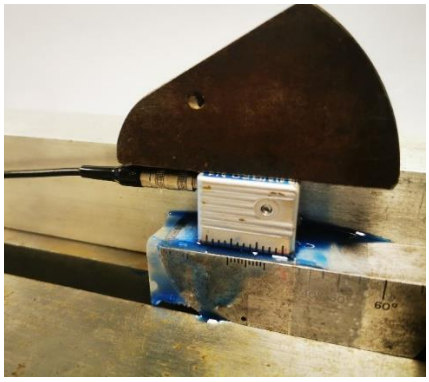

(c)

Figure 4-3 Assembly of the test equipment
a) addition of the coupling liquid, b) the probe location on the block, and c) holding the probe on the test piece by a piece of metal.

The time base of the flaw detector is calibrated by the V2 calibration block. The probe needs to be moved forward and backward until the maximum reflection signal is achieved. The highest amplitude value is frozen and used for calibration of the time base as described in section 2.2.6.2. The probe index and angle are also checked. The time base calibration snapshot is shown in Figure 4-4. The blue shadow shows the dynamic history of the echo height when the probe is moving forward and backward. This is an equipment feature to support the operator to identify the maximum response. The yellow line inside it is the live echo representation which is adjusted to the top of the blue shadow to locate the exact position of the maximum amplitude.

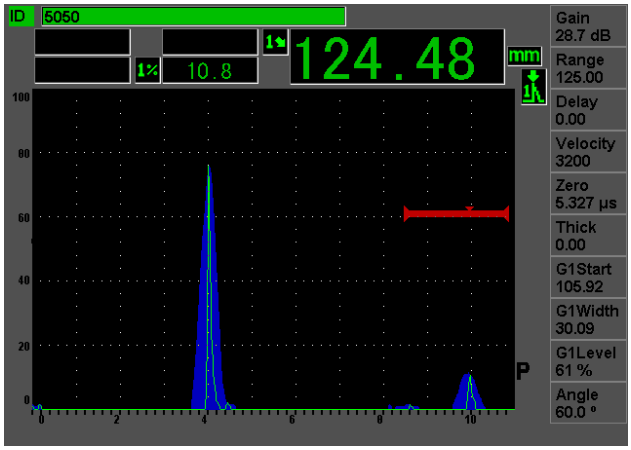

Figure 4-4 Time base calibration of the flaw detector

4.2 Results

The main objective of this test is to measure the amplitude drop between the two echoes of 50 mm and 125mm. The first echo height is adjusted to 80% of the screen height and the applied gain to achieve this level is recorded. As shown in Figure 4-5, the gain is 30.0 dB.

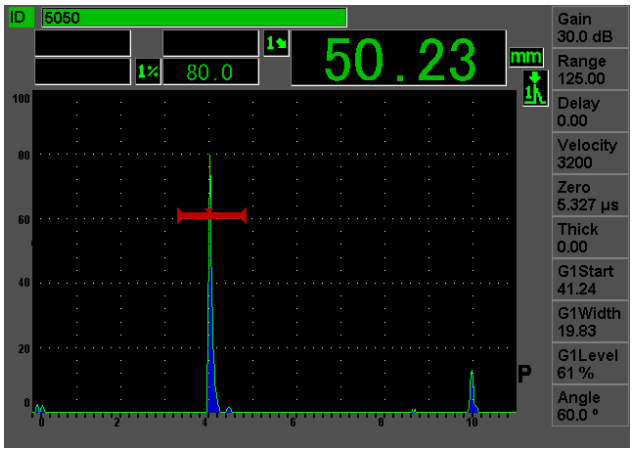

Figure 4-5 The A-scan display to record the gain of the first echo

The same procedure is implemented for the second echo in the 125 mm. Figure 4-6 shows that the gain needed to increase the echo height of this second and smaller echo to 80% of the screen height is 45.5 dB.

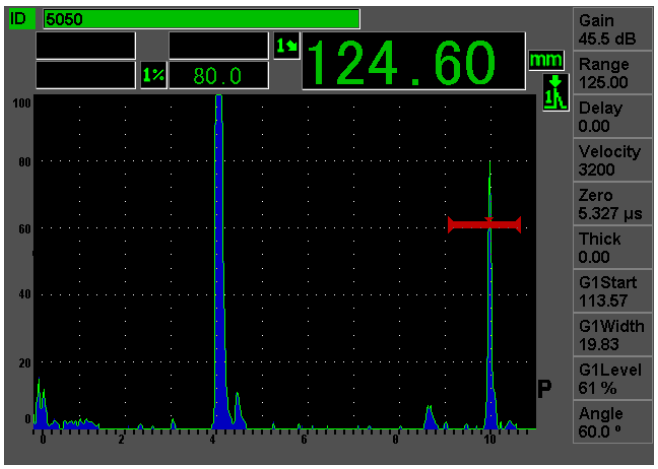

Figure 4-6 The A-scan display to record the gain of the second echo

The gains measured in Figure 4-5 and Figure 4-6 provide an amplitude drop between the two echoes is of 15.5 dB. This amplitude drop includes the transfer loss and material attenuation. By considering 0.04 dB/mm material attenuation in 150mm beam path length between two echoes [24], the amplitude drop should be increased by 6 dB to reach the 9.5 dB drop between two echoes with material attenuation excluded.

The A-scan display shown in Figure 4-6 has more notable information. There are some minor indications in the display which is worthwhile to pay attention to. The A-scan diagram starts with two peaks near to each other and continues with a constant amplitude up to 18mm. Moreover, Just after the main echoes at 50mm and 125mm, a small peak is visible. Finally, there is a small indication at 108mm. These signals will be discussed later in chapter 6.

Chapter 5 Discussion

The results of modeling and experimental measurements are compared and discussed in this chapter. The uncertainties which may affect the results are discussed and explained.

5.1 Models performance

The results presented in section 3.4 are discussed and explained in this section. The results of modeling are also compared with the experimental measurement.

5.1.1 The performance of the FE modeling

5.1.1.1 The wave generation in the probe

A pressure field was applied at the probe loading area to generate the ultrasonic wave inside the probe medium. The pressure field shown in Figure 3-7 has been applied uniformly on the probe edge at the loading area shown in Figure 3-8. Moreover, Figure 3-23 shows that the displacement variation just after the loading area is not uniform. The variation in stiffness along the loading area may responsible for that behavior. The stiffness variation may come from two main sources, the uniform element size and the effect of adjacent non loaded elements. The meshing is done in Abaqus automatically. It changes the size of the element to completely cover throughout the medium. The size introduced to Abaqus is a size with a limited variation. This results in an ununiform meshing in the nonsymmetric polygonal medium. The symmetric shape of the displacement field in Figure 3-23 shows that the effect of adjacent non-loaded elements has more weight on that phenomenon.

The loading method is adapted from the example 2.2.1 Abaqus benchmark problem for the use of infinite elements available in the ABAQUS user manual [30]. Similar to that example, we can see the creation of S-waves at both edges of the loading area shown in Figure 3-12. The reason can be because of the transverse movement of those points producing S-waves.

5.1.1.2 The performance of the reduced integration method

In finite element modeling, the reduced integration method provides a time-efficient analysis, especially in the dynamic analysis. However, some spurious results may arise due to false displacement modes [33]. A Large nodal displacement is one of these modes in which a displaced node passes over the other nodes in the element. The maximum displacement in the loading area can be read from one of the displacement histories of node 1 in different models, for instance, Figure 3-26. This value is 1.14E-7 meters which is much less than the element size at the probe, 5E-5 meters. Thus, we do not expect to have any spurious results in the nodes.

5.1.1.3 The performance of the infinite elements

In our models, infinite elements disperse energy from the probe area, simulating the damping blocks in the actual probe. As described in 2.3.3, these elements can provide “quiet” boundaries. In addition,

their performance is at the highest when nodal displacement occurs along the one-way side of the infinite element. Thus, transverse movements can be reflected. This is one of the reasons that it can be seen some movements after the main wave departures the loading area. In fact, some reflections from the infinite elements are recorded at the model's displacement histories. Drozdz [31] criticizes its performances with these reflections leading to propose absorbing layers that produce high-quality non-reflective boundaries. The procedure of modeling of the infinite element is adapted from the Abaqus benchmark [30].

5.1.2 The probe characteristics and functionalities

5.1.2.1 The probe index

The index of the modeled probe is the point that is expected to be on the probe centerline at the interface with the coupling. This can be interpreted by following the wave path shown in Figure 3-20. The wave enters into the specimen near the probe index. The reflected wave from the back wall concentrates on the probe index point in Consecutive passes. The wave concentration point is unchanged even though the angle of the beam increases by several passes through the medium.

5.1.2.2 The beam angle and speed of sound

The beam angle of the modeled probe is observed around 58 degrees as opposed to 60 degrees expectation. The speed of sound in the specimen can be responsible for this deviation. As calculated in Table 3-5 and Table 3-6, it is 60 m/s less than the theoretical value. This difference can explain 2 degrees deviation by using Snell's law in equation 2-64. By decreasing the speed of sound in the specimen in the denominator, the beam angle should decrease in the numerator to keep the fraction constant. Thus, by using 3190 m/s as the speed of sound, the angle will be 58.2 degrees which is the degree that we observed in the results.

The differences in speed between the theory and FEM can have three reasons, The material properties, the location of nodes for speed of sound calculation making an error in the determination of Δx, and the points on the displacement curves creating an error in the determination of Δt. The material properties introduced to the software have been rounded to integer while the exact numbers providing the theoretical speed of sound are decimal numbers. These decimals are responsible for a portion of this error. In addition, we recorded the displacement history of the nodes on the nominal beam centerline while the true centerline has 2 degrees deviation. This makes an error in calculations of Δx. The third source of error comes from the points on which the time distance is extracted. Although we tried to read the time distance in both maxima and minima, there is still doubt whether they are at the same phase or not. This can cause an error in the determination of Δt in the calculation of the speed of sound in the specimen.

5.1.2.3 The probe near field

In Figure 3-22, we explained that the maximum displacement magnitude occurs at 7.6 mm from the probe index. Also, we have seen the amplitude fluctuation up to 29mm from the probe index. The near field length is defined as the distance from the probe face where the maximum pressure occurs as described in section 2.2. This definition is mainly applied for normal probes [23]. However, Krautkramer [23] represents sonograms for angle probe, Figure 5-1, and mentions that the ultrasonic beam focuses at the end of the near field. By looking at the variation of the beam width for an 8x9 crystal probe with 4 MHz central frequency in Figure 5-1, an almost constant width is observed up to the focusing point. Back to the radiation field in our results in Figure 3-24, a similar pattern can be observed even though the probe angles are not equal. Since the near field is a function of central frequency and size the probe crystal, we can make this comparison. In Figure 5-2 which is a repetition

of Figure 3-24, the points with equal displacement have been drawn by lines in the radiation field showing the concentration of the beam at the end of the near field zone.

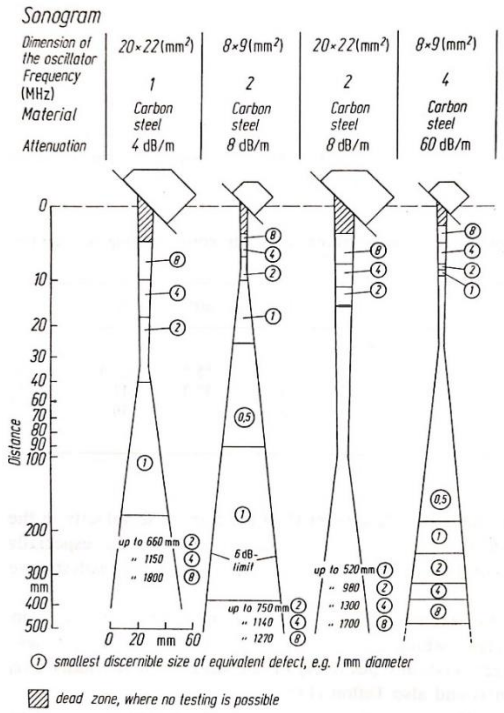

Figure 5-1 Sonograms for 45 degrees angle probe [23]

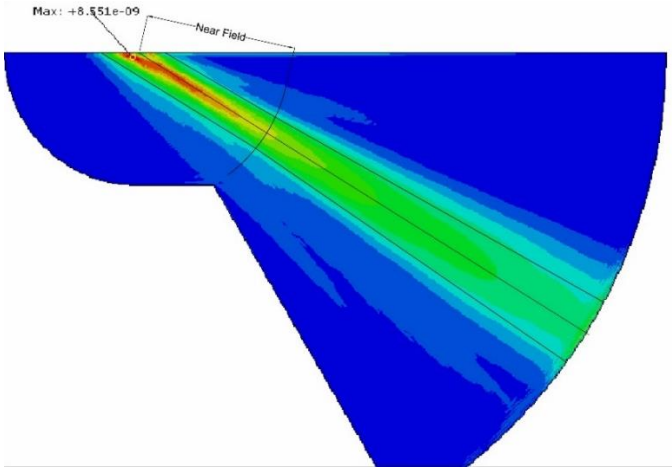

Figure 5-2 Illustration of the focus of the beam in the radiation field representation of the model 1

By considering the distance to the focusing point as the near field length 29mm would be calculated the near field length. This can also be verified by the actual near field length provided by the probe manufacture which is 30mm with a variation of 6mm [26].

5.1.3 The coupling behavior

As mentioned in section 3.6, the acoustic pressure near the steel face is measured to be larger than that of the probe face. The reason can originate from the higher acoustic impedance of the steel compared with perspex. Equation 2-31 demonstrate it mathematically. When a wave hits a medium

with stiffer properties, compression of the wave near the surface of the material will occur due to less deformable properties of it.

As seen in Figure 3-18, The distributions of the acoustic pressure amplitude have two maxima at both sides of the probe index and one local minimum at the probe index in both perspex-water and water-steel interfaces in the top and bottom layer of the coupling medium, respectively. the transmission of the incoming wave from the coupling medium starts far from the probe index at the left side of the coupling medium disturbing the silence situation of it with low acoustic pressure. By progressing the transmission, the amplitude of the wave in the probe rises as seen in the probe radiation field in Figure 3-23. Furthermore, some portion of the disturbance is trapped inside the coupling medium and is reflecting successively towards the probe index point. This intensifies the transmitted waves leading to increase acoustic pressure to the maximum value as seen in Figure 3-18. As the amplitude of the incoming waves decreases up to the probe centerline in Figure 2-12, the acoustic pressure decreases to reach a local minimum in Figure 3-18. Similar to the first maximum, by increasing the amplitude in the probe at the upper area of the probe centerline, the acoustic pressure rises again and reaches the second maximum.

However, the increase in amplitude in the probe is not strong enough to rise the second maximum of the acoustic pressure to the value of the first one. This is because the wave at the upper side of the probe centerline propagates longer than the first one. Thus, the amplitude of it when reaches to the interface is less than the first one.

According to the test results performed by Ginzel [27] explained in section 2.2.3, the voltage amplitude of the probe is minimum when the thickness of the coupling is approaching the half wavelength. Based on that, we expected to have a minimum amplitude due to the thickness of the coupling in our models. The thickness of the coupling in our model is 1.5 times of the wavelength in the water. Since 1.5 times of the wavelength has the same phase of half wavelength, we can use Ginzel's results [27] to conclude that.

5.1.4 The detected echo behavior and verification

5.1.4.1 The A-scan display error

We calculated the error of the process of creating the A-scan display of the models in Figure 3-36. These errors may originate from slight differences in the speed of sound in the models. The speed of sound is calculated implicitly from the results of the models. Since these are finite elements models solved numerically by the method introduces in section 2.3.2, the parameters affecting the accuracy of the analysis is the reason for slight differences between the speed of sound in the models. This was discussed in section 5.1.2.2.

The other reason of error in the location of the peaks in the A-scan display can come from the time delay calculated for zero point in the A-scan display in model 1. In the procedure of creating the A-scan display, the time delay to calibrate timebase to zero is calculated to 5.95 µs in model 1 which is 0.623 µs more than the value used to calibrate in the test device. The time delay of the experimental data can be found in one of the figures of the test results, For example in Figure 4-4. The time delay is shown in the table located on the right side of the display indicated by "Zero" label. In this figure, the zero time used to calibrate the time base in the tests is 5.327 µs.

5.1.4.2 Experimental verification

The time base of the A-scan display of the modes has already been verified. Now, we will study the echo height of them. Model 3 was verified experimentally. The amplitude drop between the two indications in the display was compared with the measured value in the test.

It was mentioned in chapter 2 that the flaw detectors use amplifier circuits to change ”gain” in the system. The gain is a relative quantity of amplification that increases or decreases the height of the indication signals on the UT equipment screen. Thus, the gain can be used to measure the differences between signal response strength two indications. As described in chapter 5, the test results show 9.5 dB amplitude differences between two peaks excluding the attenuation losses while in Figure 3-35, it can be seen a 6.0724 dB difference. Thus, the experimental result is 3.5 dB larger than the results of model 3.

The differences between experimental test and model results can originate from the test errors and modeling errors, which will be explained later in section 5.2.

The A-scan display of model 3 also contains some features in common with the test result. These results are repeated in Figure 5-3. To begin with, there are some minor indications within 17mm of the display of model 3, which is similar to the test result. Moreover, it can be seen an indication just after the main peak at both results which is the sign of the S-wave reached to the crystal. These similarities between the indications of the simulation and the experimental test show the success of the simulation to present the status of the ultrasonic wave during the ultrasonic testing. However, there is an indication in 107mm, 8.6 of horizontal scale, in the test result which can not be seen in the model result. It can be an indication of the reflected wave from the side walls. Since the models are in 2D, it is not expected to see the indications of the 3D experimental test.

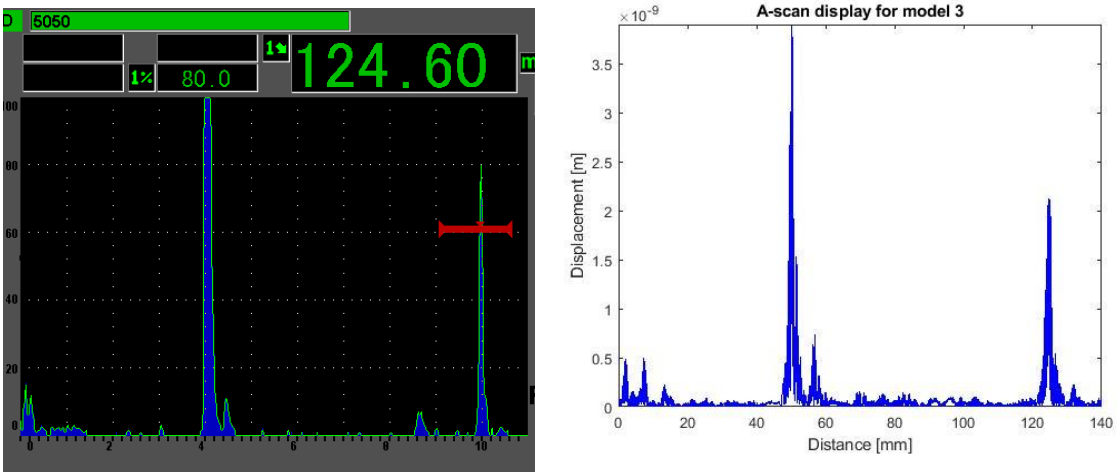

Figure 5-3 Test results, left, and modeling results, right.

5.2 Results uncertainties

Since the results of the simulation and experimental test are compared, parameters that can affect both results should be investigated. The most vital parameters of finite element modeling of the wave propagation in our models have been considered. These include the simulation of the meshing methods and element size and type, and the explicit solving method. However, other parameters can influence the accuracy of the simulation and experimental testing. They are listed as follows:

- Piezoelectric

The piezoelectric crystal is responsible for generating the ultrasonic wave and detecting the reflected echoes. The differences between the actual behavior of piezoelectric crystal and simulated pressure field can produce an error between the modeling result and the experimental measurement.

- Attenuation

The material introduced to our models does not contain any attenuation property. This can significantly affect the echo amplitude compared to an experimental situation. Although the approximate value of the attenuation in the specimen was considered by the rate of 0.04 dB/mm from reference [24] to exclude the amplitude drop due to the attenuation in the specimen from the results of the experimental test, the attenuation in the probe and coupling is not excluded from those results. This is the main source of 3.5 dB differences between the results of the simulation and the experimental test.

- Test equipment accuracy

The accuracy of the test equipment can be influenced by some parameters including the ultrasonic flaw detector accuracy, the cable connection malfunction, and the probe performance. These effects may come from the electronic circuits of the ultrasonic flaw detector, the resistance of the cable, the connections, and the crystal performance. Furthermore, the signal detected from the reflector is filtered by the ultrasonic flaw detector to remove the noises. This filtering may change the real peak value of the echo and be a source of error for the test results. Although the Epoch600 is the ultrasonic flaw detector that is widely used in the industry, and Its performance is reliable among the experts, it is a measurement device with a certain amount of accuracy. The results of this device are compared to the simulation results which is calculated numerically from the theory.

- Test setup error

The arrangement of the test set up maybe a source of error. The test piece is supported by some other blocks as described in chapter 5. The connection between those blocks and the test piece may interrupt the results of the experimental measurement although we tried to minimize this effect by minimizing the connection between them.

Chapter 6 Conclusions and future works

6.1 Conclusions

The purpose of this thesis is to simulate the ultrasonic technique by using the finite element method. This involved studying the simulated probe characteristics, A-scan displays, and experimental testing. The general structure of this thesis is shown in Figure 6-1. According to this figure, the following conclusions can be addressed:

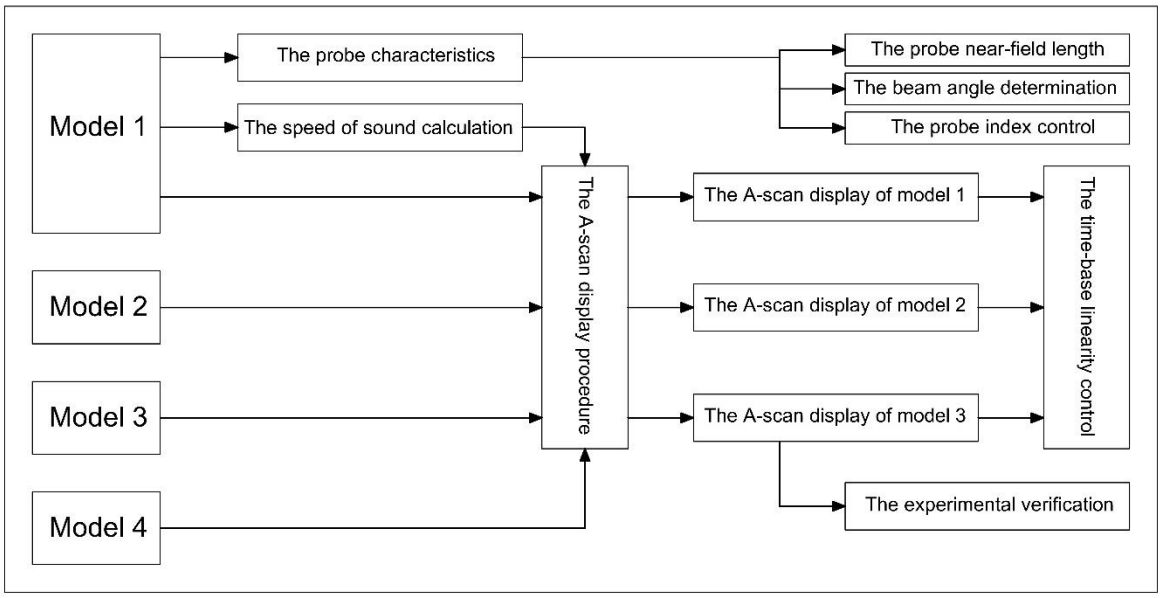

Figure 6-1 The general structure of this thesis

1. The main purpose, which is the application of the finite element method to simulate the ultrasonic testing in the isotropic and homogenous material has been fulfilled. The three main media involving in this test have been modeled and their interactions have been investigated.
2. The ultrasonic calibration process for an angle probe has been simulated. The time base calibration, probe index control, and beam angle determination have been performed. Besides, the probe near-field has been studied in both displacement amplitude diagram and beam radiation field. The simulation results have been verified by the analytical and manufacturing specifications.
3. The A-scan displays of the models have been created based on the parameters obtained from the results of model 1. The speed of sound is the most important parameter to create an A-scan display that is calculated from the results of model 1 and verified by the analytical formula derived in chapter 2. Besides the results of model 4 has been successfully reduced

the noise signals of the other models. The A-scan displays of the three main models have proven the time base linearity showing that the speed of sound and other parameters calculated in model 1 and used to create the A-scan display of the other models is constant by changing the specimens. Therefore, the procedure of modeling is reliable and applicable to simulate specimens with other geometries.

4. The A-scan display of model 3 simulating the V2 calibration block was also compared to the one obtained from the experimental test. The echo signals in both simulation and actual experimental test almost match together. However, the comparison of the amplitude drop between the first and second echo shows that the value of the experimental test is significantly less than the one for simulation. The most likely cause of this mismatch might be attributed to the attenuation of the materials.

6.2 Recommendations for future work

This study provides some opportunities for future works. First of all, the attenuation of the material has a huge impact on the results of the simulation especially in the amplitude of the echo signals. therefore, adding material attenuation in the simulation can help to improve the results. Secondly, the thickness of the coupling medium used in this thesis has been relatively high. The impact of coupling thickness on the results, especially on the probe properties can also be studied. thirdly, the scope of this thesis was limited to the modeling of calibration blocks providing strong back wall echo. So, the application of the introduced modeling procedure can be studied by different specimens with or without defects.

References

[1] S.R. Douglas and K.R. Chaplin, "EWE: A Computer Model for Ultrasonic Inspection", Atomic Energy of Canada Limited, Report AECL-10507, 1991 November.

[2] K.R. Chaplin and V.N. Sycko, "Computer Modeling of A-scans", Ultrasonics International 87 Conference Proceedings, pp. 389-394, London, England, 1987 July.

[3] W. Lord, R. Ludwig, and Z. You, " Developments in Ultrasonic Modeling with Finite Element Analysis", Journal of Nondestructive Evaluation, Vol. 9, No. 2/3, 1990.

[4] F. Ihlenburg and I. Babuska, "Finite element solution of the Helmholtz equation with high wave number, part 1: the h-version of the FEM", Computer Math. Applic. Vol. 30, No. 9, pp. 9-37, 1995.

[5] Richard J. Talbot J.S, and Przemieniecki, "Finite element analysis of frequency spectra for elastic waveguides", Int. J. Solid Structures 12, Issue 3, 1976, Pages 237.

[6] Ame S. Eriksson, Anders Bostrom, HSkan Wirdelius, "Experimental Validation of UTDefect", the Swedish Nuclear Power Inspectorate (SKI), Report 97:3, 1997.

[7] F. Casadei, J.J. Rimoli, M. Ruzzene, "Multiscale finite element analysis of elastic wave scattering from localized defects", Journal of Finite Elements in Analysis and Design, Vol. 88, 2014.

[8] K. Gao, E. Rougier, R. A. Guyer, Z. Lei, P. A. Johnson, " Simulation of crack induced nonlinear elasticity using the combined finite-discrete element method", Journal of Ultrasonics, Vol. 98, 2019.

[9] M. Cohen, and P. C. Jennings, Ed. T. Belytschko and T. R. J. Hughes "Silent Boundary Methods for Transient Analysis (in Computational Methods for Transient Analysis)", Elsevier, 1983.

[10] F. Lakestani, "Validation of mathematical models of the ultrasonic inspection of steel components", ISC m report No. 16, EUR 14673 EN, ECSC-EEC-EAEC Brussels, Luxembourg 1992.

[11] H. Kim, J. Park, S. Song, L. Schmerr, " Modeling angle beam ultrasonic testing using Multi-Gaussian beams", Journal of Nondestructive Evaluation, Vol. 23, No. 3, September 2004.

[12] H. Kim, S. Song, L. Schmerr, "modeling ultrasonic pulse-echo signals from a flat-bottom hole in immersion testing using a Multi-Gaussian beam", Journal of Nondestructive Evaluation, Vol. 23, No. 1, March 2004.

[13] G. Dib, MS Prowant, SL Crawford, SL Crawford, AA Diaz, RE Jacob, "Validation of Ultrasonic Nondestructive Examination (NDE) Computational Models – Phase 1", Pacific Northwest National Laboratory Richland, PNNL-26336, Washington, March 2017.

[14] Manual for Ultrasonic Testing at Level 2, "TRAINING GUIDELINES IN NON-DESTRUCTIVE TESTING TECHNIQUES", Vienna: IAEA, 2018.

[15] K. F. Graff, "Wave Motion in Elastic Solids", New York: DOVER PUBLICATIONS, INC., 1991.

[16] J. L. Rose, Ultrasonic Waves in Solid Media, Cambridge University Press ed., 1999.

[17] S. R. &. A. Hirschberg, "An Introduction to Acoustics, Eindhoven University of Technology", 2019.

[18] D. T. Blackstock, “Fundamentals of Physical Acoustics, John Wiley & Sons”, 2000.

[19] H. P. &. P. RANKIN, “Introduction to Vibrations and Waves, Wiley & Sons”, 2015.

[20] J. D. Achenbach, “Wave propagation in elastic solids”, American Elsevier Pub. Co., 1973.

[21] J.N. Sharma & R. Kaur, “Study of reflection and transmission of plane waves at thermoelastic-diffusive solid/liquid interface”, Latin Americans Journal of Solids and Structures 11, pp. 2141-2170, 2014.

[22] ASM Handbook, vol 17, “Nondestructive evaluation and quality control”, 1989.

[23] J. Krautkramer and H. Krautkramer , “Ultrasonic testing of material”, 4th edition, 1990.

[24] J. C. Drury, “Ultrasonic flaw detection for technicians”, 3rd edition, 2004.

[25] Ed. Ginzel, A. Golshani Ekhlas, M. Matheson, P. Cyr, B. Brown, “Near Field Length Compensation Options”, The e-Journal of Nondestructive Testing, Vol.19, No.06, June 2014.

[26] GE sensing & inspection technology GmbH, “Certificate of calibration for MWB60-4 EN”, Germany, 2015.

[27] E. A. Ginzel, “Automatic ultrasonic testing for pipeline girth welds”, A Handbook, Olympus NDT, Canada, 2006.

[28] J. Chen, Y. Shi, and S. Shi, “Noise analysis of digital ultrasonic system and elimination of pulse noise”, Int. J. Press. Vessel. Pip., vol. 75, pp. 887–890, 1998.

[29] M. S. M Naqiuddin, M. Salman Leong, L. M. Hee, and M. A. M. Azrieasrie, “Ultrasonic signal processing techniques for Pipeline: A review”, EAAI Conference, 2018.

[30] SIMULA. Abaqus 6.14 Documentation, 2014.

[31] M. B. Drozdz, “Efficient finite modeling of ultrasonic waves in elastic media”, Ph.D. thesis, Mechanical Engineering Department, Imperial College of Science, Technology and Medicine, London UK, 2008.

[32] R. D. Cook, D. S. Malkus, M. E. Plesha, and R. J. Witt, “Concepts and applications of finite element analysis”. John Wiley & Sons, Inc, University of Wisconsin - Madison, 2002.

[33] https://www.olympus.no/

Appendix 1

```
%Written by: Hadi Pezeshki, University of Stavanger
%--------------------------------------------------------------------------
% This is the script for the A-scan display for model 1.

clear all; clc;clf;
path='E:\stavenger 2018\semester 4\references\chapter 4\results\4. Data
analysis\5. A-scan display';
name='model displacement node1';
file=fullfile(path,name);

model_1=xlsread(file,'model 1');
model_4=xlsread(file,'model 4');

T1=model_1(:,1);
D1=model_1(:,2);
T4=model_4(:,1);
D4=model_4(:,2);
%Since time increments of the two models are slightly different, we need to
%interpolate the displacement of model 4 in the exact time increment of
%model 1.
D4_new= interp1(T4,D4,T1,'spline');
% The noises at the first 20 microseconds will be extracted by using eq.
% 2-79.
D1=D1-D4_new;
%--------------------------------------------------------------------------
%Creating the A-scan display
% we use the speed of sound in the probe and specimen calculated in the
% model
%Speed of sound in the probe
Cl=2730;
%Speed of sound in the specimen
Cs=3190;
%Length of the probe centerline(mm)
p=14.1;
%100 mm and 25mm radii
r1=100;
r2=25;
%subtracting the time when the wave is propagating through the probe
T1=T1-2*p/Cl/1000-2*0.6/1500/1000-2.5/Cs/1000;
%Calculating the distance
X1=T1/2*Cs*1000;
%The display should start from zero, so the negative time should be
removed.
%The argument can be found as follow
```

```
s=min(X1);
size1=size(X1);
for i=1:size1(1)
    if (X1(i)-s)>abs(s)
        n=i;
        break
    end
end
Distance_1=X1(n:size1);
% Full recticication
D1_R=abs(D1(n:size1));
% finding the argument of first and second peaks, n1 and n2, respectively.
size2=size(D1_R);
s1=size2(1);
s2=round(s1/2);
m1=max(D1_R);
m2=max(D1_R(s2:1:s1));
for i=1:s1
    if D1_R(i)==m1
        n1=i;
    end
    if D1_R(i)==m2
        n2=i;
    end
end
%Error of model 1

e1=Distance_1(n1)-100
e2=Distance_1(n2)-225
e3=e2-e1

% A-scan plot

figure(1)
plot (Distance_1,D1_R,'b')
xlabel('Distance [mm]')
ylabel('Displacement [m]')
title('A-scan display for model 1')
axis([0 250 0 inf])
```

```
%Written by: Hadi Pezeshki, University of Stavanger
%--------------------------------------------------------------------------
% This is the script for the A-scan display for model 2&3.

clear all; clc;clf;
path='E:\stavenger 2018\semester 4\references\chapter 4\results\4. Data
analysis\5. A-scan display';
name='model displacement node1';
file=fullfile(path,name);

model_2=xlsread(file,'model 2');
model_3=xlsread(file,'model 3');
model_4=xlsread(file,'model 4');

T2=model_2(:,1);
D2=model_2(:,2);

T3=model_3(:,1);
D3=model_3(:,2);

T4=model_4(:,1);
D4=model_4(:,2);
%Since time increments of the two models are slightly different, we need to
%interpolate the displacement of model 4 in the exact time increment of
%model 1.
D4_new_2= interp1(T4,D4,T2,'spline');
D4_new_3= interp1(T4,D4,T3,'spline');
% The noises at the first 20 microseconds will be extracted by using eq.
% 2-79.
D2=D2-D4_new_2;
D3=D3-D4_new_3;
%--------------------------------------------------------------------------
%Creating the A-scan display
% we use the speed of sound in the probe and specimen calculated in the
% model
%Speed of sound in the probe
Cl=2730;
%Speed of sound in the specimen
Cs=3190;
%Length of the probe centerline(mm)
p=14.1;
%100 mm and 25mm radii
r1=100;
r2=25;
%subtracting the time when the wave is propagating through the probe
T2=T2-2*p/Cl/1000-2*0.6/1500/1000-2.6/Cs/1000;
T3=T3-2*p/Cl/1000-2*0.6/1500/1000-2.6/Cs/1000;
%Calculating the distance
X2=T2/2*Cs*1000;
X3=T3/2*Cs*1000;
%The display should start from zero, so the negative time should be
removed.
%The argument can be found as follow
% model 2
s=min(X2);
size1=size(X2);
for i=1:size1(1)
    if (X2(i)-s)>abs(s)
```

```
        n=i;
        break
    end
end
Distance_2=X2(n:size1);
% Full recticication
D2_R=abs(D2(n:size1));
% model 3
s=min(X3);
size1=size(X3);
for i=1:size1(1)
    if (X3(i)-s)>abs(s)
        n=i;
        break
    end
end
Distance_3=X3(n:size1);
% Full recticication
D3_R=abs(D3(n:size1));
% finding the argument of first and second peaks, n1 and n2, respectively.
size2=size(D2_R);
s1=size2(1);
s2=round(s1/2);
m1=max(D2_R);
m2=max(D2_R(s2:1:s1));
for i=1:s1
    if D2_R(i)==m1
        n1=i;
    end
    if D2_R(i)==m2
        n2=i;
    end
end
%Error of model 2
e1_2=Distance_2(n1)-75
e2_2=Distance_2(n2)-175
e3_2=e2_2-e1_2
% model 3
size2=size(D3_R);
s1=size2(1);
s2=round(s1/2);
m1=max(D3_R);
m2=max(D3_R(s2:1:s1));
for i=1:s1
    if D3_R(i)==m1
        n1=i;
    end
    if D3_R(i)==m2
        n2=i;
    end
end
%Error of model 3
e1_3=Distance_3(n1)-50
e2_3=Distance_3(n2)-125
e3_3=e2_3-e1_3
%Plot
figure(1)
plot (Distance_2,D2_R,'b')
xlabel('Distance [mm]')
ylabel('Displacement [m]')
title('A-scan display for model 2')
```

```
axis([0 200 0 inf])
figure(2)
plot (Distance_3,D3_R,'b')
xlabel('Distance [mm]')
ylabel('Displacement [m]')
title('A-scan display for model 3')
axis([0 140 0 inf])
```